

CARL VON OSSIETZKY UNIVERSITY OF OLDENBURG

MASTER'S THESIS

Modeling and Analysis of Turbulent Wind Conditions in Numerical Simulations

Author:

Arne HELMS

Supervisors:

Prof. Laura J. LUKASSEN,
Leo HÖNING

*A thesis submitted in fulfillment of the requirements
for the degree Master of Science in Physics*

Computational Fluid Dynamics for Wind Physics
Institute of Physics

January 2021

CARL VON OSSIETZKY UNIVERSITY OF OLDENBURG

Abstract

Faculty of Mathematics and Science
Institute of Physics

Master of Science

Modeling and Analysis of Turbulent Wind Conditions in Numerical Simulations

by Arne HELMS

Within the scope of this work the turbulence model by Mann (1994, 1998) and its utilization as a synthetic inflow for Large Eddy Simulations (LES) through a volume force approach is investigated with particular focus on the resulting changes in the original characteristics of the velocity field. The emphasis is hereby given to the spectral properties, the evolution of the turbulence intensity and the statistics of velocity increments as a measure for the intermittency of the turbulence. Even though the target turbulence is not fully reached, one-point spectra and coherence of the inflow field are, to a large extent, preserved. In addition intermittency in the form of non-Gaussian velocity increments, although not given in the original velocity field, evidently develop in LES. Furthermore, the application of the stochastic time-mapping process of the Continuous-Time Random Walk (CTRW) wind model by Kleinhans (2008) to Fourier simulated Mann turbulence and its associated effects on the statistical properties, particularly with regards to increment statistics, is analyzed. It is demonstrated that the Gaussian wind model by Mann (1994, 1998) can thus be extended by the property of intermittency in the streamwise direction. In spite of changes in the initial second-order structure on small scales, the given approach may pose an alternative to previous concepts for modelled intermittent wind fields which can, for example, be used for the analysis of wind turbine loads.

Contents

Abstract	i
1 Introduction	1
2 Theoretical Background	3
2.1 Fundamentals of Fluid Dynamics	3
2.1.1 Governing Equations	3
2.2 Turbulence	6
2.2.1 The Reynolds Number	6
2.2.2 Stochastic Description of Turbulence	7
2.2.3 Richardson Cascade and Scales of Turbulent Motion	11
2.2.4 Kolmogorov 1941 Theory	12
2.2.5 Intermittency	13
2.2.6 Rapid Distortion Theory	14
2.2.7 Atmospheric Turbulence	17
2.3 Wind Field Models	19
2.3.1 The Mann Turbulence Model	19
2.3.2 The CTRW Model	25
3 Large Eddy Simulation	28
3.1 Subgrid Scale Model WALE	30
3.2 PIMPLE Algorithm	31
3.3 Turbulent Inflow Method	32
4 Analysis of Fourier Simulated Mann Turbulence	34
4.1 One-Point Spectra and Variances	36
4.2 Coherence	38
4.3 Divergence	40
4.4 Increment Statistics	42
5 Large Eddy Simulation with Mann Turbulence Inflow	44
5.1 Numerical Setup	44
5.2 Verification of the Inflow Method	47
5.3 Influence of the Spatial Resolution	49
5.4 One-Point Spectra	50
5.5 Turbulence Intensities	52
5.6 Coherence	56
5.7 Increment Statistics	60
6 Application of Stochastic Time Mapping to Mann Turbulence	63
6.1 Spectral Properties and Coherence	65
6.2 Divergence	66
6.3 Increment Statistics	67

7 Conclusion and Outlook	69
A Probability Distributions	73
B Notes on the Turbulence Intensity Definition	75
C OpenFOAM® Setup for LES	77
D Parameter for LES Inflow Mann Box	88
Bibliography	89

List of Figures

2.1	Mach number at rotor tip as function of the tip speed.	5
2.2	Dye traces in laminar and turbulent flows (Reynolds, 1883).	7
2.3	Turbulent free jet stream with $\text{Re} \approx 2300$	11
2.4	Visualization of redistribution of ε according to Kolmogorov (1962).	13
2.5	Probability density functions for velocity increments.	15
2.6	Kolmogorov and von Kármán spectrum.	18
2.7	One-point spectra of the isotropic Mann turbulence model	20
2.8	Variances as function of Γ (Mann turbulence model)	23
2.9	Comparison of Mann model with data from the Great Belt coherence experiment.	23
2.10	Definition set of the Fourier simulated turbulence according to Mann (1998).	24
2.11	Comparison between a classical Random Walk and a Continuous-Time Random Walk.	25
2.12	Lévy distribution.	26
2.13	Schematic illustration of the time-mapping process.	27
3.1	Volume force required for the acceleration by u'	33
3.2	Schematic illustration of the inflow method	33
4.1	Absolute value of velocity fluctuations of Fourier simulated turbulence in (x, y) and (x, z) plane.	35
4.2	Absolute value of velocity fluctuations of Fourier simulated turbulence in (y, z) plane.	35
4.3	Turbulent velocity fluctuation components as function of x	35
4.4	Power spectral densities of simulated turbulence with parameters from ESDU fit.	36
4.5	Variances for simulated turbulence as function of L_x/L	38
4.6	Coherence of simulated turbulence with parameters from ESDU fit.	39
4.7	PDF of the divergence within the domain \mathcal{B}	40
4.8	Standard deviation of the divergence as function of iterations.	41
4.9	Power spectral densities of original and divergence-corrected field.	42
4.10	Increment PDFs simulated turbulence with parameters from ESDU fit.	43
5.1	Computational domain of the LES.	45
5.2	LES flow field for Mann box input.	46
5.3	Horizontal axis wind turbine with major components.	47
5.4	Temporal evolution of input and output velocity field for LES.	48
5.5	Magnitude ratio of output and input velocity field for LES.	49
5.6	One-point spectra in LES for different spatial resolutions of the LES domain.	50
5.7	One-point spectra in LES for $\langle \text{TI}_x^{\text{in}} \rangle_{\mathcal{I}} = 5\%$	51
5.8	One-point spectra in LES for $\langle \text{TI}_x^{\text{in}} \rangle_{\mathcal{I}} = 10\%$	51

5.9	One-point spectra in LES for $\langle \text{TI}_x^{\text{in}} \rangle_{\mathcal{I}} = 15\%$	52
5.10	Turbulence intensities in LES for $\langle \text{TI}_x^{\text{in}} \rangle_{\mathcal{I}} = 5\%$	54
5.11	Turbulence intensities in LES for $\langle \text{TI}_x^{\text{in}} \rangle_{\mathcal{I}} = 10\%$	54
5.12	Turbulence intensities in LES for $\langle \text{TI}_x^{\text{in}} \rangle_{\mathcal{I}} = 15\%$	55
5.13	Ratios of spatially averaged turbulence intensities in LES and respective input turbulence intensities	55
5.14	Coherence in LES for $\langle \text{TI}_x^{\text{in}} \rangle_{\mathcal{I}} = 5\%$	57
5.15	Coherence in LES for $\langle \text{TI}_x^{\text{in}} \rangle_{\mathcal{I}} = 10\%$	58
5.16	Coherence in LES for $\langle \text{TI}_x^{\text{in}} \rangle_{\mathcal{I}} = 15\%$	59
5.17	Velocity increment PDF in LES for $\langle \text{TI}_x^{\text{in}} \rangle_{\mathcal{I}} = 5\%$	60
5.18	Velocity increment PDF in LES for $\langle \text{TI}_x^{\text{in}} \rangle_{\mathcal{I}} = 10\%$	61
5.19	Velocity increment PDF in LES for $\langle \text{TI}_x^{\text{in}} \rangle_{\mathcal{I}} = 15\%$	61
5.20	Kurtosis of velocity increments in LES.	62
6.1	Representation of the time-mapping for $c = 8$, $\Delta s_t \langle U \rangle = 40\text{ m}$ and different values for α	64
6.2	Histogram of $\tau_{\alpha,c} = dt/ds$ for different values for α	64
6.3	Power spectral densities for original and time-mapped velocity field. .	65
6.4	Standard deviations for original and time-mapped velocity field. . .	66
6.5	Coherence for original and time-mapped velocity field	66
6.6	PDFs for the divergence of original and time-mapped velocity fields. .	67
6.7	PDFs of velocity increments of original and time-mapped velocity fields.	68
6.8	Kurtosis for original and time-mapped velocity fields.	68
7.1	Parameterization for the energy spectrum.	72

List of Tables

List of Abbreviations

ABL	Atmospheric Boundary Layer
CDF	Cummulative Distribution Function
BEM	Beam Element Momentum
CFD	Computational Fluid Dynamics
CTRW	Continuous-Time Random Walk
DNS	Direct Numerical Simulation
ESDU	Engineering Science Data Unit
FFT	Fast Fourier Transform
FVM	Finite Volume Method
HAWC2	Horizontal Axis Wind turbine simulation Code, 2nd generation
LES	Large Eddy Simulation
PDE	Partial Differential Equation
PDF	Probability Density Function
PIMPLE	Combination of PISO and SIMPLE
RANS	Reynolds-Averaged Navier-Stokes
PISO	Pressure Implicit with Splitting of Operator
RDT	Rapid Distortion Theory
RW	Random Walk
SGS	Subgrid-Scale
SIMPLE	Semi-Implicit Method for Pressure-Linked Equations
TI	Turbulence Intensity
WALE	Wall-Adapting Local Eddy-viscosity

Chapter 1

Introduction

Models and numerical simulations of atmospheric turbulent flow are of great importance for various kinds of studies like on the transport and deposition of pollutants through the air (e. g., Santiago et al., 2017) or the interaction between turbulent flow and mechanical structures (Breuer et al., 2011). In view of the growing significance of renewable energy production, they are further particularly relevant for the aerodynamic development of wind turbines and the investigation and planning of wind farms (Mann and Peinke, 2016). A major challenge in this respect results from the large variety of spatial and temporal scales which influence the properties of turbulent wind conditions and whose consideration in numerical simulations necessitates vast computational effort. The lowest part of the Earth's atmosphere—the atmospheric boundary layer—where the turbulence dominates the vertical exchange of all meteorologically relevant variables (Nieuwstadt and Duynkerke, 1996), reaches up to 3 km above the ground (Stull, 2012). On the other hand, detailed knowledge of the wind fields down to millimetre scale is required for the prediction and characterization of wind turbine operating conditions (Mann and Peinke, 2016). Chapter 2 of this work presents the theoretical background for the physical descriptions of fluid motion through the Navier-Stokes equations and turbulent flow in particular. Moreover, models for turbulent wind, that are dealt with in this work, are introduced.

In the field of Computational Fluid Dynamics (CFD), different tools and methods have been developed to lower the computational costs of turbulent flow simulations. The most common methods are the Large Eddy Simulation (LES) and the RANS simulation which determines the solution of the Reynolds-Averaged Navier-Stokes equations. In LES, the governing equations are solved for a filtered velocity that represents the large-scale turbulent motion while simultaneously the influence of the non-resolved scales is included as subgrid-scale models. In RANS simulations, no turbulent structures are resolved but instead taken into account using turbulence models. LES is utilized in this work and therefore described in Chapter 3.

The computational effort can be further reduced by the utilization of inflow methods, i. e., the introduction of a turbulent velocity field to the simulation domain instead of a complete development of it therein. These methods find application in CFD simulations and Blade Element Momentum (BEM) simulations that are used for the calculation of local forces, for example on wind turbine blades.

A variety of turbulent inflow methods are being utilized in the field of wind energy and other research areas. They can be subdivided into two classes: Either the inflow is extracted from the interior of the simulation domain where the turbulence builds up—these approaches are denoted as *recycling methods*—or a synthetic turbulent inflow, which is based upon some mathematical model, is used. While the former has the advantage that the inflow is always a solution to the Navier-Stokes equations, the synthetic inflow approach generally requires less computational effort and its characteristics are naturally known in advance (Ehrich, 2020).

The generation of synthetic turbulent fields is based on respective mathematical models. They are distinguished by focusing on different statistical properties while neglecting others and are thus accompanied by different advantages and disadvantages. Examples include the *Digital Filter model*, which was originally proposed by Klein et al. (2003) and has since been developed further with regard to increased computational efficiency (Xie and Castro, 2008) and physical properties (e. g., Di Mare et al., 2006), and the *method of Random Spots* by Kornev and Hassel (2007) which is based on the autocorrelation function. Methods that focus on the spectral properties of turbulent flow and are based on the description of turbulence in the Fourier domain are the Sandia method by Veers (1984) and the Mann model (Mann, 1994, 1998). A further model that stands out from the previous models due to its consideration of higher-order statistics of velocity increments, i. e., the differences of velocities that are temporally (or spatially) separated by a given time interval (or length), is the Continuous-Time Random Walk (CTRW) model by Kleinhans (2008). A particular challenge in the regard of turbulent inflow is to ensure an advection of the turbulent structures through the numerical domain with as little as possible damping. In the scope of this work, the introduction of modeled turbulence through a volume force approach in LES, carried out with the open-source C++ toolbox OpenFOAM® (Weller and Jasak, 2019), is investigated. For this matter, the model by Mann (1994, 1998), of which detailed analysis is the subject of Chapter 4, is used. Hereby, particular attention is given to the change of initial statistical properties—namely the one-point spectra, the turbulence intensities, the coherences and the velocity increment distributions—within the LES. The results are dealt with in Chapter 5.

As mentioned above, turbulence models differ in terms of the statistical properties they include or omit. One important characteristic that relates to the above stated velocity increments is denoted as *intermittency* which expresses itself in non-Gaussian distributions of the velocity increments and concomitant excessive probabilities for extreme events for short temporal (or spatial) separations and has been identified as a key feature of turbulent wind (Boettcher et al., 2003). A method for the generation of intermittent fluid particle trajectories for instance was proposed by Lukassen and Wilczek (2017) through an ensemble of Gaussian velocity time series whose individual members are varying with respect to their correlation function. The generation of intermittency in the CTRW model of Kleinhans (2008) however is based on a stochastic time-mapping process which leads to a distortion of the time axis. Chapter 6 concerns the application of this time-mapping process to a modeled turbulent field according to Mann (1994, 1998) which inherently does not capture the property of intermittency. The focus here is on the influence on the spectral properties of the field, its divergence and the change of increment statistics.

In Chapter 7, the main findings are summarized and discussed. Moreover, an outlook on further research is provided.

Remarks on Notation

The Einstein summation convention of index notation applies throughout this work. If indices appear twice in a single term, it implies summation over all the values of the index unless specifically stated otherwise. Furthermore, indices $i, j, k, l \in \{1, 2, 3\}$ refer to Cartesian coordinates, i. e., $x_1 = x$, $x_2 = y$, $x_3 = z$. Vector quantities are indicated in bold.

Chapter 2

Theoretical Background

2.1 Fundamentals of Fluid Dynamics

The physical description of the motion of fluids is vitally important for various areas in science and technology. Fluid dynamics is a subdiscipline of continuum mechanics which represents a generalization of Newtonian mechanics on continua. Continuum mechanics can be used to describe the macroscopic behaviour of matter under the influence of mechanical stress. It models matter as a continuum and thus neglects its microscopic structure. This idealization, denoted as *continuum hypothesis*, generally applies if the mean free path λ of the fluid molecules is much smaller than the characteristic length scale of the flow ℓ . This precondition can be represented using the *Knudsen number* Kn which is defined as the ratio of these length scales (Karniadakis et al., 2006):

$$\text{Kn} \equiv \frac{\lambda}{\ell} \ll 1. \quad (2.1)$$

Whereas at sea level, the molecular mean free path of air is given by approximately $2.1 \cdot 10^{-7} \text{ ft} \approx 64.01 \text{ nm}$, it reaches a value of nearly $24 \text{ ft} \approx 7.3 \text{ m}$ at an altitude of $400,000 \text{ ft} \approx 121.9 \text{ km}$ where atmospheric air cannot be modeled as a fluid continuum anymore (Phillips, 2010). However, in the atmospheric boundary layer (see Section 2.2.7), which reaches up to about 3 km above the ground (Stull, 2012), the continuum hypothesis applies.

As explained in the following, differential equations for the velocity field \mathbf{U} and the thermodynamical pressure p that represent the conservation of momentum and mass can be formulated based on this hypothesis.

This work refrains from going into detail as to the derivation of the equations used here. The corresponding literature (e. g., Faber, 1995) should instead be consulted.

2.1.1 Governing Equations

A *material volume* $\mathcal{V}(t)$ inside a fluid consists of the same fluid particles by definition. Often, the integral of a physical quantity $\phi(\mathbf{x}, t)$ (e. g., $\phi = \rho$ or $\phi = U_i$) over this volume $\mathcal{V}(t)$ is of interest. Furthermore, the temporal derivative of this integral is non-trivial, since in addition to the integrand $\phi(\mathbf{x}, t)$, the region of integration $\mathcal{V}(t)$ is time-dependent. The *Reynolds transport theorem*, a three-dimensional generalization of the Leibniz integration rule, provides an alternative formulation of the derivative as the sum of the rate of change of $\phi(\mathbf{x}, t)$ within the volume $\mathcal{V}(t)$ and the flux of $\phi(\mathbf{x}, t)$ across its surface $\partial\mathcal{V}(t)$:

$$\frac{d}{dt} \int_{\mathcal{V}(t)} \phi(\mathbf{x}, t) d^3x = \int_{\mathcal{V}(t)} \frac{\partial \phi(\mathbf{x}, t)}{\partial t} d^3x + \int_{\partial\mathcal{V}(t)} \phi(\mathbf{x}, t) \mathbf{u}(\mathbf{x}, t) \cdot \mathbf{n} d^2f. \quad (2.2)$$

\mathbf{n} is the outward pointing unit normal vector. With the Reynolds transport theorem, the governing differential equations for mass and momentum can be derived from assumptions about material volumes, as is shown below. To keep the structure of the equations clear, the *material derivative*

$$\frac{D}{Dt} \equiv \frac{\partial}{\partial t} + \mathbf{U} \cdot \nabla \quad (2.3)$$

is introduced. It describes the temporal rate of change of any physical quantity of a fluid particle that is subjected to the macroscopic velocity field \mathbf{U} .

Continuity equation

The mass $\int_{\mathcal{V}(t)} \rho d^3x$ (i. e., the volume integral of the density ρ) of any material volume $\mathcal{V}(t)$ is constant over time, because it always consists of the same fluid particles:

$$\frac{d}{dt} \int_{\mathcal{V}(t)} \rho d^3x = 0. \quad (2.4)$$

With the Reynolds transport theorem (Eq. 2.2) and Gauss's theorem follows

$$\int_{\mathcal{V}(t)} \frac{\partial \rho}{\partial t} d^3x + \int_{\partial \mathcal{V}(t)} \rho \mathbf{U} \cdot \mathbf{n} d^2f = \int_{\mathcal{V}(t)} \left(\frac{\partial \rho}{\partial t} + \nabla \cdot (\rho \mathbf{U}) \right) d^3x = 0. \quad (2.5)$$

Since this must be fulfilled for any arbitrary material volume, the integrand must vanish, from which the continuity equation

$$\frac{\partial \rho}{\partial t} + \nabla \cdot (\rho \mathbf{U}) = 0 \quad (2.6)$$

follows, which is equivalent to

$$\frac{D\rho}{Dt} = -\rho \nabla \cdot \mathbf{U}. \quad (2.7)$$

The left-hand side of the equation represents the temporal change of the density of fluid particles. If the flow is incompressible, i. e., $D\rho/Dt = 0$, the divergence of the velocity field vanishes:

$$\nabla \cdot \mathbf{U} = 0. \quad (2.8)$$

Even though every flow is compressible, it can be approximated as incompressible if the Mach number, i. e., the ratio of $|\mathbf{U}|$ and the speed of sound, is less than 0.3, since density changes due to velocity are in the order of 5 % in this case (Anderson Jr, 2010). Regarding the aerodynamics of wind turbines, the highest velocities occur at the tips of the rotor blades. At optimal inflow conditions, the rotor tips are exposed to effective velocities of

$$U_{\text{eff}} = \sqrt{\omega^2 R^2 + U_{\infty}^2}, \quad (2.9)$$

where ω denotes the rotor speed, R denotes the blade radius and U_{∞} denotes the inflow velocity in large distance to the rotor. The product ωR equals the tip speed of the rotor. As seen in Fig. 2.1, Mach numbers of 0.3 are exceeded at tip speeds of about 100 m/s. Due to the increasing size of modern wind turbines and request for high tip speeds, the incompressible assumption might therefore be violated in some

cases (Sørensen et al., 2018). In the scope of this work, however, incompressibility is assumed for the turbulence model as well as for numerical simulations.

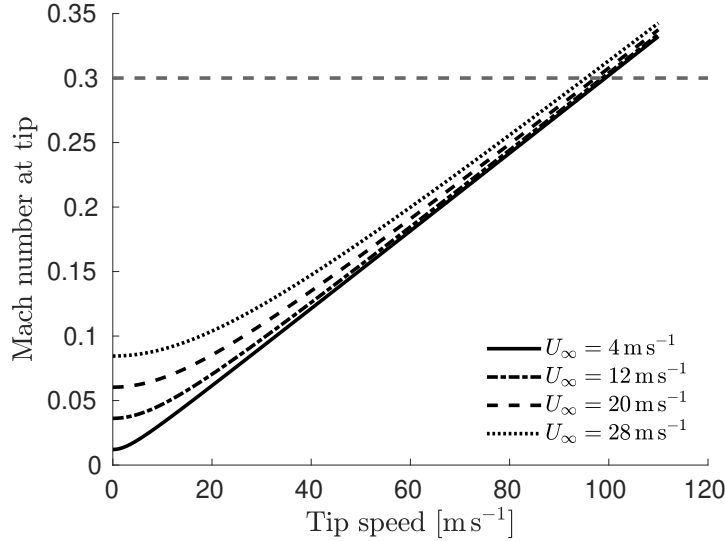


FIGURE 2.1: Mach number at rotor tip as a function of the tip speed for different inflow velocities assuming the speed of sound at approximately 331.3 m s^{-1} , which corresponds to a temperature of 273.15 K (0°C , standard conditions) (Bies et al., 2017).

Navier-Stokes equation

In accordance to Newton's second law of motion, the conservation of momentum of a material volume can be stated as

$$\frac{d}{dt} \int_{\mathcal{V}(t)} \rho \mathbf{U} d^3x = \mathbf{F} \quad (2.10)$$

where \mathbf{F} is the sum of forces acting on $\mathcal{V}(t)$. Distinctions are made between volume forces, which can be expressed as integrals $\int_{\mathcal{V}(t)} \mathbf{f}(\mathbf{x}, t) d^3x$ over volume force densities¹ $\mathbf{f}(\mathbf{x}, t)$, and surface forces resulting from the contact of $\partial\mathcal{V}(t)$ to the surrounding fluid. Typically, surface forces depend not only on the position \mathbf{x} and the time t , but also on the local orientation of the surface, described by the unit normal vector \mathbf{n} . In analogy to volume force density, surface densities $\mathbf{t}(\mathbf{x}, \mathbf{n}, t)$ are assigned to surface forces so that they can be expressed as $\int_{\partial\mathcal{V}(t)} \mathbf{t}(\mathbf{x}, \mathbf{n}, t) d^2f$. Further, Cauchy's theorem states, that surface forces can be represented as the product of the *Cauchy stress tensor* τ_{ij} and the unit normal vector. Hence with Reynold's transport theorem follows

$$\int_{\mathcal{V}(t)} \rho \frac{D\mathbf{U}_i}{Dt} d^3x = \int_{\mathcal{V}(t)} f_i d^3x + \int_{\partial\mathcal{V}(t)} \tau_{ij} n_j d^2f \quad (2.11)$$

For incompressible Newtonian fluids, i. e., fluids in which the shear stresses—the off-diagonal elements of τ_{ij} —are always linear to the rate of deformation over time, the so-called rate of strain

$$S_{ij} \equiv \frac{1}{2} \left(\frac{\partial U_i}{\partial x_j} + \frac{\partial U_j}{\partial x_i} \right), \quad (2.12)$$

¹hereinafter simply designated as volume forces

the Cauchy stress tensor is given as

$$\tau_{ij} = -p \delta_{ij} + 2 \mu S_{ij} \quad (2.13)$$

where δ_{ij} denotes the Kronecker delta function and μ denotes the dynamic viscosity of the fluid. Thus, again applying Gauss's theorem and assuming that the above equations must be satisfied for any arbitrary material volume, the Navier-Stokes equation (NSE) for incompressible flows arises:

$$\rho \frac{D\mathbf{U}}{Dt} = -\nabla p + \mu \nabla^2 \mathbf{U} + \mathbf{f}. \quad (2.14)$$

Further, taking the divergence of the NSE yields following Poisson equation for the pressure:

$$\nabla^2 p = -\nabla \cdot (\mathbf{f} - (\mathbf{U} \cdot \nabla) \mathbf{U}). \quad (2.15)$$

In a wider sense, the term Navier-Stokes equations refers to both continuity and momentum equation.

Bernoulli's equation

Bernoulli's equation is given as

$$\frac{1}{2} \rho \mathbf{U}^2 + p = \text{const} \quad (2.16)$$

and describes the relation between the velocity and the pressure along streamlines, i. e., curves that are instantaneously tangent to \mathbf{U} , for inviscid fluids ($\mu = 0$). The equation can directly be derived from the Navier-Stokes equation (see, for example, Turns, 2006).

2.2 Turbulence

2.2.1 The Reynolds Number

The phenomenon of turbulence denotes the irregular movement of fluids consisting of vortices on many scales, that occurs at high kinetic energies at which damping effects dominate viscous friction. Vortices (or *eddies*) elude precise definition but can be intuitively described as a rotating movement of fluid particles around a straight or curved axis of rotation.

The transition from laminar flow to turbulence can be described via the dimensionless *Reynolds numbers*

$$\text{Re} \equiv \frac{\mathcal{U} \ell}{\nu} \quad (2.17)$$

in which ℓ denotes the characteristic length of the flow that is defined depending on the problem (e. g., the length of an obstacle in the mean flow direction). \mathcal{U} is the characteristic velocity and $\nu = \mu/\rho$ is the kinematic viscosity. The idea of the non-dimensional Reynolds number as a characteristic quantity for turbulent flows has its origin in Osborne Reynolds studies on the dynamical behaviour of water in pipes at different flow rates (Fig. 2.2). In these experiments, Reynolds introduced a small jet of dyed water into the center of flow through a glass pipe. It was evident that

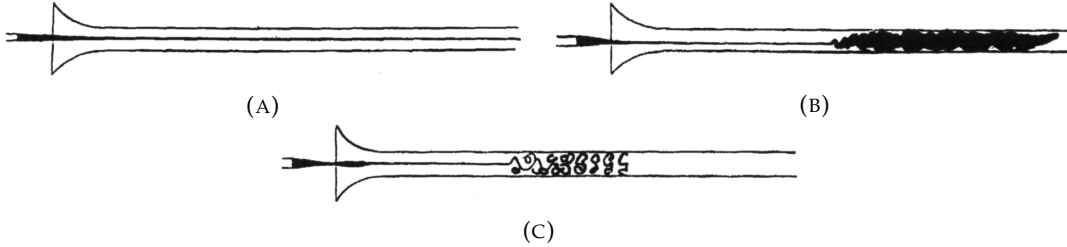


FIGURE 2.2: Dye traces in laminar and turbulent flows. From Reynolds (1883). Laminar flow at low velocity (A), diffuse dye viewed by the naked eye (B), coherent structures seen under electric spark (C).

the dyed layer remained distinct and undisturbed within the tube. For increased velocities, however, diffusion of the dyed layer through the cross-section of the fluid was visible which marked the transition point from laminar to turbulent flow.

The Reynolds number can be interpreted as the ratio of inertial and viscous forces in the flow. An undimensionalization of the Navier-Stokes equation (Eq. 2.14) further illustrates its physical meaning. To transfer the dimensioned variables velocity \mathbf{U} , pressure p , volume force f , Cartesian coordinates x_i and time t into respective non-dimensional quantities (marked with \dagger), they are referred to quantities intrinsic to the system: $\mathbf{U} = \mathbf{U}^\dagger \mathcal{U}$, $p = p^\dagger \rho \mathcal{U}^2$, $f = f \ell / \mathcal{U}^2$, $x = x^\dagger \ell$, $t = t^\dagger \ell \mathcal{U}$. Substitution into the NSE (Eq. 2.14) leads to the following non-dimensional NSE:

$$\frac{\partial \mathbf{U}^\dagger}{\partial t^\dagger} + (\mathbf{U}^\dagger \cdot \nabla^\dagger) \mathbf{U}^\dagger = -\nabla^\dagger p^\dagger + \underbrace{\frac{\nu}{\mathcal{U} \ell}}_{=\text{Re}^{-1}} \nabla^{\dagger 2} \mathbf{U}^\dagger. \quad (2.18)$$

The continuity equation takes the form $\nabla^\dagger \cdot \mathbf{U}^\dagger = 0$. This shows, that the flow properties in units given by the scales of the system are fully described by the Reynolds number. Furthermore, the viscous terms vanish for $\text{Re} \rightarrow \infty$. Thus, flows with high Reynolds number can be approximated as inviscid.

Atmospheric flow is generally turbulent due to large values of \mathcal{U} and ℓ (Jacob, 1999). Turbulent flows are identified as homogeneous if all statistical properties are the invariants under a shift in position. Furthermore, turbulence is referred to as isotropic, if its statistics are invariants under rotations and reflections of the coordinate system (Pope, 2001).

2.2.2 Stochastic Description of Turbulence

The chaotic behaviour of turbulence motivates the stochastic description of the flow field, i. e., the consideration of the velocity at certain position and time as a random variable. Although turbulence is fully described by the deterministic Navier-Stokes equations (Eqs. 2.8, 2.14), the sensitivity of the evolution of the flow to tiny changes in initial and boundary conditions means that a fluid-flow experiment, that is carried out multiple times under specific conditions, does not necessarily lead to the same results in reality (Pope, 2001).

A random variable U can formally be defined as a variable whose values depend on outcomes of a random phenomenon (Blitzstein and Hwang, 2019). Single random

variables are fully described by the *cumulative distribution function* (CDF)

$$F_U(V) \equiv \mathbb{P}(U \leq V), \quad (2.19)$$

i. e., the probability that U will take a value less are equal to V . An equivalent and presumably more intuitive way to describe a random variable is the *probability density function* (PDF)

$$p_U(V) \equiv \frac{dF_U(V)}{dV} \quad (2.20)$$

which can be interpreted as the relative likelihood that the value of the random variable U equals V .

All distributions as well as the corresponding PDF and CDF mentioned in the framework of this thesis are given in Appendix A.

On the basis of the PDF, the *mean*

$$\langle U \rangle \equiv \int_{\mathbb{R}} V p(V) dV, \quad (2.21)$$

which is the average of all possible values of U weighted by its probability density, can be defined.

Since $p(V)$ cannot be measured directly in the sense of absolute certainty, different methods can be used to determine the mean. Thus, for example, the mean value of the time-dependent velocity $\mathbf{U}(\mathbf{x}_0, t)$ at a certain point in space \mathbf{x}_0 can either be approximated by the ensemble average

$$\langle \mathbf{U}(\mathbf{x}, t) \rangle_N \equiv \frac{1}{N} \sum_{n=1}^N \mathbf{U}^{(n)}(\mathbf{x}, t), \quad (2.22)$$

where $\mathbf{U}^{(n)}(\mathbf{x}, t)$ is the n -th measurement of $\mathbf{U}(\mathbf{x}, t)$ out of N realizations of the same experiment, or the time average

$$\langle \mathbf{U}(\mathbf{x}_0, t) \rangle_T \equiv \frac{1}{T} \int_{t_0}^{t_0+T} \mathbf{U}(\mathbf{x}_0, t) dt. \quad (2.23)$$

The latter is used as a measure for the mean in the context of this work and, if not made explicit otherwise, is denoted by $\langle \cdot \rangle$ for simplicity's sake. The approximation of the ensemble average by the time average is common practice in turbulence research (Pope, 2001). The underlying assumption that justifies this approximation is the ergodicity of turbulent flow, i. e., the idea that the statistics of an ensemble of realizations of a statistically stationary² flow field are equivalent to the statistics obtained from a sufficiently long time interval of one realization. Although there is no clear proof that turbulence is ergodic, numerical simulations by Galanti and Tsinober (2004) support the hypothesis at least under the precondition of spatial homogeneity.

Analogously to the mean, the *variance* $\text{var}(U)$ is defined as the probability-weighted average squared deviation from the mean:

$$\text{var}(U) \equiv \langle u^2 \rangle = \int_{\mathbb{R}} (V - \langle U \rangle)^2 p(V) dV \quad (2.24)$$

²Statistically stationary processes or those whose statistical properties do not change when shifted in time.

with $u \equiv U - \langle U \rangle$. The *standard deviation* σ is defined as the square root of the variance.

Another statistical measure which is of particular significance for the description of velocity increments is the *kurtosis*, as will become clear later on. It describes the shape of a distribution and is defined as (Pearson, 1905)

$$\text{Kurt}(U) \equiv \left\langle \left(\frac{U - \langle U \rangle}{\sigma} \right)^4 \right\rangle. \quad (2.25)$$

The kurtosis of any Gaussian distribution equals 3. Distributions with larger kurtosis are denoted as *leptokurtic* and are characterized by more pronounced outliers ("heavy tails") compared to a Gaussian distribution.

Within the theory of turbulent flows, where the velocity \mathbf{U} at certain time and position in space is considered random, the decomposition into an average term $\langle \mathbf{U} \rangle$ which is superimposed by fluctuations \mathbf{u} is known as *Reynolds decomposition* (Reynolds, 1895):

$$\mathbf{U} = \langle \mathbf{U} \rangle + \mathbf{u}. \quad (2.26)$$

On the basis of this description, *Taylor's hypothesis of frozen turbulence* (Taylor, 1938), which can be used to establish a link between time and location domain, is introduced. The hypothesis implies that velocity changes at a fixed point in space can be considered as the passage of a turbulent structure that is (on small time scales) assumed to be constant. The condition for its validity is that the velocity $\langle \mathbf{U} \rangle$ that is carrying the structure is much greater than the fluctuations of the velocity \mathbf{u} which represents the turbulence. Hence a time interval τ can be converted to a spatial shift \mathbf{r} via the mean velocity $\langle \mathbf{U} \rangle$:

$$\mathbf{r} = \langle \mathbf{U} \rangle \tau. \quad (2.27)$$

Especially in the context of aerodynamics, the standard deviation of the i -th velocity component in units of the mean velocity $\langle U \rangle$ is a frequently used measure for the intensity of wind velocity fluctuation (Pipinato, 2015) and therefore called *turbulence intensity* (TI) (Burton et al., 2001):³

$$\text{TI}_i \equiv \frac{\sigma_i}{\langle U \rangle} = \frac{\sqrt{\langle u_i^2 \rangle}}{\langle U \rangle}. \quad (2.28)$$

A more sophisticated statistical measure is the *covariance*

$$\begin{aligned} \text{cov}(U_1, U_2) &\equiv \langle (U_1 - \langle U_1 \rangle)(U_2 - \langle U_2 \rangle) \rangle \\ &= \langle U_1 U_2 \rangle - \langle U_1 \rangle \langle U_2 \rangle. \end{aligned} \quad (2.29)$$

If two random variables U_1, U_2 are not independent, the mean of the product of both does not equal the product of the individual means, i. e., $\text{cov}(U_1, U_2) \neq 0$. The covariance finds its application in the spatial description of turbulent flows where

³Note that there is no unique definition of this quantity in the literature. The *turbulence intensity* may be defined differently in other works, e. g., via the standard deviation of the velocity magnitude (further discussion: see Appendix B).

two velocity components, separated by a spatial shift \mathbf{r} , are considered (Mann, 1994):

$$\begin{aligned} R_{ij}(\mathbf{r}, \mathbf{x}, t) &\equiv \text{cov}[U_i(\mathbf{x}, t), U_j(\mathbf{x} + \mathbf{r}, t)] \\ &= \langle u_i(\mathbf{x}, t) u_j(\mathbf{x} + \mathbf{r}, t) \rangle. \end{aligned} \quad (2.30)$$

In this context, R_{ij} is also referred to as *two-point correlation*. For homogeneous turbulence, the two-point correlation is independent of \mathbf{x} by definition. In this case, the statistical information contained therein can equivalently be expressed as its Fourier transform—the *spectral tensor* (Pope, 2001)

$$\Phi_{ij}(\boldsymbol{\kappa}, t) \equiv \frac{1}{(2\pi)^3} \int_{\mathbb{R}^3} R_{ij}(\mathbf{r}, t) e^{-i\boldsymbol{\kappa}\cdot\mathbf{r}} d^3r. \quad (2.31)$$

$\boldsymbol{\kappa} = (\kappa_x, \kappa_y, \kappa_z)$ denotes the wave vector that contains the angular wavenumbers κ_i , i. e., the spatial angular frequencies, for each direction. Hence the (co-)variances of \mathbf{u} are given as

$$\langle u_i u_j \rangle = \int_{\mathbb{R}} \Phi_{ij}(\boldsymbol{\kappa}) d^3\kappa. \quad (2.32)$$

Another quantity, that is often considered, is the *energy spectrum*, which reduces the spectral tensor by its directional information and corresponds to the contribution of the wavenumber magnitude κ on the turbulent kinetic energy (per unit mass) k . Accordingly, the integral over the energy spectrum yields the total kinetic energy per unit mass:⁴

$$k \equiv \frac{1}{2} \langle u_i u_i \rangle = \int_0^\infty E(\kappa) d\kappa. \quad (2.33)$$

The energy spectrum itself is defined as follows (Batchelor and Townsend, 1949):

$$E(\kappa) \equiv \int_{\mathbb{R}^3} \frac{1}{2} \Phi_{ii}(\boldsymbol{\kappa}', t) \delta(|\boldsymbol{\kappa}'| - \kappa) d^3\kappa'. \quad (2.34)$$

Cross spectral analysis provides the determination of the relationship between two longitudinal velocity profiles as a function of the wavenumber of the respective direction. Without loss of generality, the x -direction is chosen as the longitudinal—i. e., the mean flow—direction throughout this work. Thereby, the *cross-spectrum* of two longitudinal velocity profiles with a transversal distance of Δy in y -direction and Δz in z -direction is given as (Mann, 1994)

$$\begin{aligned} \chi_{ij}(\kappa_x, \Delta y, \Delta z) &\equiv \frac{1}{2\pi} \int_{\mathbb{R}} R_{ij}(x, \Delta y, \Delta z) e^{-i\kappa_x x} dx \\ &= \int_{\mathbb{R}^2} \Phi_{ij}(\boldsymbol{\kappa}) e^{i(\kappa_y \Delta y + \kappa_z \Delta z)} d\kappa_y d\kappa_z. \end{aligned} \quad (2.35)$$

The normalization of the cross-spectrum with respect to the *one-point spectrum* $F_i(\kappa_x)$ of each velocity profile yields the *coherence* (Mann, 1994)

$$\text{coh}_{ij} \equiv \frac{|\chi_{ij}(\kappa_x, \Delta y, \Delta z)|^2}{F_i(\kappa_x) F_j(\kappa_x)}. \quad (2.36)$$

⁴This is also the reason for the prefactor of $\frac{1}{2}$ in Eq. 2.34.

For the case of full linear dependence, the coherence is unity, whereas the coherence vanishes, if there is no dependence whatsoever. The magnitude of the considered signals is immaterial for this quantity.

The one-point spectrum (or *power spectral density*) $F_i(\kappa_x)$ is given as (no summation)

$$\begin{aligned} F_i(\kappa_x) &= \int_{\mathbb{R}^2} \Phi_{ij}(\kappa) d\kappa_y d\kappa_z \\ &= \frac{1}{2\pi} \int_{\mathbb{R}} R_{ii}(x, 0, 0) e^{-i\kappa_x x} dx. \end{aligned} \quad (2.37)$$

This relation between power spectral density and two-point correlation is also denoted as the Wiener-Khintchin theorem (Wiener, 1930; Khintchine, 1934).

2.2.3 Richardson Cascade and Scales of Turbulent Motion

*Big whorls have little whorls
That feed on their velocity,
And little whorls have lesser whorls
And so on to viscosity.*

Lewis F. Richardson

Turbulent flows consist of eddies on a variety of spatial scales as can be seen in Fig. 2.3 by the example of a turbulent free jet stream. Richardson (1922) stated, that the largest eddies of the scale ℓ decay successively under submission of energy into smaller eddies until the energy is dissipated completely on the smallest length scale, the *dissipation length* l_μ , as he also memorably expressed in his famous poem. This phenomenon is denoted as *Richardson cascade* or *turbulent cascade*. The dissipation length is also referred to as *Kolmogorov length* and can, due to dimensional reasons, be expressed as

$$l_\mu = \left(\frac{\nu^3}{\varepsilon} \right)^{1/4}. \quad (2.38)$$

ε denotes turbulent dissipation rate per unit mass, i. e., the transformation of kinetic energy into internal energy, and ν denotes the kinematic viscosity. The intermediate



FIGURE 2.3: Turbulent free jet stream visualized by laser-induced fluorescence at $Re \approx 2300$. Taken from Dimotakis et al. (1981).

range of scales between l_u and ℓ is denoted as the *inertial subrange*. The flow dynamics within this subrange can be described under statistical assumptions and is the subject of the following section.

2.2.4 Kolmogorov 1941 Theory

Kolmogorov (1941a,b,c) stated three basic hypotheses that allow the derivation of laws for the statistics of the velocity increment

$$\mathbf{u}_r(\mathbf{x}, t) \equiv \mathbf{u}(\mathbf{x} + \mathbf{r}, t) - \mathbf{u}(\mathbf{x}, t), \quad (2.39)$$

where \mathbf{x} denotes a reference point and \mathbf{r} denotes an arbitrary spatial shift, for $\text{Re} \rightarrow \infty$ and small values of $|\mathbf{r}|$ directly from the Navier-Stokes equations. However, the direction of \mathbf{r} is commonly chosen as the direction of the mean flow, as is the case in the context of this work. The vector quantity \mathbf{u}_r can be reduced to the scalar longitudinal velocity increment:

$$u_r(\mathbf{x}, t) \equiv \mathbf{u}_r(\mathbf{x}, t) \cdot \frac{\mathbf{r}}{|\mathbf{r}|}. \quad (2.40)$$

Kolmogorov's hypotheses can be formulated as follows (Frisch, 1995):

1. For $\text{Re} \rightarrow \infty$ and far away from any boundaries, the statistics of u_r only depend on the magnitude of \mathbf{r} and are translational and rotational invariant.⁵ Therefore, the n -th moment of u_r (*structure function*)

$$S_n(r) \equiv \langle u_r^n(\mathbf{x}, t) \rangle \quad (2.41)$$

is only a function of $r = |\mathbf{r}|$.

2. $\exists h \in \mathbb{R}$ such that the statistics of $u_{\tilde{r}}$ with $\tilde{\mathbf{r}} = \lambda \mathbf{r}$ are the same as of $\lambda^h u_r$ for any $\lambda \in \mathbb{R}^+$. Therefore,

$$S_n(\lambda r) = \lambda^h S_n(r). \quad (2.42)$$

3. The turbulent flow has constant mean turbulent energy dissipation rate (per unit mass) ε . Together with the scale r , it determines the statistical properties of the flow. Hence by dimensional analysis the structure function can be expressed as

$$S_n(r) \propto (\varepsilon r)^{n/3}. \quad (2.43)$$

Based on these three assumption, the following exact relation for the third structure function can be derived from the Navier-Stokes equations (see, for example, Lewandowski and Pinier, 2016) which is also known as the *four-fifths law*:

$$S_3(r) = -\frac{4}{5} \varepsilon r. \quad (2.44)$$

⁵Translational and rotational invariance are the key characteristics of homogeneous isotropic turbulence.

For the incompressible and isotropic case of turbulence, the Wiener-Khinchin theorem (Khintchine, 1934; Wiener, 1930) provides the following expression for the energy spectrum (Frisch, 1995):

$$E(\kappa) = \frac{1}{\pi} \int_0^\infty \kappa r \langle \mathbf{u}(x) \cdot \mathbf{u}(x+r) \rangle \sin(\kappa r) dr. \quad (2.45)$$

Together with Eq. 2.43, this gives

$$E(\kappa) = c_K \varepsilon^{2/3} \kappa^{-5/3} \quad (2.46)$$

where the proportionality constant $c_K \approx 1.7$ (Schmidt et al., 2006) is denoted as *Kolmogorov constant*.

2.2.5 Intermittency

For his 1941 theory, Kolmogorov assumed self-similarity of the turbulent flow in the inertial subrange and thus the independence of its statistics of the considered spatial scale. However, experiments by Batchelor and Townsend (1949) demonstrated, in contradiction to Kolmogorov's theory, that spatial velocity derivatives follow a highly uneven spatial distribution for high wave numbers, i. e., for small scales. Kolmogorov (1962) recognized this contradiction to his 1941 theory (as well as Obukhov, 1962) and refined his initial theory by the assumption of the turbulent energy dissipation rate ε as a spatially fluctuating quantity. More precisely, ε on a spatial scale r_{n-1} is assumed to be randomly redistributed to smaller space elements present at smaller scales r_n with uncorrelated multipliers a_n for all n along the turbulent cascade, whereas the largest scale is denoted as ℓ . This concept is visualized in Fig. 2.4 and can be expressed as

$$\varepsilon_{r_n} = a_n \varepsilon_{r_{n-1}} = a_n a_{n-1} \varepsilon_{r_{n-2}} = \dots = \prod_{i=1}^n a_i \varepsilon_\ell \quad \text{with } \langle a_i \rangle = 1. \quad (2.47)$$

It follows directly that the logarithm

$$\log \frac{\varepsilon_{r_n}}{\varepsilon_\ell} = \log \left(\prod_{i=1}^n a_i \right) = \sum_{i=1}^n \log a_i \quad (2.48)$$

equals a sum of independent random variables $\log a_i$ for which the central limit theorem establishes a Gaussian distribution if n is sufficiently large. Thus, the transition

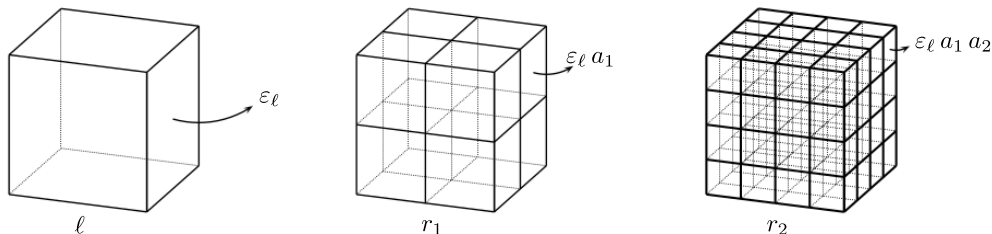


FIGURE 2.4: Visualization of the random redistribution of ε with multipliers a_i according to Kolmogorov (1962). Adapted from Laubrich (2009)

from discrete r_n to continuous r yields

$$p(\varepsilon_r) = p\left(\log \frac{\varepsilon_r}{\varepsilon_\ell}\right) = \frac{1}{2\pi\Lambda} \exp\left[-\frac{\left(\log \frac{\varepsilon_r}{\varepsilon_\ell}\right)^2}{2\Lambda^2}\right]. \quad (2.49)$$

$\Lambda^2 = \Lambda^2(r)$ denotes the variance for which a slight dependency on the scale r is permitted. Kolmogorov (1962) proposed

$$\Lambda^2(r) = A + \gamma \log \frac{r}{\ell} \quad (2.50)$$

with the phenomenological intermittency coefficient $\gamma \approx 0.227$ (Frisch, 1995). From Eqs. 2.49 and 2.50 follows (see Eq. 2.21)

$$\langle \varepsilon^{n/3} \rangle \propto r^{-\gamma \frac{n(n-3)}{18}}. \quad (2.51)$$

Analogously to Eq. 2.43, the structure function $S_n(r)$ can therefore be expressed as

$$S_n(r) \propto \langle \varepsilon^{n/3} \rangle r^{n/3} \propto r^{\frac{n}{3} - \gamma \frac{n(n-3)}{18}}. \quad (2.52)$$

In contrast to Eq. 2.42, which reflects the assumption of self-similarity within the whole inertial subrange, the shape of $S_n(r)$ is characterized by a dependency of the scale r . This scale-dependent behaviour is also reflected in the probability distribution of velocity increments u_r as shown in Fig. 2.5. For large spatial shifts r , the PDFs resemble a Gaussian distribution, whereas non-Gaussian behaviour, manifesting in heavy tails of the distribution, occurs for small values of r .⁶ This increased probability of extreme velocity increments is referred to as *intermittency*.

Intermittent velocity fluctuations have also been verified and well-documented for atmospheric turbulence (e.g., Boettcher et al., 2003). In this connection, it is common to speak of *gusts* as a term for excessive changes of the wind velocity within a short period of time.

2.2.6 Rapid Distortion Theory

Rapid distortion theory (RDT) denotes a method for describing turbulent air that is undergoing rapid stretching due to mean velocity gradients. It was developed for the analysis of fast changes in turbulent flows such as those related to the interaction between turbulent flow and solid boundaries.

In order to formulate this theory, the velocity and the pressure are considered in Reynolds decomposition (i. e., $\mathbf{U} = \langle \mathbf{U} \rangle + \mathbf{u}$ and $p = \langle p \rangle + p'$, see Eq. 2.26). First of all, the role of the thus resulting mean strain-rate

$$\bar{S}_{ij} \equiv \frac{1}{2} \left(\frac{\partial \langle U_i \rangle}{\partial x_j} + \frac{\partial \langle U_j \rangle}{\partial x_i} \right) \quad (2.53)$$

⁶Note that Fig. 2.5 shows the PDF in logarithmic manner. A Gaussian distribution therefore appears as a downward parabola.

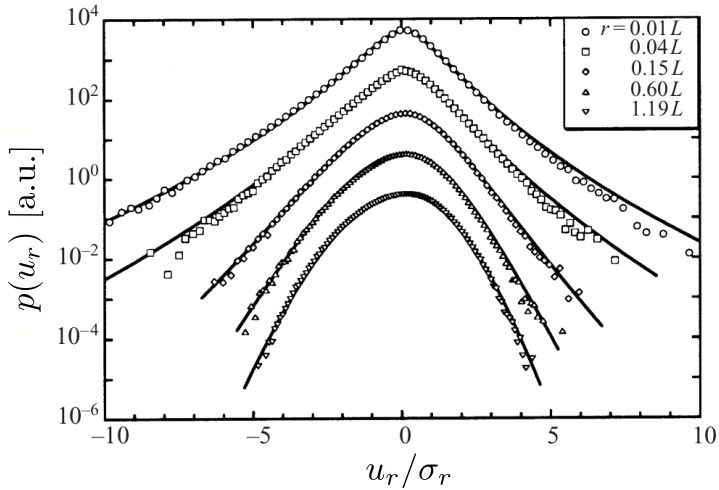


FIGURE 2.5: Probability density functions of velocity increments u_r for different spatial separations r from experimental data by Renner et al. (2001) and fits according to Castaing et al. (1990). The PDFs are shifted along the ordinate for the sake of clarity and normalized to their respective standard deviation σ_r .

(see Eq. 2.12) needs to be given closer attention at first. The magnitude of the tensor \bar{S}_{ij} is given as

$$\mathcal{S}(t) \equiv \sqrt{2 \bar{S}_{ij} \bar{S}_{ij}} \quad (2.54)$$

and its reciprocal value \mathcal{S}^{-1} represents a time scale for the mean shear. A time scale τ that represents the turbulent motion of the flow can be expressed as the ratio of turbulent kinetic energy (Eq. 2.33) and the turbulent dissipation rate (per unit mass): $\tau = k/\varepsilon$.⁷ The resulting turbulence-to-mean-shear ratio $\tau \mathcal{S}$ is typically in the order of 3 to 6 (Pope, 2001). In the *rapid-distortion limit*, however, the ratio is assumed to be arbitrarily large.

With the Reynolds decomposition for \mathbf{U} and p , the continuity equation (Eq. 2.8) can be rephrased as follows:

$$\frac{\partial \langle U_i \rangle}{\partial x_i} = \frac{\partial u_i}{\partial x_i} = 0. \quad (2.55)$$

Similarly, the momentum equation (NSE, Eq. 2.14) can be transformed into the *Reynolds equation* (Reynolds, 1883)

$$\frac{\overline{D}\langle U_i \rangle}{\overline{D}t} = -\frac{1}{\rho} \frac{\partial \langle p \rangle}{\partial x_i} + \nu \nabla^2 \langle U_i \rangle + \langle f \rangle - \frac{\partial \langle u_i u_j \rangle}{\partial x_j} \quad (2.56)$$

where the differential operator

$$\frac{\overline{D}}{\overline{D}t} \equiv \frac{\partial}{\partial t} + \langle U_i \rangle \frac{\partial}{\partial x_i} \quad (2.57)$$

⁷In a strict sense, the Kolmogorov time scale $\tau_\mu = (\nu/\varepsilon)^{1/2}$ (analogous to the Kolmogorov length scale, Eq. 2.38) needs to be considered if RDT is to be applied to all scales of turbulent motion.

is defined in analogy to Eq. 2.3. The Poisson equation for the mean pressure can be expressed as

$$\nabla^2 \langle p \rangle = -\rho \frac{\partial \langle U_i \rangle}{\partial x_j} \frac{\partial \langle U_j \rangle}{\partial x_i} - \frac{\partial^2 \langle u_i u_j \rangle}{\partial x_i \partial x_j} + \frac{\partial \langle f_i \rangle}{\partial x_i} \quad (2.58)$$

A Poisson equation for the pressure fluctuations $p' \equiv p - \langle p \rangle$ can be obtained by subtraction of Eq. 2.58 from Eq. 2.15. Lastly, by assuming a constant volume force, i. e., $f_i = \langle f_i \rangle$, follows that

$$\nabla^2 p' = -2\rho \frac{\partial \langle U_i \rangle}{\partial x_j} \frac{\partial u_j}{\partial x_i} - \rho \frac{\partial^2}{\partial x_i \partial x_j} (u_i u_j - \langle u_i u_j \rangle). \quad (2.59)$$

Moreover, the pressure fluctuation p' can be decomposed in an analytically meaningful manner (Pope, 2001):

$$p' = p^r + p^s + p^h. \quad (2.60)$$

p^r , p^s and p^h denote the *rapid*, *slow* and *harmonic* pressure, respectively, and satisfy following equations:

$$\nabla^2 p^r = -2\rho \frac{\partial \langle U_i \rangle}{\partial x_j} \frac{\partial u_j}{\partial x_i}, \quad (2.61)$$

$$\nabla^2 p^s = -\rho \frac{\partial^2}{\partial x_i \partial x_j} (u_i u_j - \langle u_i u_j \rangle), \quad (2.62)$$

$$\nabla^2 p^h = 0. \quad (2.63)$$

The reason for these denotations is that the rapid pressure responds instantaneously (*rapidly*) to changes of the mean velocity gradient $\partial \langle U_i \rangle / \partial x_j$ in contrast to the slow pressure. The denotation of the harmonic pressure arises from the fact that it is a solution of the Laplace equation and thus a *harmonic function* by definition (Gilbarg and Trudinger, 2015).

The evolution of the velocity fluctuations u_i can be obtained by subtraction of the Reynolds equation from the NSE:

$$\frac{\bar{D}u_i}{\bar{D}t} = -\frac{1}{\rho} \frac{\partial p'}{\partial x_i} + \nu \nabla^2 u_i + -u_j \frac{\partial \langle U_i \rangle}{\partial x_j} - u_j \frac{\partial u_i}{\partial x_j} \quad (2.64)$$

where the pressure fluctuations are following Eq. 2.59.

Both the first term of the right-hand side of Eq. 2.64 and the rapid pressure p^r represent the interaction between the turbulent velocity fluctuations u_i and the mean velocity gradient $\partial U_i / \partial x_j$. In contradiction to the remaining terms, which represent turbulence-turbulence-interaction, they scale linearly with S . Thus, in the limit of rapid distortion, the remaining terms can be neglected and as a result, the rapid-distortion equations

$$\frac{\bar{D}u_i}{\bar{D}t} = -\frac{1}{\rho} \frac{\partial p^r}{\partial x_i} - u_i \frac{\partial \langle U_i \rangle}{\partial x_i}, \quad (2.65)$$

$$\nabla^2 p = -2\rho \frac{\partial \langle U_i \rangle}{\partial x_j} \frac{\partial u_j}{\partial x_i}. \quad (2.66)$$

arise. Eq. 2.65 forms the basis for the description of the temporal evolution of the spectral velocity tensor in the wind model by Mann (1994) in Section 2.3.1.

2.2.7 Atmospheric Turbulence

The lowest part of the Earth's atmosphere, adjacent to the surface, is the atmospheric boundary layer (ABL), which reaches up to about 3000 m above the ground (Stull, 2012). The transport processes within the ABL are a fundamental driving force of the Earth's weather and it is characterized by the highest degree of turbulent motion in all atmospheric layers (Holtslag, 2015).

The occurrence of atmospheric turbulence is mainly caused by forcing from the Earth's surface. Firstly, turbulence is mechanically triggered by the terrain's roughness, i. e., obstacles like buildings and the contours of the terrain, also denoted as *orography* (Vallis and Roads, 1986). The surface roughness is usually quantified by the *roughness length* z_0 (Burton et al., 2001). Secondly, solar heating of the Earth's surface causes thermal convection through buoyancy. Above a critical temperature difference between overlying air layers, density differences that are caused by thermal expansion lead to an upward motion while at the same time cooled, less dense layers of air exhibit downward motion in accordance to Archimedes' principle. The influence of thermal convection is usually categorized into the following three states (Burton et al., 2001):

1. Stable stratification: As a parcel of air rises, the pressure reduction and the associated expansion of the air lead to a drop in temperature as the internal energy increases (adiabatic cooling). This prevents vertical motion of the air.
2. Neutral stratification: The adiabatic cooling of the air while rising takes place in such way that it is always in thermal equilibrium with the surrounding. This case is typical for strong winds at intense turbulence and is hence of great importance for wind energy applications, particularly for wind turbine loads.
3. Unstable stratification: Due to intense solar heating, lifting of air parcels due to thermal convection can not be compensated by adiabatic cooling. The accompanying mixing of the air leads to relatively low vertical gradient of the mean wind speed.

A further mechanism for the occurrence of atmospheric turbulence is the Kelvin-Helmholtz instability (Helmholtz, 1868; Thomson, 1871) which denotes the onset of turbulent flow in case of velocity shear, i. e., at velocity difference across the interface between fluid layers. Such is the case at sufficiently large vertical velocity gradients in the ABL (North et al., 2014).

The wind dynamics within the ABL are moreover influenced by the Coriolis force due to Earth's rotation.

Mean Wind Profile

For low heights z and neutral stratification, the mean wind profile $\langle U \rangle(z)$ scales logarithmically with the height (Burton et al., 2001):

$$\langle U \rangle(z) \propto \ln \frac{z}{z_0} : \quad (2.67)$$

A common approximation of the vertical mean wind profile is given by the following power law

$$\langle U \rangle(z) \propto z^a \quad (2.68)$$

where the shear exponent is given by $a = 1/7 \approx 0.143$ for neutral conditions (Schlichting and Gersten, 2016). Within the scope of the Mann turbulence model (Section 2.3.1), $\langle U \rangle(z)$ is further simplified and considered linear.

Von Kármán Energy Spectrum

In order to expand the description of the energy spectrum established by Kolmogorov (1941a,b,c) by the finite outer scales of atmospheric turbulence beyond the inertial subrange, different approaches have been made. In the context of wind energy research, the Kaimal and the von Kármán spectrum have primarily been established (Burton et al., 2001). The latter forms the basis for the Mann turbulence model which is utilized in the present work and is given as (Kármán, 1948)

$$E(\kappa) = c_K \varepsilon^{2/3} L^{5/3} \frac{(L \kappa)^4}{[1 + (L \kappa)^2]^{17/6}}. \quad (2.69)$$

with a length scale L . The von Kármán spectrum, in comparison to the $-5/3$ behaviour according to Eq. 2.46, is shown in Fig. 2.6

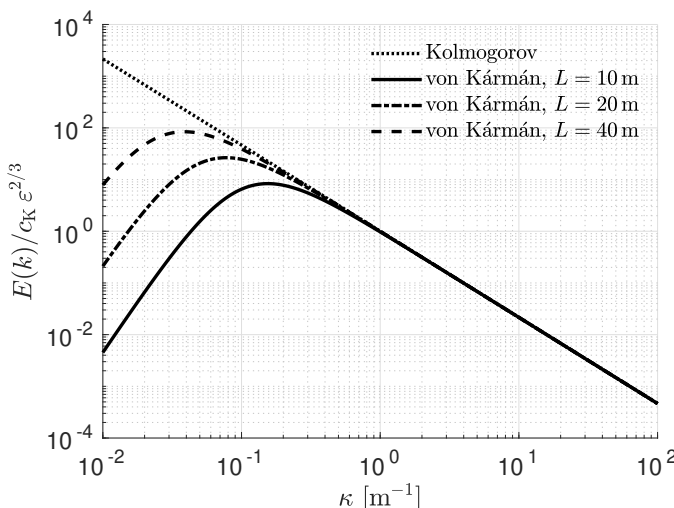


FIGURE 2.6: The Kolmogorov spectrum (Eq. 2.46) and the von Kármán spectrum (Eq. 2.69) for different exemplary values of the length scale L in comparison.

2.3 Wind Field Models

2.3.1 The Mann Turbulence Model

The *Mann turbulence model* (Mann, 1994, 1998) aims to capture the complete second-order statistics of homogeneous, neutrally stratified atmospheric boundary layer turbulence in the form of the spectral velocity tensor Φ_{ij} (Eq. 2.31). The basis of the model is an application of Rapid Distortion Theory (see Section 2.2.6) implying a linearization of the Navier-Stokes equation as well as a definition and modeling of eddy lifetimes. The resulting spectral velocity tensor and hence the modeled stationary turbulent velocity field $\mathbf{u}(\mathbf{x})$ (considered in Reynolds decomposition, Eq. 2.26) are dependent on only three parameters: a lengthscale L , a non-dimensional parameter Γ as a measure for the eddy lifetime and a factor $c_K \varepsilon^{2/3}$ where $c_K \approx 1.7$ (Schmidt et al., 2006) is the three-dimensional Kolmogorov constant and ε the turbulent dissipation rate per unit mass.

The mapping from the modelled tensor $\Phi_{ij}(\boldsymbol{\kappa})$ to the velocity field $\mathbf{u}(\mathbf{x})$ takes place via a generalized stochastic Fourier-Stieltjes integral⁸ (Batchelor, 2000)

$$\mathbf{u}(\mathbf{x}) = \int_{\mathbb{R}^3} e^{i \boldsymbol{\kappa} \cdot \mathbf{x}} d\mathbf{Z}(\boldsymbol{\kappa}). \quad (2.70)$$

The stochastic process \mathbf{Z} is defined by following properties (Mann, 1998):

$$\langle dZ_i(\boldsymbol{\kappa}') dZ_j^*(\boldsymbol{\kappa}'') \rangle = 0 \quad \text{for } \boldsymbol{\kappa}' \neq \boldsymbol{\kappa}'', \quad (2.71)$$

$$\frac{\langle dZ_i(\boldsymbol{\kappa}) dZ_j^*(\boldsymbol{\kappa}) \rangle}{d\kappa_x d\kappa_y d\kappa_z} = \Phi_{ij}(\boldsymbol{\kappa}). \quad (2.72)$$

Eq. 2.71, which depicts that the increments of \mathbf{Z} are uncorrelated, represents the assumed homogeneity of the turbulence whereas Eq. 2.72 provides the connection between Φ_{ij} and \mathbf{u} .

The mean velocity of the wind is assumed as a uniform shear with the mean flow in x direction:

$$\langle \mathbf{U} \rangle(\mathbf{x}) = z \frac{d\langle U \rangle}{dz} \hat{\mathbf{x}}. \quad (2.73)$$

$\hat{\mathbf{x}}$ denotes the unit vector in x direction. The symmetry group of the model is thus given as

$$\left\{ \mathbb{1}, \begin{pmatrix} 1 & 0 & 0 \\ 0 & -1 & 0 \\ 0 & 0 & 1 \end{pmatrix} \begin{pmatrix} -1 & 0 & 0 \\ 0 & 1 & 0 \\ 0 & 0 & -1 \end{pmatrix}, -\mathbb{1} \right\}, \quad (2.74)$$

where $\mathbb{1}$ denotes the unit matrix. The field $\mathbf{u}(\mathbf{x})$ is therefore invariant under inversion of all coordinates as well as under inversion of the y axis or simultaneous inversion of both x and z axis.

The modeling of the spectral velocity tensor can be divided into two parts which are described in the following.

⁸Reason for this approach the fact that $\mathbf{u}(\mathbf{x})$ is not square-integrable over \mathbb{R}^3 . The Fourier transform therefore does not exist. One alternative example to circumvent this problem is the representation of $\mathbf{u}(\mathbf{x})$ as Fourier series under the assumption of cyclic boundary conditions (Townsend, 1976).

First Step: Isotropic Turbulence

For the simple case of isotropic turbulence (i. e., no shear assumed), the spectral tensor has generally the following form (Pope, 2001):

$$\Phi(\kappa) = \frac{E(\kappa)}{4\pi\kappa^4} (\delta_{ij}\kappa^2 - \kappa_i\kappa_j). \quad (2.75)$$

Hence it can be fully described by the energy spectrum $E(\kappa)$ (Eq. 2.34) for which the von Kármán spectrum with the parameters $c_K \varepsilon^{2/3}$ and L is chosen (Eq. 2.69; Kármán, 1948). Substitution leads to

$$\Phi_{\text{iso}}(\kappa) = \frac{c_K \varepsilon^{2/3} L^{17/3}}{4\pi} \frac{\delta_{ij}\kappa - \kappa_i\kappa_j}{[1 + (L\kappa)^2]^{17/6}}. \quad (2.76)$$

The corresponding one-point spectra can now be obtained from the spectral tensor via

$$F_i(\kappa_x) = \int_{\mathbb{R}^2} \Phi_{ij}(\kappa) d\kappa_y d\kappa_z \quad (2.77)$$

(see Eqs. 2.35, 2.37). For the isotropic case, this leads to

$$F_i(\kappa_x) = \begin{cases} \frac{9}{55} c_K \varepsilon^{2/3} \frac{1}{(1+L^2\kappa_x^2)^{5/6}} & \text{for } i = 1, \\ \frac{3}{110} c_K \varepsilon^{2/3} \frac{3+8L^2\kappa_x^2}{(1+L^2\kappa_x^2)^{11/6}} & \text{for } i \in \{2, 3\}, \end{cases} \quad (2.78)$$

as shown in Fig. 2.7 and as a result, following variances for the velocity field arise (see Eq. 2.32):

$$\sigma_{\text{iso}}^2 = \sigma_x^2 = \sigma_y^2 = \sigma_z^2 = \frac{9}{55} \frac{\sqrt{\pi} \Gamma\left(\frac{1}{3}\right)}{\Gamma\left(\frac{5}{6}\right)} c_K \varepsilon^{2/3} L^{2/3} \approx 0.688 c_K \varepsilon^{2/3} L^{2/3}. \quad (2.79)$$

Γ denotes the Euler Gamma function.⁹

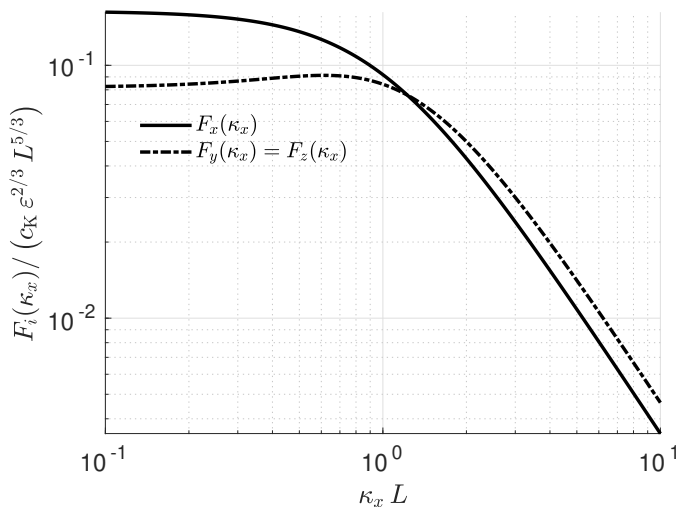


FIGURE 2.7: One-point spectra $F_i(\kappa_x)$ of the isotropic case of the Mann turbulence model (Eq. 2.78).

⁹ $\Gamma(z) \equiv \int_0^\infty x^{z-1} e^{-x} dx$ for $\text{Re}(z) > 0$.

Second Step: Extension to Non-Isotropic Turbulence

To estimate the influence of the mean shear on the turbulent flow field, RDT as described in the preceding section is applied. The consequent time-dependent velocity field is then transferred to a stationary field by substituting the time by a modeled lifetime of the eddies within the turbulent flow.

The fundamental assumption upon which Mann (1994) models the eddy lifetime τ_E is that vortices of size κ^{-1} are destroyed primarily by vortices that are smaller or of the same order of magnitude. Mann (1994) suggests the approximation of their corresponding characteristic velocity by the square rooted integral $(\int_{\kappa}^{\infty} E(\kappa') d\kappa')^{1/2}$ over the energy spectrum (von Kármán spectrum; Eq. 2.69). Moreover, the lifetime of an eddy τ_E is assumed to be proportional to its size κ^{-1} divided by the mentioned characteristic velocity:

$$\tau_E \propto \kappa^{-1} / \sqrt{\int_{\kappa}^{\infty} E(\kappa') d\kappa'} \quad (2.80)$$

$$\propto \kappa^{-2/3} \left[{}_2F_1 \left(\frac{1}{3}, \frac{17}{6}; \frac{4}{3}; -(\kappa L)^{-2} \right) \right]^{-1/2} \quad (2.81)$$

$$\propto \begin{cases} \kappa^{-3/3} & \text{for } \kappa \rightarrow \infty \\ \kappa^{-1} & \text{for } \kappa \rightarrow 0 \end{cases}. \quad (2.82)$$

${}_2F_1$ denotes the Gaussian hypergeometric function (see, for example, Erdélyi, 1953). Since small scales are of main interest, it is sufficient to consider high wavenumbers and therefore $\tau_E \propto \kappa^{-2/3}$ (Mann, 1998). For dimensional reason, the parameter $\Gamma \geq 0$ is introduced so that

$$\tau_E = \Gamma \left(\frac{d\langle U \rangle}{dz} \right)^{-1} (\kappa L)^{-2/3}. \quad (2.83)$$

Furthermore, a non-dimensional lifetime β_E can be defined as

$$\beta_E \equiv \frac{d\langle U \rangle}{dz} \tau_E = \Gamma (\kappa L)^{-2/3}. \quad (2.84)$$

Fourier-Stieltjes transformation of the RDT momentum equation (Eq. 2.65) via the integral in Eq. 2.70 yields

$$\frac{DdZ_i(\boldsymbol{\kappa}(t), t)}{Dt} = \frac{d\langle U \rangle}{dz} \left(2 \frac{\kappa_i \kappa_x}{\kappa^2} - \delta_{i1} \right) dZ_3(\boldsymbol{\kappa}(t), t). \quad (2.85)$$

The temporal evolution of the wavenumber is further described by (Pope, 2001)

$$\frac{d\kappa_i(t)}{dt} = -\kappa_j(t) \frac{\partial \langle U_j \rangle}{\partial x_i}. \quad (2.86)$$

Eqs. 2.86 and 2.85 can be solved with the initial conditions $\kappa(t = 0) = \boldsymbol{\kappa}_0 = (\kappa_x, \kappa_y, \kappa_z)$ where $\kappa_z = \kappa_z(t = 0)$ and $dZ(\boldsymbol{\kappa} = \boldsymbol{\kappa}_0, t = 0)$. Furthermore, the time t can be expressed in terms of the non-dimensional time $\beta \equiv d\langle U \rangle / dz t$.

Following solutions result:

$$\kappa(\beta) = (\kappa_x, \kappa_y, \kappa_z(\beta)) \quad \text{with } \kappa_z(\beta) = \kappa_{z0} - \beta \kappa_x, \quad (2.87)$$

$$dZ(\kappa, \beta) = \begin{pmatrix} 1 & 0 & \xi_1 \\ 0 & 1 & \xi_2 \\ 0 & 0 & \kappa_0^2/\kappa^2 \end{pmatrix} dZ(\kappa_0, 0). \quad (2.88)$$

The occurring variables are given as follows:

$$\xi_1 = C_1 - \frac{\kappa_y}{\kappa_x} C_2, \quad (2.89)$$

$$\xi_2 = \frac{\kappa_y}{\kappa_y} C_1 + C_2, \quad (2.90)$$

$$C_1 = \frac{\beta \kappa_x^2 (\kappa_0^2 - 2 \kappa_{z0}^2 + \beta \kappa_x \kappa_{z0})}{\kappa^2 (\kappa_x^2 + \kappa_y^2)}, \quad (2.91)$$

$$C_1 = \frac{\kappa_y \kappa_0^2}{\sqrt{\kappa_x^2 + \kappa_y^2}} \arctan \left(\frac{\beta \kappa_x \sqrt{\kappa_x^2 + \kappa_y^2}}{\kappa_0^2 - \kappa_{z0} \kappa_x \beta} \right). \quad (2.92)$$

Finally, an explicit expression for the temporal evolution $\Phi(\kappa, \beta)$ of the spectral tensor is obtained by substitution of the increment $dZ(\kappa, \beta)$ into Eq. 2.72. Furthermore, stationarity is obtained by substitution of β by the non-dimensional eddy-lifetime β_E , given by Eq. 2.84. The resulting components of the stationary spectral tensor, that provide the core component of the Mann turbulence model, are given by (Mann, 1994)

$$\Phi_{11} = \frac{E(\kappa_0)}{4 \pi \kappa_0^4} \left[\kappa_0^2 - \kappa_x^2 - 2 \kappa_x \kappa_{z0}^2 \xi_1 + (\kappa_x^2 + \kappa_y^2) \xi_1^2 \right], \quad (2.93)$$

$$\Phi_{22} = \frac{E(\kappa_0)}{4 \pi \kappa_0^4} \left[\kappa_0^2 - \kappa_y^2 - 2 \kappa_y \kappa_{z0}^2 \xi_2 + (\kappa_x^2 + \kappa_y^2) \xi_2^2 \right], \quad (2.94)$$

$$\Phi_{33} = \frac{E(\kappa_0)}{4 \pi \kappa_0^4} (\kappa_x^2 + \kappa_y^2), \quad (2.95)$$

$$\Phi_{12} = \Phi_{21} = \frac{E(\kappa_0)}{4 \pi \kappa_0^2 4} \left[-\kappa_x \kappa_y - \kappa_x \kappa_{z0} \xi_2 - \kappa_y \kappa_{z0} \xi_1 + (\kappa_x^2 + \kappa_y^2) \xi_1 \xi_2 \right], \quad (2.96)$$

$$\Phi_{13} = \Phi_{31} = \frac{E(\kappa_0)}{4 \pi \kappa_0^2 \kappa^2} \left[-\kappa_x \kappa_{z0} + (\kappa_x^2 + \kappa_y^2) \xi_1 \right], \quad (2.97)$$

$$\Phi_{23} = \Phi_{32} = \frac{E(\kappa_0)}{4 \pi \kappa_0^2 \kappa^2} \left[-\kappa_y \kappa_{z0} + (\kappa_x^2 + \kappa_y^2) \xi_2 \right]. \quad (2.98)$$

Integration of the spectral tensor with respect to all wavenumber components returns the (co-) variances. As seen in Fig. 2.8, the variances of the x - and y -component of the turbulent velocity fluctuations become larger with increasing Γ , i. e., with increasing influence of the shear, whereas the variance of u_z is decreasing. $\sigma_x^2 > \sigma_y^2 > \sigma_z^2$ is consistent with meteorological data (e. g., Bortoli et al., 2000; Tampieri et al., 2016).

Furthermore, Mann (1994) validated the model experimentally by comparison of the model spectra to experimental data measured with sonic anemometry at the Danish island Sprogø (Mann et al., 1991). The measurement was performed against the background of the building of the Great Belt Bridge between the Danish islands of

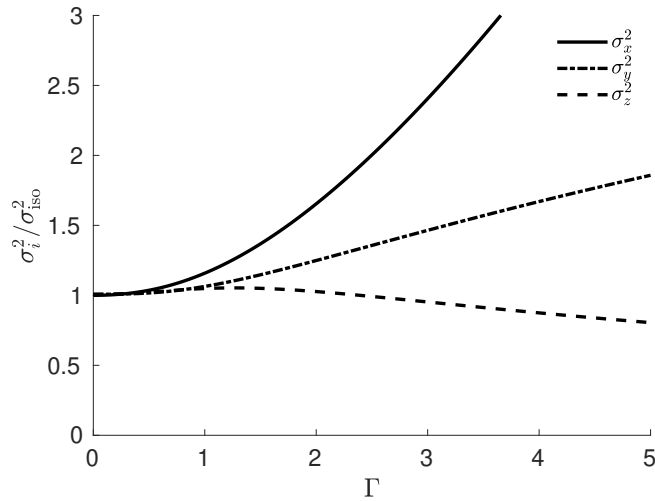


FIGURE 2.8: Variances in units of the variance in the isotropic case (Eq. 2.79) of the velocity components as function of Γ .

Zealand and Funen for which cross-spectra were of great importance for the estimation of dynamic loads on the bridge.

Figure 2.9 shows the comparison of the spectra $F_i(\kappa_x)$ of model and measured data and the comparison of the coherence $\text{coh}_{ii}(\kappa_x)$ (no summation) of model and measured data, respectively. As the figures imply, the spectra are in good agreement with the observations, whereas the model coherences fit the measurement data for small horizontal separations Δy and show significant deviation for large values of Δy .

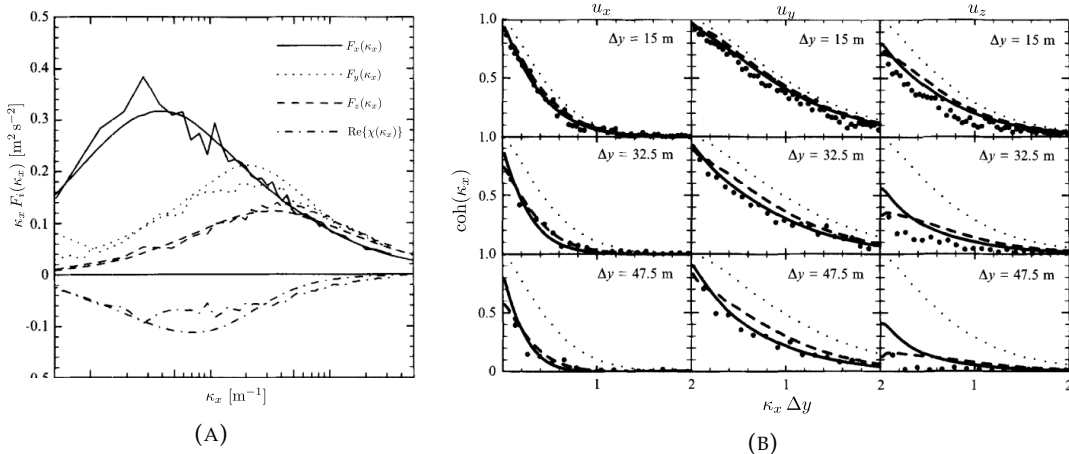


FIGURE 2.9: Comparison of the model with data from the Great Belt coherence experiment (Mann et al., 1991). (A) Fit of the model spectra (smooth lines) to the data (ragged lines). (B) Measured (dots) and predicted coherence (solid lines). Dashed lines in (B) label predicted coherence from an alternative model, the dotted lines correspond to isotropic inertial-range coherence that are valid for very small Δy (Harris, 1970; Kristensen and Jensen, 1979). Taken from Mann (1994).

Fourier simulation

The numerical simulation of the modelled velocity field is based on the approximation of Eq. 2.70 by the Fourier series (Mann, 1998)

$$u_i(\mathbf{x}) = \sum_{\boldsymbol{\kappa}} e^{i\boldsymbol{\kappa} \cdot \mathbf{x}} C_{ij}(\boldsymbol{\kappa}) v_j(\boldsymbol{\kappa}), \quad (2.99)$$

defined on the discrete set $\mathcal{B} = \{\mathbf{x} \mid x_i = n L_i : n = 1, \dots, n_i\}$ (see Fig. 2.10) as the sum over all wave vectors in $\{\boldsymbol{\kappa} \mid \kappa_i = m 2\pi/L_i : m = -n_i/2, \dots, n_i/2\}$. $v_j(\boldsymbol{\kappa}) \in \mathbb{C}$ denote independent stochastic variables of which both real and imaginary part obey the normal distribution with unit variance. The coefficients $C_{ij}(\boldsymbol{\kappa})$ are approximately

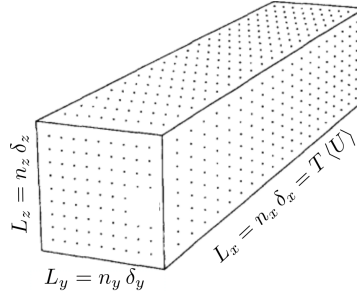


FIGURE 2.10: Box \mathcal{B} that represents the definition set of the Fourier simulated velocity field. Applying Taylor's hypothesis (Eq. 2.27) with mean wind speed $\langle U \rangle$ to the x axis allows simulations of total time T .

Adapted from Mann (1998).

given by

$$C_{ij}(\boldsymbol{\kappa}) v_j(\boldsymbol{\kappa}) = \frac{1}{L_x L_y L_z} \int_{\tilde{\mathcal{B}}} u_i(\mathbf{x}) e^{-i\boldsymbol{\kappa} \cdot \mathbf{x}} d^3x \quad (2.100)$$

where $\tilde{\mathcal{B}} = [0, L_x] \times [0, L_y] \times [0, L_z]$ denotes the volume in which the modeled turbulent field is defined. Taking the covariance tensor leads to

$$C_{ik}^*(\boldsymbol{\kappa}) C_{jk}(\boldsymbol{\kappa}) = \frac{1}{L_x^2 L_y^2 L_z^2} \int_{\tilde{\mathcal{B}} \times \tilde{\mathcal{B}}} \langle u_i(\mathbf{x}) u_j(\mathbf{x}') \rangle e^{i\boldsymbol{\kappa} \cdot (\mathbf{x} - \mathbf{x}')} d^3x d^3x' \quad (2.101)$$

$$= \int_{\mathbb{R}^3} \Phi_{ij}(\boldsymbol{\kappa}') \prod_{l=1}^3 \text{sinc}^2 \left[\frac{(\kappa_l - \kappa'_l) L_l}{2} \right] d^3\kappa'. \quad (2.102)$$

For $L_l \gg L$, $\text{sinc}^2 \left[(\kappa_l - \kappa'_l) L_l / 2 \right]$ is only different from zero for $\kappa_l \approx \kappa'_l$ and its total integral is given as $2\pi/L_l$. This simplifying condition is given for $l = 3$, i. e., $L_x \gg L$ for many applications as well as in the present case. Consequently, the following applies:

$$C_{ik}^*(\boldsymbol{\kappa}) C_{jk}(\boldsymbol{\kappa}) = \frac{2\pi}{L_x} \int_{\mathbb{R}^2} \Phi_{ij}(\kappa_x, \kappa'_y, \kappa'_z) \prod_{l=2}^3 \text{sinc}^2 \left[\frac{(\kappa_l - \kappa'_l) L_l}{2} \right] d\kappa_y d\kappa_z. \quad (2.103)$$

A detailed derivation of the above equations is given by Mann (1998). The corresponding software tool (DTU Wind Energy, 2018) for the Fourier simulation that is utilized for this work is part of the aeroelastic¹⁰ tool HAWC2 (*Horizontal Axis Wind*

¹⁰The research field of aeroelasticity deals with the interaction between a fluid flow and elastic bodies (e. g., wind turbines) that are exposed to it.

turbine simulation Code, 2nd generation), developed at the Risø DTU National Laboratory for Sustainable Energy (Larsen and Hansen, 2007).

2.3.2 The CTRW Model

The concept of *Random Walks* is a model for random processes that can be described as the succession of random steps on some mathematical space and is used in a wide range of applications. In the field of financial theory, for instance, the *Random Walk Hypothesis* states that the evolution of stock market prices can be described by a Random Walk and is thus unpredictable (Cootner, 1967). Another prime example for a Random Walk is the trajectory of particles in a fluid, denoted as Brownian motion (Knight, 1962).

In most cases, the waiting time between two successive steps of a Random Walk (RW) is regarded as constant. As a consequence, the time variable does not have to be regarded further and the state of the RW can simply be described by the current number of preceding steps. For some applications, however, it is suitable to consider a more generalized concept of Random Walks. Accordingly, Montroll and Weiss (1965) proposed an expansion of the model by waiting times between successive steps that are as well random, constituting the so-called Continuous-Time Random Walks (CTRW) model. Fig. 2.11 clarifies the difference between classical RWs and CTRWs.

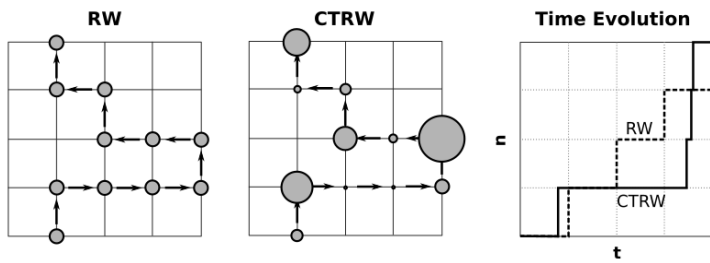


FIGURE 2.11: Comparison of a classical RW (left) and a CTRW (middle) through the example of the movement on a two-dimensional lattice. The size of the circular areas correspond to the waiting time at the respective position. The figure on the right shows the corresponding number of steps n as function of the time t . Taken from Kleinhans (2008).

As explained in Section 2.2.5, turbulent flow is, inter alia, characterized by anomalous scaling behaviour which is reflected by the occurrence of intermittency. Friedrich (2003) could demonstrate that CTRWs are suitable for the description of this phenomenon. On this basis, Kleinhans (2008) established a two-folded CTRW-based wind model. In a first step, a velocity time series $u(s)$ as a function of a model-intrinsic time scale s is generated as a coupled Ornstein-Uhlenbeck process. Since the paths of CTRWs are generally discontinuous¹¹, s is considered instead of the the number of steps n . Since this first step is not subject of this study, further definition is omitted here. The second part of Kleinhans' model—the centerpiece of the time series generation—is given by the stochastic time mapping process (Fogedby, 1994)

$$\frac{dt(s)}{ds} = \tau_\alpha(s) \quad (2.104)$$

¹¹The term "continuous" in "Continuous-Time Random Walk" refers solely to the time at which the steps of the walk take place.

that leads to intermittent dynamics of the velocity. τ_α are uncorrelated random numbers that obey the PDF (Kleinhans, 2008)

$$p_\alpha(V) = \frac{1}{\pi} \operatorname{Re} \left\{ \int_0^\infty \exp \left[-i \xi V - \xi^\alpha \exp \left(-i \frac{\pi \alpha}{2} \right) \right] d\xi \right\} \quad (2.105)$$

which belongs to the family of Lévy distributions (Lévy, 1925). The distribution is shown in Fig. 2.12 for exemplary values of α . It turns into the Dirac distribution at $\alpha = 0$ and $\alpha = 1$:

$$p_{\alpha=0}(V) = \delta(V), \quad (2.106)$$

$$p_{\alpha=1}(V) = \delta(1-V). \quad (2.107)$$

Thus, $t(s) = s$ for $\alpha = 1$. For $\alpha < 1$, the mean does not exist. For any finite data,

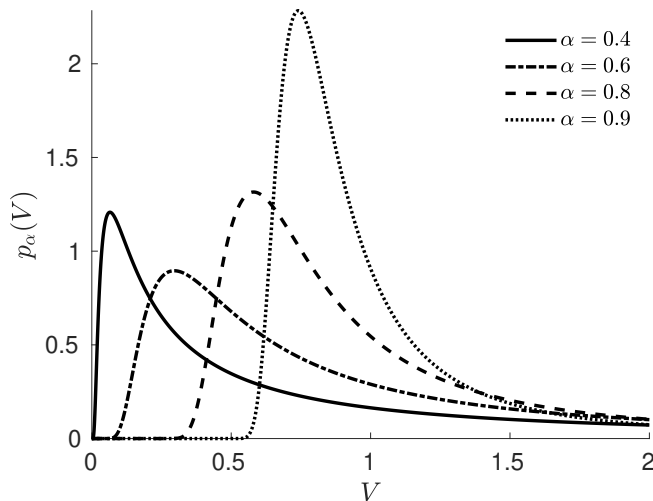


FIGURE 2.12: Lévy distribution according to Eq. 2.105 for exemplary values for α .

however, mean and variance do exist. In order to take this into account, a truncated Lévy distribution that vanishes above some given cutoff c , is considered:

$$p_{\alpha,c}(V) \equiv \begin{cases} p_\alpha(V) / \int_0^c p_\alpha(V') dV' & \text{for } V \leq c \\ 0 & \text{for } V > c. \end{cases} \quad (2.108)$$

The respective waiting time is denoted accordingly as $\tau_{\alpha,c}$.

Eq. 2.104 in its discretized form can be represented as (Kleinhans, 2008)

$$t(s_{i+1}) = t(s_i) + C(\alpha, c, \Delta s_t) \tau_{\alpha,c}(s). \quad (2.109)$$

In practice, $t(s)$ is only computed at certain points with increment Δs_t , as illustrated in Fig. 2.13. Between those points, linear interpolation is applied. Since $\tau_{\alpha,c}(s)$ does not follow a stable¹² distribution for finite $c < \infty$, the process $t(s)$ varies depending

¹²A distribution is denoted as stable if a linear combination of two independent random variables from the same distribution follows again the distribution of the individual parameters (Mandelbrot, 1960).

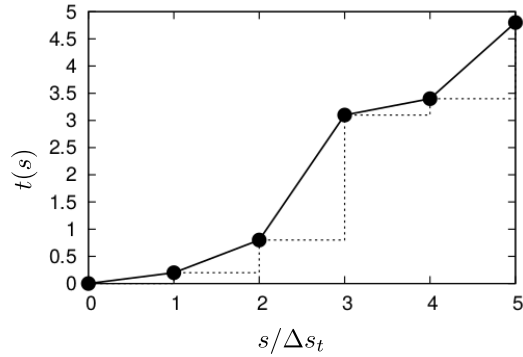


FIGURE 2.13: Schematic illustration of the time-mapping process according to Eq. 2.109. Taken from Kleinhans (2008).

on the increment Δs_t . Therefore, the parameter

$$C(\alpha, c, \Delta s_t) \equiv \Delta s_t \int_0^c p_\alpha(V) dV / \int_0^c V p_\alpha(V) dV, \quad (2.110)$$

which ensures that the mean slope of $t(s)$ is equal to one, is introduced (Kleinhans, 2008). This provides comparability between simulations with different values of α . For the numerical generation of random Lévy distributed numbers, the following procedure can be employed. Firstly, random numbers a_1 and a_2 that follow a uniform distribution on $(-\pi/2, \pi/2)$ and an exponential distribution with unit mean, respectively, are generated. This can easily be done via random numbers a_3 from the standard uniform distribution on $(0, 1)$ which is included in almost every programming environment:

$$a_1 = \pi \left(a_3 - \frac{1}{2} \right), \quad (2.111)$$

$$a_2 = -\log a_3. \quad (2.112)$$

Insertion of a_1 and a_2 into equation

$$\tau_\alpha \equiv \frac{\sin [\alpha (a_1 + \frac{\pi}{2})]}{\cos^{1/\alpha} a_1} \left(\frac{\cos [a_1 - \alpha (a_1 + \frac{\pi}{2})]}{a_2} \right)^{\frac{1-\alpha}{\alpha}} \quad (2.113)$$

yields Lévy distributed numbers. Random numbers $\tau_{\alpha,c}$ that follow the truncated distribution $p_{\alpha,c}$ can easily be generated by the rejection of random numbers, according to the above equation, that are larger than c .

In the scope of this work, the time-mapping process as described above is applied to simulated turbulence according to the wind model by Mann (1994, 1998) by considering the given time axis in the same way in which the model-intrinsic time s of the CTRW wind model is considered. The results are presented in Chapter 6.

Chapter 3

Large Eddy Simulation

As explained, the dynamics of fluid flows are governed by partial differential equations (PDEs)–the Navier-Stokes equations (Eqs. 2.8 and 2.14)–that represent the conservation of mass and momentum. Until today, the proof of the existence of global solutions for these equations has not yet been successful and is subject of one out of seven Millennium Prize Problems in mathematics that were stated by the Clay Mathematics Institute in 2000 (Jaffe, 2006). Closed analytical solutions exist only for few very simple cases and turbulent flows in particular are notoriously difficult to describe.

Fortunately, Computational Fluid Dynamics (CFD) provides a possibility to cope with this problem. CFD is the branch of Fluid Dynamics that deals with the substitution of the given PDEs by a set of algebraic equations that can be solved using digital computers to find approximative solutions. The transfer of the given continuous PDEs into algebraic equations takes place via discretization. In scope of this work, the discretization method chosen is the *Finite Volume method* (FVM), in which the domain is divided into a number of fixed volumes (cells) and the governing PDEs in their differential form are integrated over each of these control volumes. Volume integrals that contain divergence terms are–via Gauss’s theorem–converted to surface integrals that are evaluated as fluxes at the boundary of each cell. A flux that is leaving a given volume must always be identical to the flux that is entering the adjacent volume. Thus, the respective quantity is inherently conserved. The definition of the *grid* (or *mesh*), which is the set of cells created by edges joining pairs of vertices that are defined in the discretized spatial domain, plays a major role here.

The most forward and probably most correct approach to find a precise solution would be to solve the (discretized) Navier-Stokes equations directly (*direct numerical simulation*, DNS). The scales to be resolved, however, are determined by the physical properties of the flow and range from large-scale turbulent motions in the order of the characteristic length of the flow to the smallest scales that are determined by the Kolmogorov length l_η . As the required number of grid points in each spatial dimension as well as the required number of time steps scale with $\text{Re}^{3/4}$, the total computational costs scale with Re^3 (Sagaut, 2006). The approach of direct numerical simulation is therefore restricted to cases with moderate Reynolds numbers. Different alternative methods like the *Large Eddy Simulation* (LES) model, which is employed for the present work, can be used to lower the computational costs of the turbulent flow simulation. Here, the governing equations are solved for a *filtered* velocity field $\tilde{\mathbf{U}}(\mathbf{x}, t)$ representing the large-scale turbulent motions of the flow which are directly influenced by the boundary and hence are not universal. These equations include a model for the influence of the not directly represented scales of smaller size which are assumed to be universal. This method is justified by the fact that turbulent motion on large scales contain more energy than on smaller scales and

thus have a greater relevance for the transport of the conserved quantities (Ferziger, Peric, et al., 1999).

The scale separation is accomplished by application of a scale high-pass filter to the exact solution of the field $\phi(\mathbf{x}, t)$ (e.g., $\phi = U_i$ or $\phi = p$). The filtered field, denoted as $\tilde{\phi}(\mathbf{x}, t)$, is given by the convolution of ϕ with the filter kernel G (Sagaut, 2006):

$$\tilde{\phi}(\mathbf{x}, t) \equiv \int_{\mathbb{R}^3} \phi(\mathbf{x}', t) G(\mathbf{x} - \mathbf{x}') d^3x = (G * \phi)(\mathbf{x}, t). \quad (3.1)$$

The filter kernel G is associated with the effective cutoff scale $\Delta = (\Delta x \Delta y \Delta z)^{1/3}$, where Δx_i denotes the cell length in each direction, which determines the threshold value below which the flow is modeled. As Δ tends towards the Kolmogorov length l_η , the filtered Navier-Stokes equations are transformed into their non-filtered form and hence LES becomes DNS (McDonough, 2007). For the simulations considered in this work, the box or top-hat filter

$$G(\mathbf{x} - \mathbf{x}') = \begin{cases} \frac{1}{\Delta} & \text{if } |\mathbf{x} - \mathbf{x}'| \leq \frac{\Delta}{2}, \\ 0 & \text{otherwise} \end{cases} \quad (3.2)$$

is used.

The application of a filter to momentum and continuity equation leads to the following equations (Sagaut, 2006):

$$\frac{\partial \tilde{U}_i}{\partial t} + \frac{\partial}{\partial x_j} \widetilde{U_i U_j} = -\frac{1}{\rho} \frac{\partial \tilde{p}}{\partial x_i} + \nu \frac{\partial^2 \widetilde{U_i}}{\partial x_j \partial x_j} + \tilde{f}_i, \quad (3.3)$$

$$\frac{\partial \widetilde{U}_j}{\partial x_j} = 0. \quad (3.4)$$

The non-linear term $\widetilde{U_i U_j}$ can be expressed as a function of $\widetilde{\mathbf{U}}$ and the residual component \mathbf{U}' . The latter is defined via the decomposition

$$\mathbf{u} = \tilde{\mathbf{u}} + \mathbf{u}', \quad (3.5)$$

which should not be confused with the seemingly analogous Reynolds decomposition (Eq. 2.26). The difference between filtered product $\widetilde{U_i U_j}$ and the product of the filtered velocities $\widetilde{U_i} \widetilde{U_j}$ defines the *residual-stress tensor* following Leonard (1975):

$$\tau_{ij}^R \equiv \widetilde{U_i U_j} - \widetilde{U_i} \widetilde{U_j}. \quad (3.6)$$

τ_{ij}^R represents a measure for the influence of the small, unresolved scales on the resolved scales and is subject to different modeling approaches. The *subgrid scale model* for the residual-stress tensor used for LES in this work is described in Section 3.1. Consequently, the filtered Navier-Stokes equation can be rewritten as

$$\frac{\tilde{D} \widetilde{U}_i}{\tilde{D} t} = -\frac{1}{\rho} \frac{\partial \tilde{p}}{\partial x_i} + \nu \frac{\partial^2 \widetilde{U}_i}{\partial x_j \partial x_j} + \tilde{f}_i - \frac{\partial \tau_{ij}^R}{\partial x_j} \quad (3.7)$$

with a substantial derivative based on the filtered velocity in analogy to Eq. 2.3:

$$\frac{\tilde{D}}{\tilde{D} t} \equiv \frac{\partial}{\partial t} + \tilde{\mathbf{u}} \cdot \nabla. \quad (3.8)$$

3.1 Subgrid Scale Model WALE

Many subgrid-scale (SGS) models for LES are based on the introduction of an *eddy-viscosity* ν_t by which the deviatoric¹ part of τ_{ij}^R is modeled as

$$\tau_{ij}^R - \frac{1}{3} \tau_{kk}^R \delta_{ij} = -2 \nu_t \tilde{S}_{ij} \quad (3.9)$$

where δ_{ji} denotes the Kronecker delta and

$$\tilde{S}_{ij} \equiv \frac{1}{2} \left(\frac{\partial \tilde{U}_i}{\partial x_j} + \frac{\partial \tilde{U}_j}{\partial x_i} \right) \quad (3.10)$$

is the filtered rate-of-strain tensor (see Eq. 2.12). The first SGS model was created by Smagorinsky (1963) who considered the eddy viscosity as follows:

$$\nu_t = (C_S \Delta)^2 \sqrt{2 \tilde{S}_{ij} \tilde{S}_{ij}}. \quad (3.11)$$

C_S denotes the *Smagorinsky coefficient*. Theoretical considerations lead to a value of $C_S \approx 0.18$, whereby practice has shown that $C_S \approx 0.1$ yields more realistic results (Katopodes, 2018). Smagorinsky's model was also the SGS model for the very first LES to be performed and described (by Deardorff et al., 1970) and is still widely used to the present day. However, the Smagorinsky model has two major drawbacks. Firstly, Wray and Hunt (1990) were able to show via DNS that the energy in isotropic turbulence is concentrated not only in zones of high strain but also of high vorticity. For this reason, the above parameterization only with the filtered strain rate is not quite adequate. Secondly, the SGS model by Smagorinsky results in a non-zero turbulent viscosity near walls, even though it should be vanishing due to the damping of turbulent fluctuation there. In response, Nicoud and Ducros (1999) proposed the *Wall-Adapting Local Eddy-viscosity* (WALE) subgrid-scale model which is based on both strain and rotation rates and naturally leads to $\nu_t \rightarrow 0$ at walls:

$$\nu_t = (C_W \Delta)^2 \frac{\left(\tilde{S}_{ij}^d \tilde{S}_{ij}^d \right)^{3/2}}{\left(\tilde{S}_{ij} \tilde{S}_{ij} \right)^{5/2} + \left(\tilde{S}_{ij}^d \tilde{S}_{ij}^d \right)^{5/4}} \quad (3.12)$$

where

$$\tilde{S}_{ij}^d \equiv \frac{1}{2} \left(\tilde{g}_{ij}^2 + \tilde{g}_{ji}^2 \right) = \frac{1}{3} \delta_{ij} \tilde{g}_{kk}^2 \quad (3.13)$$

denotes the traceless symmetric part of the (filtered) squared velocity gradient tensor $\tilde{g}_{ij} = \partial \tilde{U}_i / \partial x_j$ and C_W is the model constant that is located in the interval $[0.55, 0.60]$ when assuming $C_S = 0.18$ (Nicoud and Ducros, 1999). The WALE model was used for all LES in this work.

¹This term is based on the nomenclature for the classical Cauchy stress tensor $\underline{\tau}$ which can be expressed as the sum of a hydrostatic tensor and a deviatoric tensor, defined as $\text{dev}(\underline{\tau}) \equiv \text{tr}(\underline{\tau}) \mathbb{1}/3$ where tr denotes the trace and $\mathbb{1}$ the unity matrix (Altenbach, 2012).

3.2 PIMPLE Algorithm

The PIMPLE algorithm that is used for solving the governing equations is based on the *Pressure-Implicit with Splitting of Operators* (PISO) algorithm, which was developed by Issa (1986) for unsteady flows, and the *Semi-Implicit Method for Pressure Linked Equations* (SIMPLE) algorithm for steady-state flows by Patankar and Spalding (1972). Detailed presentation of the method shall be omitted here. Instead, respective literature (e.g., Holzmann, 2016) should be consulted.

The PISO algorithm essentially consists of the following steps:

1. Definition of boundary conditions,
2. solution of the momentum equation (*momentum predictor*),
3. calculation of the mass fluxes at cell faces,
4. solution of the pressure equation (see Eq. 2.15)
5. correction of mass fluxes at cell faces
6. correction of the velocity based on pressure with step 4,
7. update of boundary conditions,
8. repetition from step 3 for prescribed number of times,
9. increase of the time step and repetition from step 1.

The SIMPLE algorithm can be summarized as follows:

1. Definition of boundary conditions,
2. solution of the momentum equation,
3. calculation of the mass fluxes at cell faces,
4. solution of the pressure equation,
5. correction of the mass fluxes,
6. correction of the velocity with new pressure
7. repetition until convergence is reached.

Both methods can now be combined to the PIMPLE algorithm in order to achieve a higher stability. This can be thought of as the SIMPLE algorithm with a subsequent PISO loop which is repeated for a prescribed number of items (*inner correctors*). The *outer correctors* define, how many times the total system (SIMPLE loop and repeated PISO loop) is run until the next time step is considered. For LES in the scope of this work, the number of inner correctors was set to 2 and the number of outer correctors was set to 1. All simulations were performed with OpenFOAM® (Weller and Jasak, 2019). The corresponding input files that define the configuration of the simulations are given in Appendix C.

3.3 Turbulent Inflow Method

In scope of this work, a method for imposing the synthetic turbulent velocity field $\mathbf{u}(\mathbf{x})$ is investigated. It exploits the volume force in the momentum equation (Eq. 2.14) to accelerate or decelerate the flow to the desired magnitude, respectively. A prerequisite for this approaches is the conversion of the stationary field $\mathbf{u}(\mathbf{x})$ into a time-dependent field $\mathbf{u}'(y, z, t)$ in the spirit of Taylor's hypothesis (see Eq. 2.27):

$$u'_i(y, z, t) = u_i(x = (T - t) \langle U \rangle, y, z), \quad (3.14)$$

which is applicable if $\langle u'^2 \rangle \ll \langle U \rangle^2$, i. e., if the turbulence intensity is sufficiently small ($TI_i \ll 1$). A mean velocity $\langle U \rangle$ is provided by corresponding boundary conditions.

A more straight-forward approach would be the injection of the field with a boundary condition approach. Here, the time-dependent Neumann condition

$$U_i(x = 0, y, z, t) = \langle U \rangle \delta_{1i} + u'_i(t, y, z) \quad (3.15)$$

for the inlet patch at $x = 0$ would be used. The disadvantage of this very intuitive approach is that the region of interest often demands a large distance to the boundaries of the computational domain to minimize their influence. Furthermore, the grid resolution in the region of interest is often chosen to be significantly larger compared to the boundary regions.

The alternative approach of turbulence imposition via volume forces, however, allows a positioning closer to the region of interest. The following formulation can, for instance, be found in the works of Gilling and Sørensen (2011) and Troldborg et al. (2014). To begin with, the pressure jump Δp that is required to accelerate the flow from $\langle U \rangle$ to $\langle U \rangle + u'$ along a streamline can be directly derived from Bernoulli's equation (Eq. 2.16):

$$\Delta p = \frac{1}{2} \rho \left[(\langle U \rangle + u')^2 - \langle U \rangle^2 \right]. \quad (3.16)$$

This pressure jump corresponds to the following volume force along a path of length Δn , which is depicted in Fig. 3.1:

$$f = \frac{\rho u'}{\Delta n} \left(\langle U \rangle + \frac{1}{2} u' \right). \quad (3.17)$$

This equation can be extended to three dimensions with a heuristic approach (Gilling and Sørensen, 2011):

$$f = \frac{\rho u'}{\Delta n} \left(\langle U \rangle + \frac{1}{2} u'_\perp \right) \quad (3.18)$$

Here, $u'_\perp = \mathbf{u}' \cdot \hat{\mathbf{x}}$ denotes the projection of the velocity fluctuations onto the mean flow direction. The acceleration distance Δn for all LES carried out in the scope of this work is chosen as $\Delta n = 2$ m.

The basic concept behind the presented inflow method is schematically illustrated in Fig. 3.2.

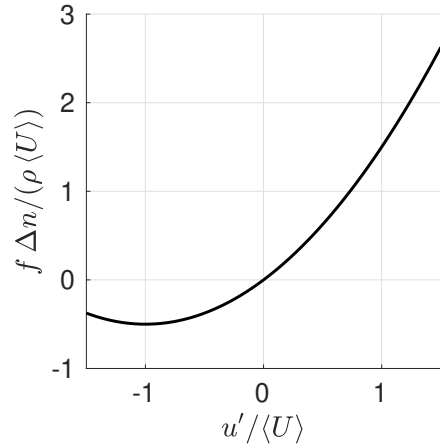


FIGURE 3.1: Course of the one-dimensional volume force required for the acceleration by u' (Eq. 3.17).

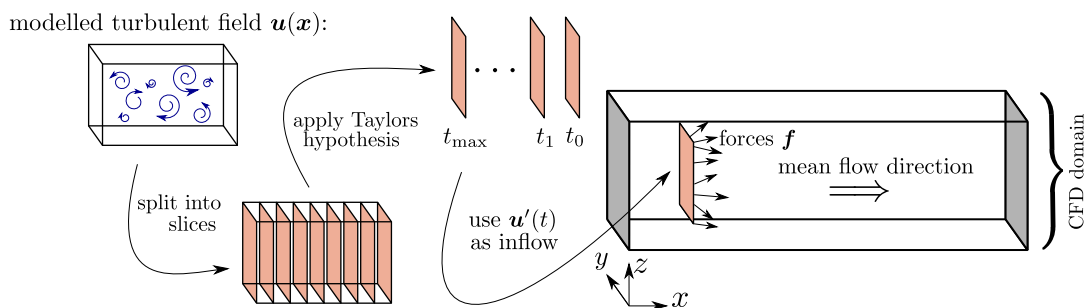


FIGURE 3.2: Schematic illustration of the approach presented: The modeled stationary turbulent velocity field $u(x)$ is split into slices in the (y, z) -plane along the x -direction. Subsequently, every slice is identified with a respective time step according to Taylor's hypothesis (Eq. 3.14). Finally, the turbulent field can be introduced to the LES for every time step via volume forces as described by Eq. 3.18.

Chapter 4

Analysis of Fourier Simulated Mann Turbulence

In order to investigate the turbulent velocity field provided by the Fourier simulation as described in Section 2.3.1, an exemplary non-isotropic case is considered. Furthermore, the statistical properties of the simulated field are compared to those that arise from the purely analytical model by Mann (1994) which is, in contrast, based on the assumption of continuous space and an infinitely large domain \mathcal{B} . The chosen physical parameters are derived from the Engineering Science Data Unit (ESDU) spectral model (ESDU, 1982) for $\langle U \rangle = 40 \text{ m s}^{-1}$ over sea. The values for Γ , L and $c_K \varepsilon^{2/3}$ as well as for n_i and δx_i (spatial increment), which determine the size and the spatial resolution of the domain, are given in Tab. 4.1.

TABLE 4.1: Parameter values of the Mann model derived from the ESDU spectral model (ESDU, 1982) and chosen values for the number of points n_i in each direction and the spatial increments δx_i .

Γ	L	$c_K \varepsilon^{2/3}$	n_x	$n_y = n_z$	δx_i
4.5	66 m	$0.62 \text{ m}^{4/3} \text{ s}^{-2}$	1024	128	8 m

Fig. 4.1 shows the magnitude $|u(x)|$ of the stationary simulated field with the parameters obtained from the ESDU fit in a vertical and a horizontal plane in the center of the domain. As can be seen in the (x, z) plane in the upper plot, the influence of the shear, i. e., the vertical gradient $d\langle U \rangle / dz$, on the velocity fluctuations cause a distortion of its spatial structures. The anisotropy is thus directly evident in the flow field. However, this feature is apparent neither in the (x, y) plane nor in the (y, z) plane which is depicted in Fig. 4.2 at $x = L_x/2$, since the shear does not have any effect on these planes. Moreover, Fig. 4.3 depicts the course of all three velocity fluctuation components along the x direction exemplarily at $(y, z) = (0, 0)$. Although the plot corresponds to only one point in the (y, z) plane, it can be regarded as representative for the whole field due to the homogeneity which is a universal feature of the wind model by Mann. Here, the effect of the shear becomes apparent by the dominance of considerable fluctuations of the velocity component u_x in comparison to u_y which shows, in turn, larger structures than u_z . The associated difference of the respective variances is a direct result of the anisotropy ($\Gamma > 0$) as illustrated in Fig. 2.8. In Section 4.1, the one-point spectra of analytical and Fourier simulated Mann turbulence as well as their relevance for the variances of the velocity are addressed. Moreover, Section 4.2 is devoted to the comparison of analytical and Fourier simulated Mann turbulence with respect to the coherence. Section 4.3 deals with the divergence of the Fourier simulated velocity field and the application of a methodology for minimizing it. In Section 4.4, the distribution of velocity increments of Fourier simulated Mann turbulence is analyzed.

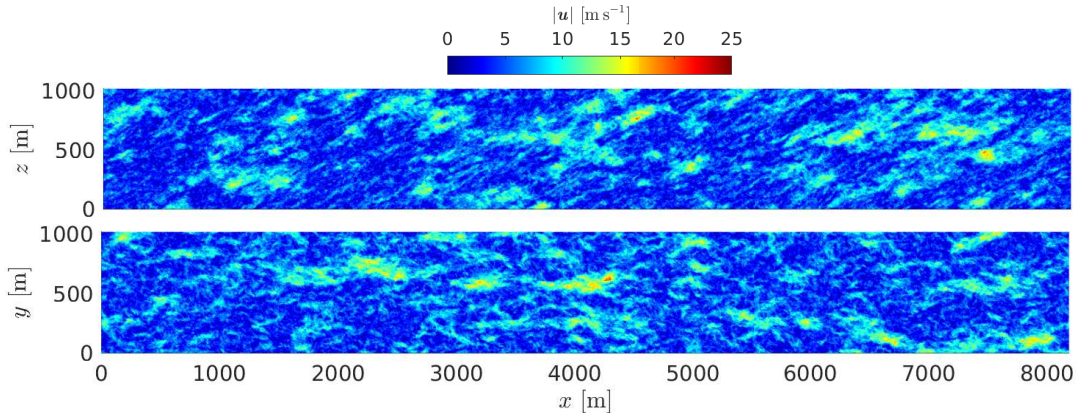


FIGURE 4.1: Absolute value of the velocity fluctuations at $y = L_y/2$ (figure on the top) and at $z = L_z/2$ (figure on the bottom) for parameter set as given in Tab. 4.1.

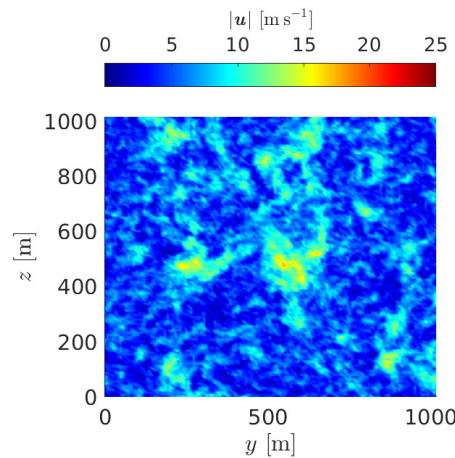


FIGURE 4.2: Absolute value of the velocity fluctuations at $x = L_x/2$ for parameter set as given in Tab. 4.1.

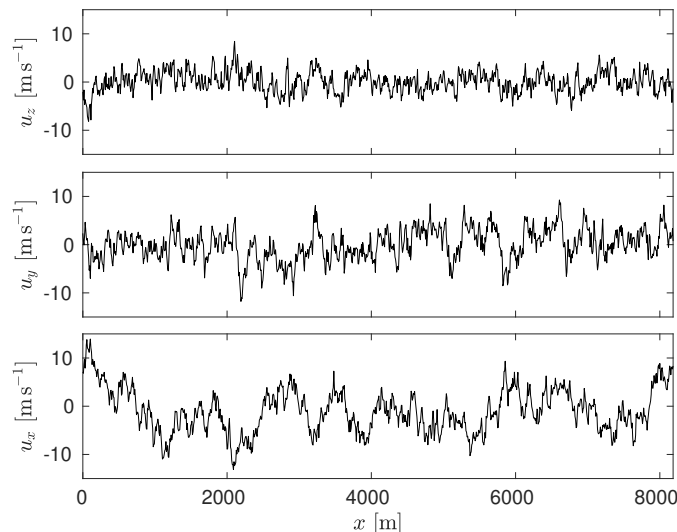


FIGURE 4.3: Turbulent velocity fluctuation components as function of x at $(y, z) = (0, 0)$ obtained from the ESDU fit parameters as set out in Tab. 4.1.

4.1 One-Point Spectra and Variances

The power spectral densities $F_i(\kappa_x)$ (Eq. 2.37) of all three velocity components of the simulated turbulence can be calculated efficiently with the Fast Fourier Transform (FFT) algorithm (Van Loan, 1992). Fig. 4.4 shows $\langle F_i(\kappa_x) \rangle_{\mathcal{I}}$, where $\langle \cdot \rangle_{\mathcal{I}}$ denotes spatial averaging over the plane $\mathcal{I} = \{(y, z) \mid 0 \leq y \leq L_y, 0 \leq z \leq L_z\}$ perpendicular to the main direction of propagation, in comparison with the respective analytical expressions that arise from Eq. 2.37 with the spectral tensor given by Eqs. 2.93 – 2.98. The implementation of the underlying equations is based on the work of Cheynet (2020). Evidently the spectra are in good accordance with the expected courses.

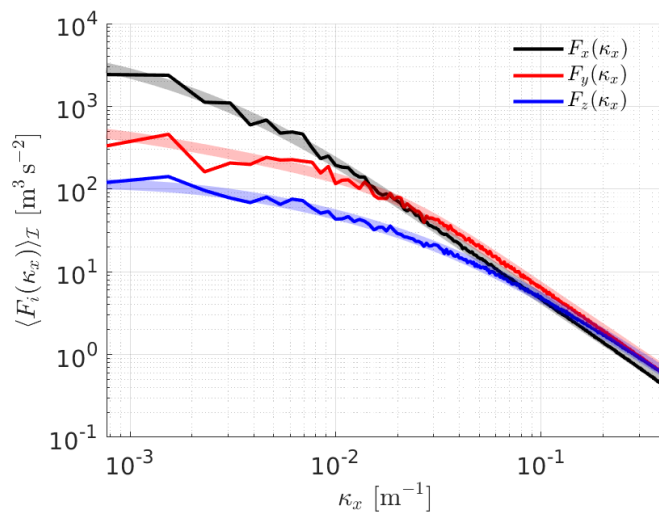


FIGURE 4.4: Power spectral densities of all turbulent velocity components, averaged over the (y, z) plane, for the parameters listed in Tab. 4.1. The smooth, transparent lines represent the analytical expressions for $F_i(\kappa_x)$.

As mentioned earlier, the turbulence intensity and thus the variance (see Eq. 2.28) as a simple statistical property is often conventionally considered in the field of aerodynamics. For various engineering applications, it is therefore essential to set the variance of the velocity field to a prescribed value before using it for numerical simulations. However, the relation between the set of parameters $\{L, \Gamma, c_K \varepsilon^{2/3}\}$ that determine the turbulent velocity field and the variance is not straightforward. According to Eq. 2.32 and Eq. 2.37, the variance is given by¹ (no summation)

$$\sigma_i^2 = \int_{\mathbb{R}} F_i(\kappa_x) d\kappa_x = 2 \int_0^\infty F_i(\kappa_x) d\kappa_x. \quad (4.1)$$

On this basis, Mann (1994) provides an explicit expression for the variance as function of L and $c_K \varepsilon^{2/3}$ (Eq. 2.79). However, this only holds for the simple case of isotropy (i. e., $\Gamma = 0$) and $\mathcal{B} = \mathbb{R}^3$, i. e., and infinitely large and continuous spatial domain. Whilst the first restriction can of course also be fulfilled for the Fourier simulated turbulent field, the latter is generally not given since numerical data is always finite and discrete.

For the utilization of Mann turbulence in the aeroelastic HAWC2 tool (Larsen and Hansen, 2007), the authors propose an arbitrary choice of $c_K \varepsilon^{2/3}$ and a subsequent

¹The spectra are two-folded, but symmetric. For this reason, only the positive wave numbers are considered here.

rescaling of the field $\mathbf{u}(x)$ with the scaling factor

$$\text{SF} = \sqrt{\frac{\sigma_{\text{target}}^2}{\sigma^2}} \quad (4.2)$$

where σ^2 denotes the variance of the original field and $\sigma_{\text{target}}^2 = \text{TI}^2 \langle U \rangle^2$ (see Eq. 2.28) denotes the target variance that should be reached in order to obtain to desired turbulence intensity TI. When using this method it should be noted that the physical parameter $c_K \varepsilon^{2/3}$ is as well implicitly rescaled, namely by the squared scaling factor since $\mathbf{u}(x) \propto \sqrt{E(\kappa)} \propto \sqrt{c_K \varepsilon^{2/3}}$ which can be verified with Eqs. 2.93 – 2.98 together with Eq. 2.69.

Alternatively, the value for the parameter $c_K \varepsilon^{2/3}$ can be chosen in advance, if a functional relation between variance and the parameter for the Fourier simulation is known. In order to obtain such a relation, the finiteness and the discretization of the domain \mathcal{B} has to be taken into account. First of all, if a finite but continuous domain $\mathcal{B} = [0, L_x] \times [0, L_y] \times [0, L_z]$ is considered, the lowest wavenumber κ_x is given by $\kappa_x^{\min} = 2\pi/L_x$. As a result, the variances are, based on Eq. 4.1, given as (no summation)

$$\sigma_i^2 = 2 \int_{\kappa_x^{\min}}^{\infty} F_i(\kappa_x) d\kappa_x. \quad (4.3)$$

As seen in Fig. 4.5 A which shows the variances of the velocity components as function of the length L_x of the domain in longitudinal direction, this gives a decent approximation for the actual variances of the simulated field. Still, the variances of u_y and u_z are clearly overestimated for the larger spatial increment $\delta x = 20$ m. The fact that all variances are significantly lower than according to Eq. 4.1 (horizontal lines in Fig. 4.5 A) up to $L_x/L \sim \mathcal{O}(10^4)$ underlines the invalidity of Eq. 4.1 for Fourier simulated Mann turbulence.

At this point, it is suitable to take into account the upper limit of the wavenumber range, too. For sampled, i. e., discrete data, the Nyquist frequency, given by half the sampling rate, is the highest frequency that the signal can unambiguously represent (Van Loan, 1992). Considering the field $\mathbf{u}(x)$ in the spatial domain, the term Nyquist wavenumber may be more appropriate in this context. Thus, the integral (no summation)

$$\sigma_i^2 = 2 \int_{\kappa_x^{\min}}^{\kappa_x^{\max}} F_i(\kappa_x) d\kappa_x. \quad (4.4)$$

with $\kappa_x^{\max} = \pi/\delta x$ given by the Nyquist wavenumber can be taken as a measure for the variance for the simulated turbulent field which is both finite and discrete. Figs. 4.5 B and C show the variances for the velocity components, again as function of L_x/L , in comparison to the variances that arise from Eq. 4.4. It is found that additional consideration of the maximum wavenumber κ_x^{\max} gives an even greater concordance with the data (see Fig. 4.5 A for comparison).

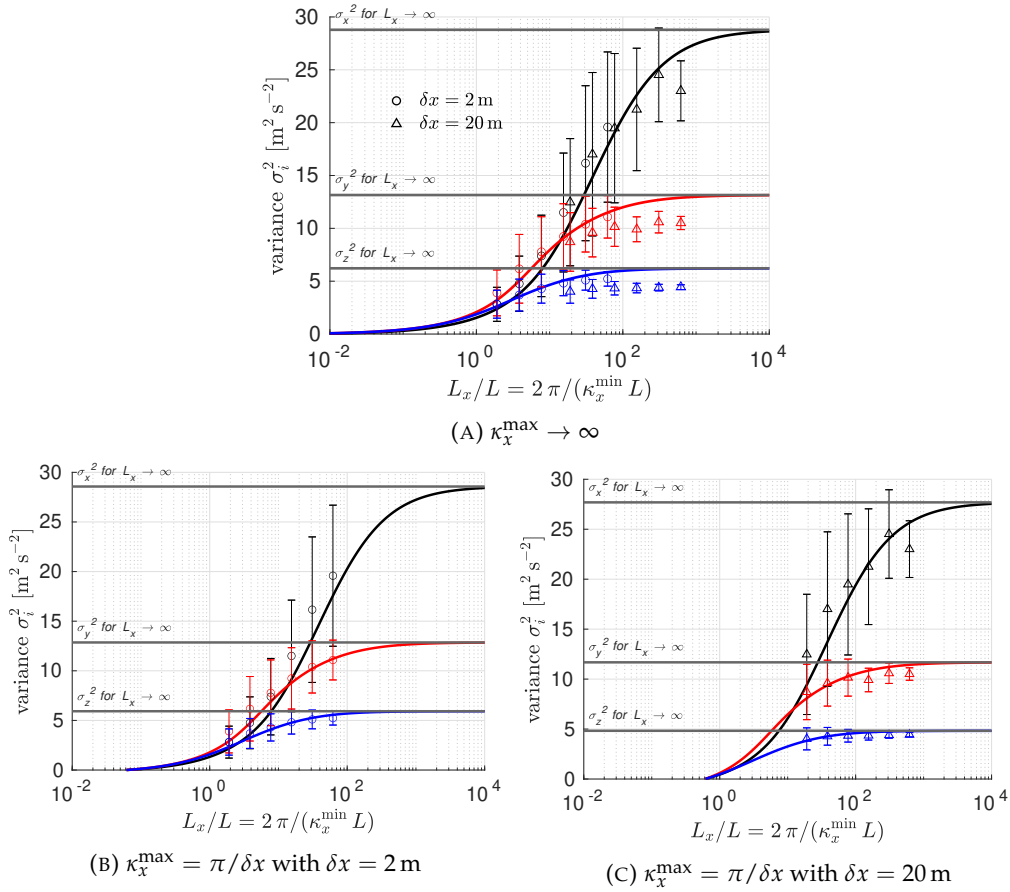


FIGURE 4.5: Obtained variances as function of L_x/L (length of the turbulence box in units of the length scale parameter L) in comparison to Eq. 4.3 for the set of parameters given in Tab. 4.1 for the spatial increments $\delta x = 2\text{ m}$ and $\delta x = 20\text{ m}$ as well as in comparison to Eq. 4.4 for $\delta x = 2\text{ m}$ and $\delta x = 20\text{ m}$ separately (B and C). Black, red and blue lines indicate the x , y and z component, respectively. Error bars correspond to the spatial standard deviation within the (y, z) plane in each direction. The horizontal lines represent the variances for an infinite domain.

4.2 Coherence

The coherence (Eq. 2.36) of two velocities $u_i(x, y, z)$ and $u_j(x, y + \Delta y, z + \Delta z)$, that are spatially separated by the length $\sqrt{\Delta y^2 + \Delta z^2}$ in the direction transversal to the mean flow, is defined as their magnitude-squared cross-spectrum (Eq. 2.35) divided by the product of their respective one-point spectra. In the practice of signal processing, these quantities can be estimated by averaging over realizations of the process or successive signal blocks (Kramer, 2013):

$$\text{coh}(\kappa_x, \Delta y, \Delta z) = \frac{|\langle \chi_{ij}(\kappa_x, \Delta y, \Delta z) \rangle|^2}{\langle F_i(\kappa_x) \rangle \langle F_j(\kappa_x) \rangle} \quad (4.5)$$

Since the turbulent field $u(x)$ is homogeneous (Mann, 1994), the averaging process can be applied with respect to the (y, z) plane (denoted as \mathcal{I}). Moreover, when expressing cross-spectrum and one-point spectra by the Fourier transform \mathcal{F} , it follows

that

$$\text{coh}_{ij}(\kappa_x, \Delta y, \Delta z) = \frac{|\langle \mathcal{F}^* \{u_i(x, y, z)\}(\kappa_x) \mathcal{F} \{u_j(x, y + \Delta y, z + \Delta z)\}(\kappa_x) \rangle_{\mathcal{I}}|^2}{\langle |\mathcal{F} \{u_i(x, y, z)\}(\kappa_x)|^2 \rangle_{\mathcal{I}} \langle |\mathcal{F} \{u_j(x, y + \Delta y, z + \Delta z)\}(\kappa_x)|^2 \rangle_{\mathcal{I}}}. \quad (4.6)$$

Given this formulation, the coherence of the simulated velocity field can, just like the one-point spectra, be efficiently calculated via FFT.

To verify the cross-spectral properties of the Fourier simulated field $\mathbf{u}(x)$, the coherence of the velocities with horizontal ($\Delta y > 0, \Delta z = 0$), vertical ($\Delta y = 0, \Delta z > 0$) and diagonal ($\Delta y > 0, \Delta z > 0$) separation is computed and compared to the respective analytical expressions that arise from Eq. 2.36 with Eqs. 2.35 and 2.37 for the spectral tensor Φ_{ij} that constitutes the turbulence model (Eqs. 2.93 – 2.98) given the parameters in Tab. 4.1 (Fig. 4.6). A very high consistency between analytical expression and the coherence of the simulated data is noted.

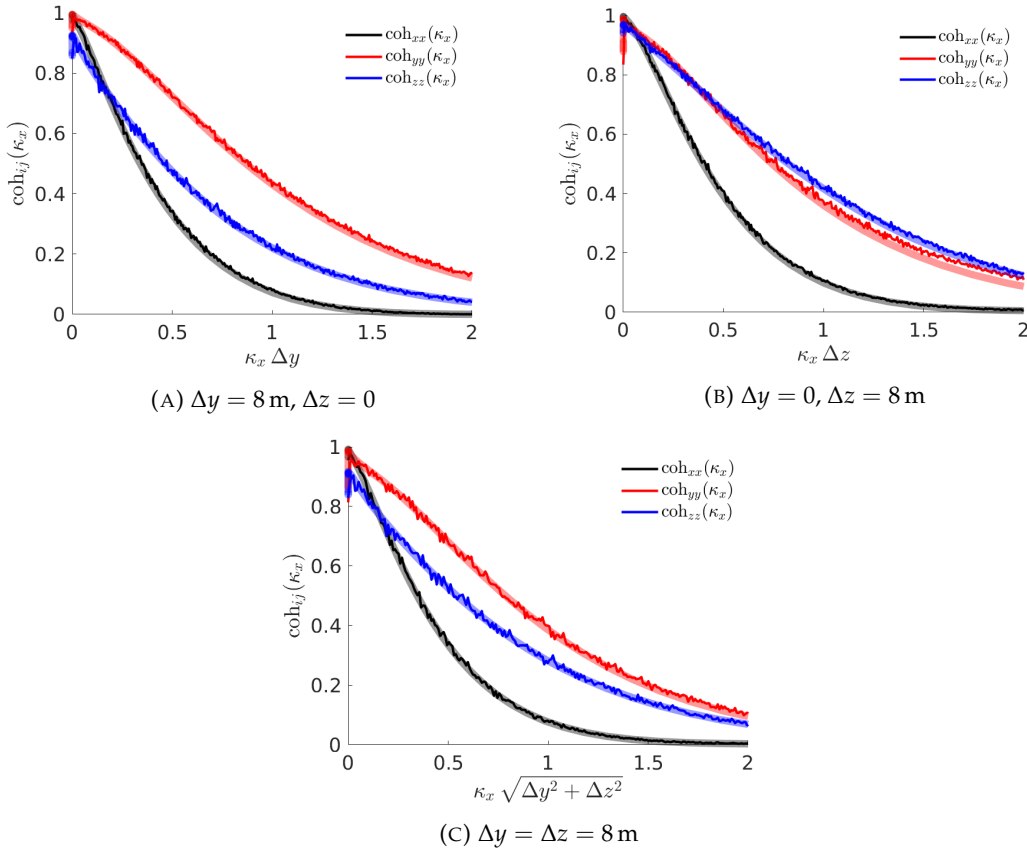


FIGURE 4.6: Coherence of all turbulent velocity components with the parameters listed in Tab. 4.1; horizontal spatial separation (A), vertical spatial separation (B) and diagonal spatial separation (C). The smooth, transparent lines represent the respective analytical expressions.

4.3 Divergence

The divergence of the modeled turbulent field, especially when using it as inflow for numerical simulations for incompressible flows, is of great importance. CFD solvers for incompressible flows enforce the satisfaction of the continuity equation as given by Eq. 2.8. This means that a large deviation from $\nabla \cdot \mathbf{u} = 0$ is then accompanied by substantial changes of the spatial structure of \mathbf{u} by the numerical solution algorithm. The standard deviation of the considered exemplary simulated field $\mathbf{u}(x)$ is normally distributed around zero within the domain \mathcal{B} , as can be seen in Fig. 4.7.² The standard deviation of the divergence with respect to the whole domain \mathcal{B} for the considered simulation is given as $\sqrt{\langle (\nabla \cdot \mathbf{u})^2 \rangle_{\mathcal{B}}} = 0.109 \text{ s}^{-1}$. Shirani et al. (1981)

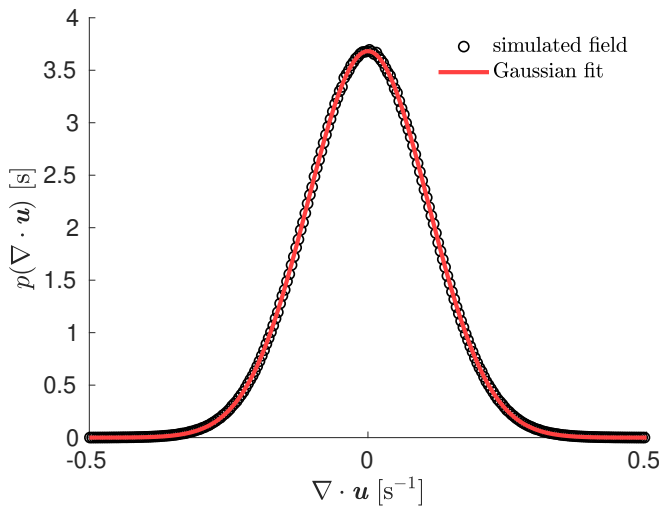


FIGURE 4.7: PDF of the divergence within the domain \mathcal{B} with respective Gaussian least-squares fit.

propose a method to make a given velocity field $\mathbf{u}(x)$ divergence-free. In theory, this constitutes an opportunity to obtain the satisfaction of the continuity equation before exposing the field to CFD simulations. The method can be summarized as follows: Let $u_i^I(x_j)$ be the original, unmodified velocity field. The sum of this field and the gradient of a potential $\varphi(x_i)$ is defined as $u_i^{II}(x_j)$ such that its divergence vanishes:

$$u_i^{II}(x_j) \equiv u_i^I + \frac{\partial \varphi(x_j)}{\partial x_i}. \quad (4.7)$$

For $\nabla \cdot \mathbf{u}^{II}(x)$ to be fulfilled, the following Poisson equation must apply:

$$\frac{\partial^2 \varphi(x_j)}{\partial x_i \partial x_i} = -\frac{\partial u_i^I(x_j)}{\partial x_i}. \quad (4.8)$$

Fourier transformation of this equation provides an expression for the Fourier transform of the potential $\varphi(x_i)$:

$$\mathcal{F}\{\varphi(x_j)\}(\kappa_j) = \frac{\kappa_i}{i \kappa^2} \mathcal{F}\{u_i(x_j)\}(\kappa_j). \quad (4.9)$$

²The partial derivatives for the divergence were computed using central differences for the interior points of \mathcal{B} and single-sided (forward and backward) differences for points along the edges of \mathcal{B} .

Hence from the calculation of $\mathcal{F}\{\varphi(x_j)\}(\kappa_j)$ with the above equation, a subsequent reverse transformation into the spatial domain and substitution into Eq. 4.7 gives the desired selenoidal (divergence-free) field $u^{\text{II}}(x)$.

When applying this method to the given discrete data, the Fourier transform can efficiently be calculated by performing three-dimensional FFT. For the given field that results from the parameters given in Tab. 4.1, the procedure minimizes the divergence within the field so that the standard deviation of $\nabla \cdot u$ is corrected to $\sqrt{\langle (\nabla \cdot u)^2 \rangle_B} = 0.101 \text{ s}^{-1}$ and thus reduced by approximately 7 %. A reduction to zero can not be expected since the above equations are only exact for continuous smooth functions. Repeat application of the divergence correction method does not lead to a further reduction of $\nabla \cdot u$ as can be seen in Fig. 4.8 which shows the standard deviation of the divergence as function of the number of iterations. Fig. 4.9

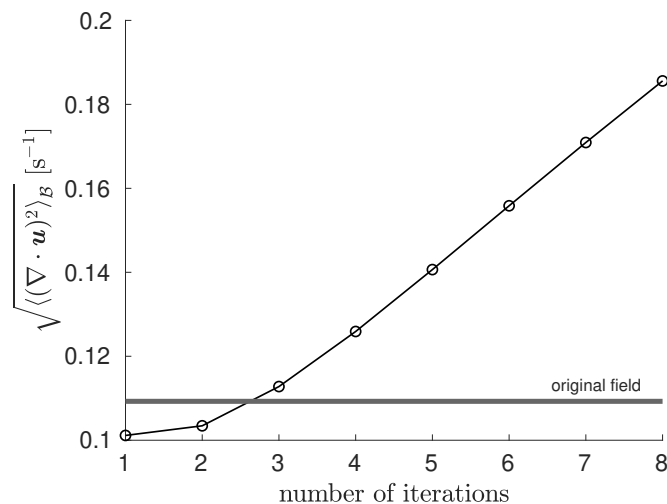


FIGURE 4.8: Standard deviation of the divergence within the domain \mathcal{B} as function of the number of iterations considered. The horizontal line represents the divergence standard deviation before application of the correction method by Shirani et al. (1981).

shows the one-point spectra of the original field in comparison to the spectra of the corrected field after one iteration. The spectra are only slightly affected by the divergence correction. Significant differences can only be identified at large wavenumbers (see magnified plot in Fig. 4.9). This indicates that the divergence correction changes the spatial structure of the field $u(x)$ only at small scales while large scales remain practically unaffected.

Due to the only slight decrease of the divergence, the presented correction method is not used hereinafter. However, it might provide a valuable tool for velocity fields with a higher initial divergence than the one considered here.

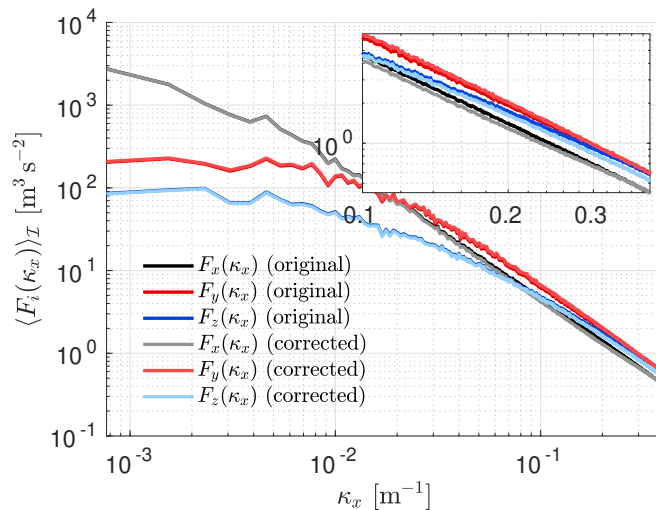


FIGURE 4.9: Power spectral densities for all velocity components for original and divergence corrected field according to Shirani et al. (1981).

4.4 Increment Statistics

As the Mann wind model only comprises the second-order structure of atmospheric turbulence, it lacks the property of intermittency, presenting itself for instance in the form of leptokurtic probability distributions for the velocity increments (see Eqs. 2.39 and 2.40), e. g.,

$$u_r = u_x(x + r, y, z) - u_x(x, y, z), \quad (4.10)$$

which is can be considered as independent of the reference point (x, y, z) since spatial homogeneity is one of the fundamental assumptions of Mann's model.

Considering the exemplary field resulting from the parameters given in Tab. 4.1, the increment probability density functions depicted in Fig. 4.10 arise. For comparison, the PDFs are shown together with Gaussian distributions with the same respective standard deviation. As the figure implies, the PDFs of u_r are in close correspondence with Gaussian distributions and the turbulence is therefore not intermittent. In the following Chapter 5, however, it is investigated to what extend intermittency occurs in LES if Mann modeled turbulence is used as inflow. Furthermore, in Chapter 6 it is described how the stochastic time-mapping process of the CTRW wind model by Kleinhans (2008) can be used as an ex-post approach to make the turbulence intermittent.

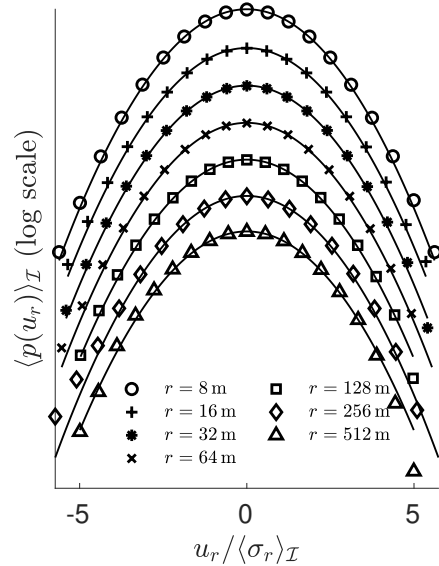


FIGURE 4.10: Spatially averaged PDFs of u_r for different spatial separations r . Velocity increments are normalized by their spatially averaged standard deviation. The solid lines represent Gaussian distribution with the same respective standard deviation for comparison. All PDFs are vertically shifted for the sake of clarity.

Chapter 5

Large Eddy Simulation with Mann Turbulence Inflow

This chapter addresses the utilization of Fourier simulated Mann turbulence as an inflow for Large Eddy Simulations through the volume force approach as described in Section 3.3. Firstly, the numerical setup of the simulations as well as the choice of the parameters for the Mann turbulence model (Section 5.1) is considered. Moreover, the inflow methodology is verified in Section 5.2 and the influence of the spatial resolution of the LES domain is investigated in Section 5.3. The changes of the one-point spectra, the turbulence intensity in longitudinal direction, the coherence and the increment statistics in the LES are dealt with in Sections 5.4 – 5.7.

The statistical properties of the flow velocity in LES are considered in the time domain at different distances to the location of the plane where the synthetic turbulent field is introduced (x_{in}). The total simulation time was chosen so that the complete Mann box would reach the end of the LES domain, given the mean velocity of $\langle U \rangle = 10 \text{ m s}^{-1}$. It may be noted that the time intervals, over which an average $\langle \cdot \rangle$ (see Eq. 2.23) is determined, are considered as function of the distance $x - x_{\text{in}}$ to the inlet plane in accordance to Taylor's hypothesis. This means that the averaging starts from $t_0 = (x - x_{\text{in}})/\langle U \rangle$, i. e., the time it takes for the turbulence, which is carried by the mean flow with velocity $\langle U \rangle$, to reach x . Accordingly, the averaging ends at $t_0 + T$ where $T = L_x/\langle U \rangle$ is the total time of the inflow field after conversion into the time domain (Eq. 3.14). The consideration of the correct time interval for averaging is crucial, as the statistical properties are highly dependent on it. For the variance, for instance, this is clear from Fig. 4.5.¹

In the preceding chapter, the subscript \mathcal{I} was chosen to denote spatial averaging over the whole (y, z) -plane of the Mann box. In analogy, $\langle \cdot \rangle_{\mathcal{I}}$ in this chapter symbolizes the spatial average over the part of the LES domain that contains the turbulent inflow field (bordered by red lines in Fig. 4.1), in y - and z -direction.

5.1 Numerical Setup

All flow simulations are performed with OpenFOAM®. The corresponding files that define the simulation setup are given in Appendix C.

To provide a mean velocity field for the carriage of the modelled turbulent field, the boundary condition at $x = 0$ is set to the desired value

$$\mathbf{U}(x = 0, y, z, t) = \langle U \rangle \hat{\mathbf{x}}, \quad \text{with } \langle U \rangle = 10 \text{ m s}^{-1} \quad (5.1)$$

¹In this figure, the variance is considered as function of L_x . This, however, is equivalent to the length of the considered time interval, since $L_x = \langle U \rangle T$ according to Taylor's hypothesis.

where \hat{x} denotes the unit vector in x direction. For the opposite boundary of the domain, i. e., the outlet patch, the following Neumann boundary condition is applied:

$$\frac{\partial \mathbf{U}}{\partial x} \Big|_{x=x_{\max}} = 0. \quad (5.2)$$

This zero-gradient condition extrapolates the velocity to the boundary from the nearest cell value. For the *kinematic pressure* $p_k \equiv p/\rho$ the reverse is applied, meaning that p_k is subject to the zero-gradient condition at $x = 0$ and set to zero at $x = x_{\max}$. The eddy-viscosity ν_t is subject to the zero-gradient condition both at $x = 0$ and $x = x_{\max}$. The remaining boundaries transversal to the mean flow direction are chosen as cyclic for all quantities. Hence, the opposing boundaries are treated as if they were physically connected in order to minimize the influence of the boundary regions on the region of interest—the turbulent flow field in the center of the domain.

The initial condition for the velocity is expediently chosen as

$$\mathbf{U}(x, t = 0) = \langle U \rangle \hat{x}. \quad (5.3)$$

The values for p_k and ν_t are set to zero for $t = 0$. In order to suppress the occurrence of periodic artifacts due to the unphysical topology of the simulation domain, the inlet plane where the turbulent field $\mathbf{u}'(y, z, t)$ is introduced via forces (see Fig. 3.2), is not directly connected to the boundaries of the computational domain. The lateral distance to the periodic boundaries is given as one fourth of the domain's length in each direction. Moreover, the inlet plane is placed at $x = x_{\max}/4$ in streamwise direction. The spatial dimensions are chosen as $x_{\max} = 320$ m, $y_{\max} = z_{\max} = 160$ m. In order to reduce computational costs, the spatial resolution is chosen as constant (given as $\Delta x_i = 1$ m) and also highest in the region of interest where the turbulence is introduced and gradually decreased towards the domain boundaries, so that the spatial resolution in the domain center is four times higher than at the boundaries. Cross-sections of the mesh are shown in Fig. 5.1 for a lower number of grid cells than used in scope of this work for the sake of visibility. With $\Delta x_i = 1$ m in the center of the domain, the total number of cells is given as $n_x = 320$ in x direction and $n_y = n_z = 120$ in both y and z direction.

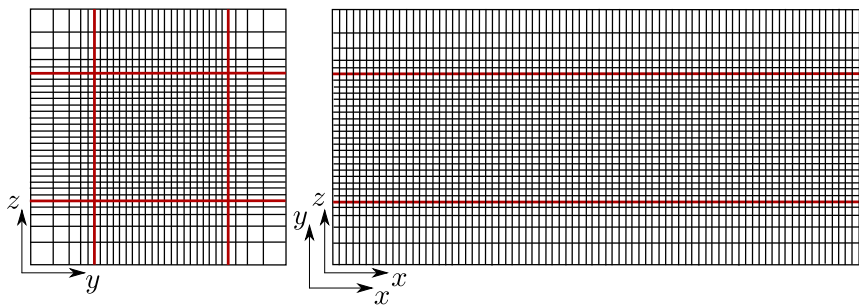


FIGURE 5.1: Computational domain, exemplary with $(n_x, n_y, n_z) = (80, 30, 30)$: (y, z) -plane (left) and (x, y) -plane / (x, z) -plane view (right). Spatial resolution is constant ($\Delta x_i = \text{const}$) in the subset $[x_{\max}/4, 3x_{\max}/4] \times [y_{\max}/4, 3y_{\max}/4] \times [z_{\max}/4, 3z_{\max}/4]$ (bordered by red lines) within which the turbulent flow is introduced and gradually decreasing towards the boundaries of the domain.

Fig. 5.2 depicts the magnitude of the velocity field \mathbf{U} for an isotropic Mann box inflow that is scaled to an average longitudinal standard deviation of $\langle \text{TI}_x \rangle_{\mathcal{I}} = 5\%$ with $\langle U \rangle = 10 \text{ m s}^{-1}$ at an exemplary time $t = 200 \text{ m}$. Statistical analysis of this and further velocity fields is the subject of the following sections.

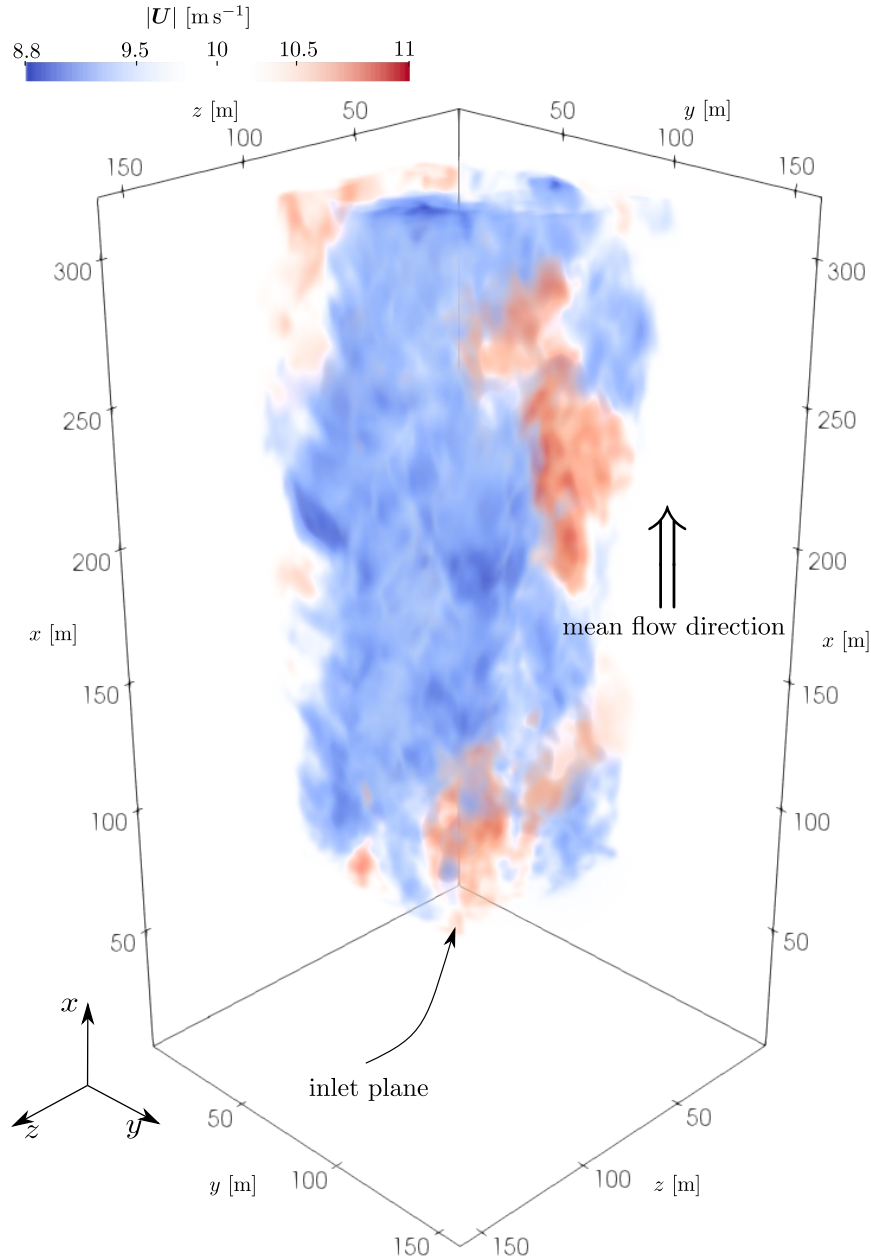


FIGURE 5.2: Velocity magnitude $|U|$ at exemplary time $t = 200 \text{ s}$ in LES with isotropic Mann box inflow ($\Gamma = 0$) that was rescaled to an average longitudinal standard deviation of $\langle \text{TI}_x \rangle_{\mathcal{I}} = 5\% \langle U \rangle$.

Choice of Parameters

For the analysis of Mann modeled turbulence as inflow for Large Eddy Simulations, fixed longitudinal turbulence intensities TI_x (Eq. 2.28) are considered in order to permit comparability between cases with different values for Γ . Hence, the effect of anisotropy due to shear can rather be observed in isolation.

For the length scale L , Kelly (2018) proposes the following parameterization:

$$L = z \frac{\text{TI}_x}{a} \quad (5.4)$$

where z and a denote the height above the ground and the shear exponent according to Eq. 2.68, respectively. The shear exponent is chosen as $a = 1/7$ as it represents neutral conditions (Schlichting and Gersten, 2016). Since the focus of this work shall be placed on wind energy applications, a representative value for the hub height of wind turbines (rotor's height above the ground, see Fig. 5.3) as value for z is used for this purpose. The average hub height of wind turbines installed in 2018 in Germany is given by 133 m (Häuser and Keiler, 2018). The corresponding value according to Eq. 5.4 is used for all LES considered in this work.

The parameter $c_K \varepsilon^{2/3}$ is derived from the rescaling of the initially generated field. As explained in Section 4.1, a rescaling of the field $\mathbf{u}(x)$ with a scaling factor SF implies a rescaling of $c_K \varepsilon^{2/3}$ with the factor SF^2 due to the proportionality between $\mathbf{u}(x)$ and $\sqrt{c_K \varepsilon^{2/3}}$. The remaining constituting parameters Γ and L remain unaffected thereby. Average longitudinal turbulence intensities of 5 %, 10 % and 15 % for an isotropic case ($\Gamma = 0$) and an anisotropic case with $\Gamma = 4$ at $\langle U \rangle = 10 \text{ m s}^{-1}$ are considered.

All sets of parameters for LES used in scope of this work are given in Appendix D.

5.2 Verification of the Inflow Method

In order to verify the volume force method described in Section 3.3, allowing the acceleration and deceleration of the flow for the introduction of a turbulent velocity field, a Large Eddy Simulation with an input velocity field $\mathbf{u} = u_x \hat{x}$, where $u_x \in \{\pm 0.5 \text{ m s}^{-1}, \pm 1 \text{ m s}^{-1}, \pm 2 \text{ m s}^{-1}\}$ is chosen as a piecewise constant step function as shown in Fig. 5.4 (A), is evaluated. In order to eliminate possible cyclic variability, the total simulated time is chosen long enough to include two subsequent

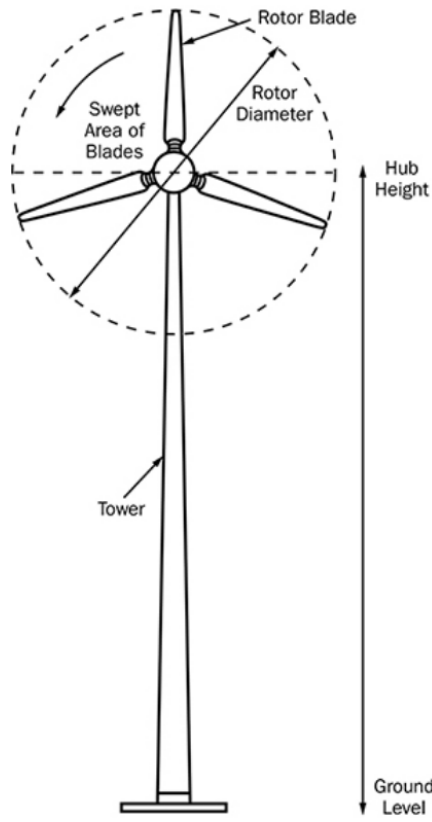


FIGURE 5.3: Horizontal axis wind turbine with major components. Taken from Clarke (2003).

inflow fields of this kind over which an average is considered. The mean velocity is chosen as $\langle U \rangle = 10 \text{ m s}^{-1}$. Fig. 5.4 (B) depicts the resulting output velocity fluc-

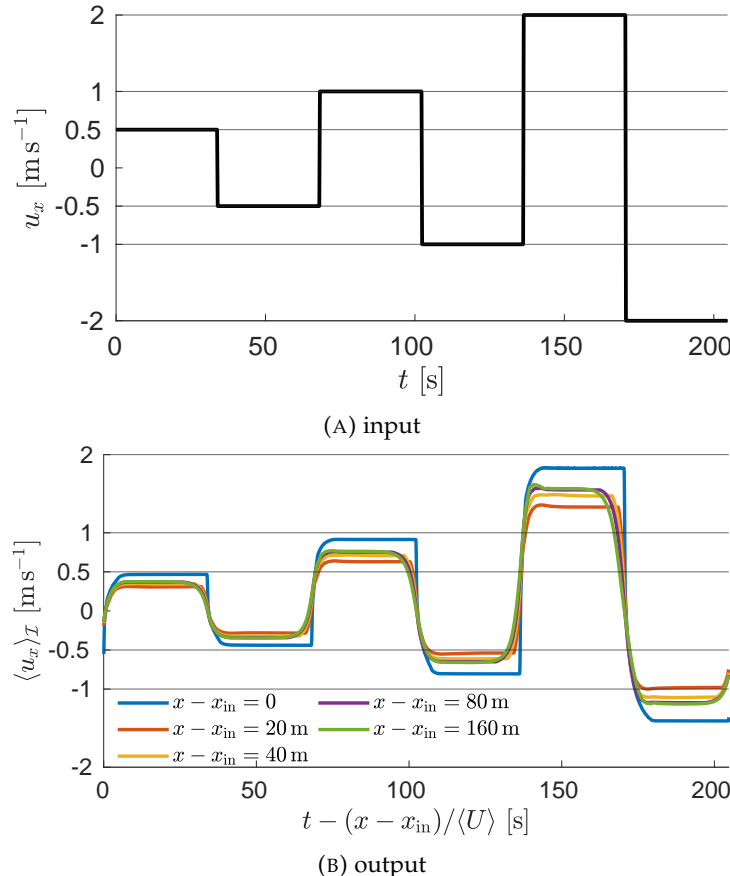


FIGURE 5.4: Piecewise constant step function as input field for the verification of the inflow method (A) and resulting velocity field in LES, averaged over the inlet (y, z)-plane (B).

tuation at different distances to the inlet patch in upstream direction, averaged over the (y, z) plane of the inlet. Each time axis is shifted according to Taylor's hypothesis (Eq. 2.27) in order consider comparable temporal courses. From the resulting velocities in the LES, it is clearly evident that the magnitude of the output velocity in the LES is always smaller than the respective input value, whereby this difference increases with the magnitude of the input velocity. It can thus be concluded, that the considered inflow method should only be used for input fields with small magnitude compared to the mean flow velocity and therefore small turbulence intensities. It is also apparent that the deviation of the resulting velocity from the target value is generally more pronounced for negative velocity fluctuations (i. e., for deceleration). The asymmetry between acceleration and deceleration becomes more distinct with increasing magnitude of the input field as can be seen in Fig. 5.5 which shows the ratio of output to input velocity fluctuations.

Furthermore, the application of the volume force leads to a locally sharply confined velocity jump around $x = x_{\text{in}}$ bounded by local minima for acceleration and maxima for deceleration, respectively. The velocity for $x \gg x_{\text{in}}$ however builds up slowly towards an approximately constant value, whose magnitude is significantly smaller than the target value.

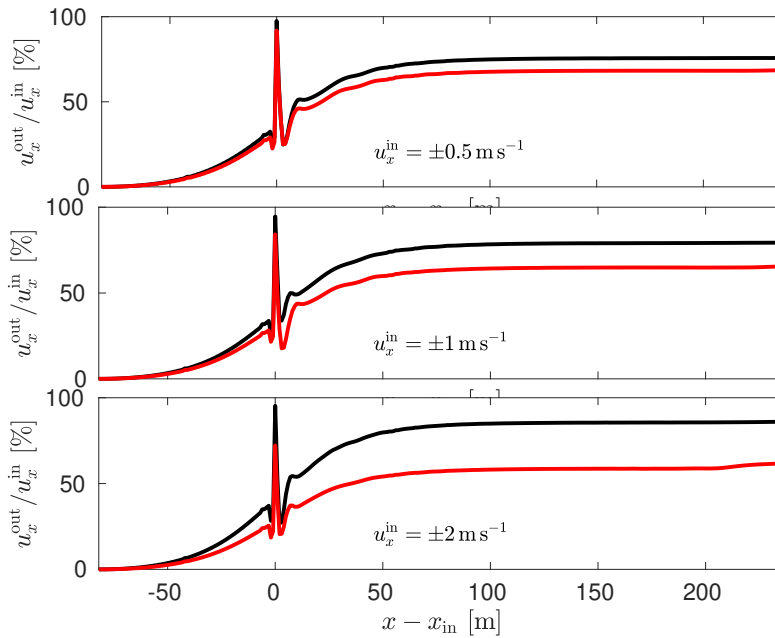


FIGURE 5.5: Ratio of the magnitude of output and input velocity field for acceleration (black) and deceleration (red).

5.3 Influence of the Spatial Resolution

It has been proven that the spatial resolution of the LES should chosen significantly higher than the spatial resolution of the inflow field. Fig. 5.6 shows the spatially averaged spectra of all three velocity components in LES at an exemplary distance of $x - x_{\text{in}} = 100$ m to the inlet of a Mann box with $\text{TI}_x \approx 5\%$ for two different spatial resolutions. $\Delta x_i = 2$ m corresponds to the spatial resolution of the inflow Mann box itself. It is clearly evident that a lower spatial resolution leads to a more pronounced decay of the spectra at high frequencies exclusively due to numerical reasons since the inflow field and all parameters are otherwise exactly alike.

This effect is also reported in others studies, e. g., by Thomas and Williams (1999) and Xie et al. (2004). According to them, this effect can be explained by the numerical dissipation of the discretization schemes and the finite length of the top-hat filter (Eq. 3.2). In order to keep the error small, a spatial resolution of $\Delta x_i = 1$ at $\delta x_i = 2$ m (spatial resolution of the Mann box) is chosen for all subsequent simulations.

One approach to describe the discrepancy between actual solution and numerical solution of the governing equations is the *modified equation* (Pope, 2001)

$$\frac{\tilde{D}\tilde{U}_i}{\tilde{D}t} = -\frac{1}{\rho} \frac{\partial \tilde{p}}{\partial x_i} + \nu \frac{\partial^2 \tilde{U}_i}{\partial x_j \partial x_j} - \frac{\partial}{\partial x_j} (\tau_{ij}^R + \tau_{ij}^n) \quad (5.5)$$

which corresponds to the LES momentum equation (Eq. 3.7). The numerical stress τ_{ij}^n represents the spatial-truncation error and is a function of the grid spacing, i. e., the spatial resolution. The dissipation rate resulting from it is given as

$$\varepsilon_n = -\tau_{ij}^n \bar{S}_{ij} \quad (5.6)$$

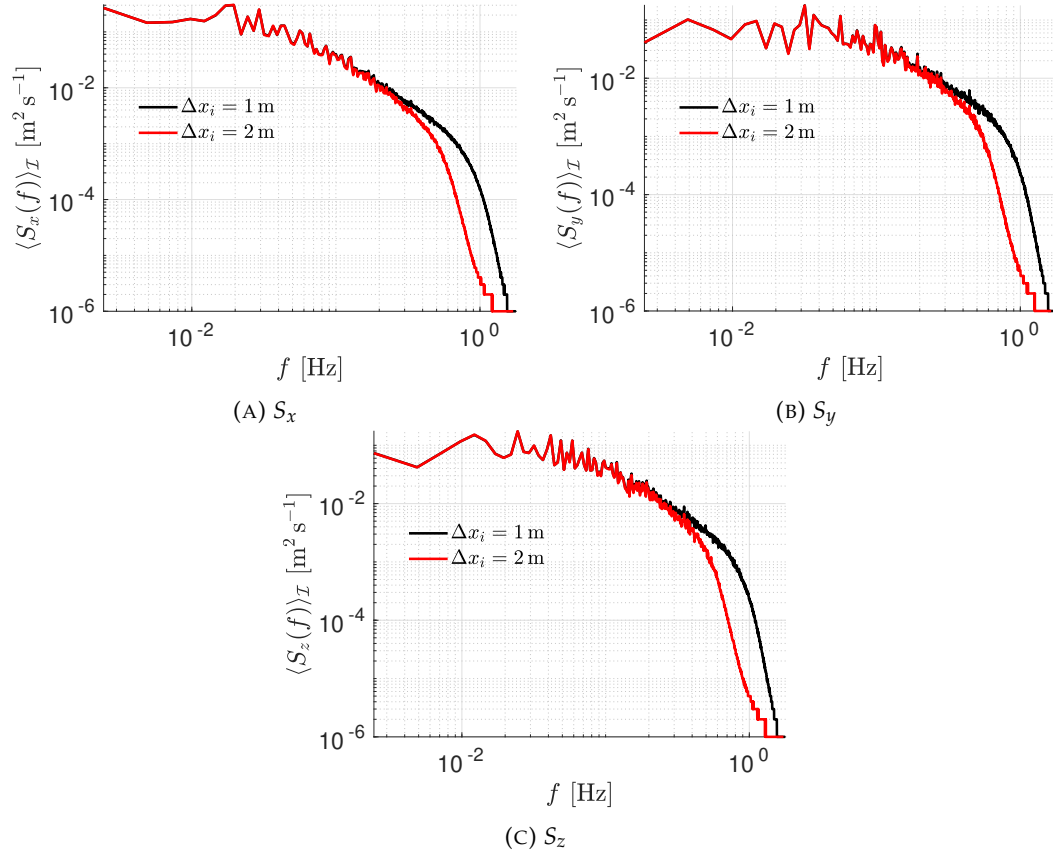


FIGURE 5.6: Spatially averaged one-point spectra $S_i(f)$ for all velocity components in LES for isotropic inflow with $\text{TI}_x \approx 5\%$ at $x - x_{\text{in}} = 100\text{ m}$ for different spatial resolutions of the LES domain.

5.4 One-Point Spectra

The velocity is now considered in the time domain at fixed location in streamwise direction. Therefore, the one-point spectra relate to the frequency domain and are thus denoted as $S_i(f)$ in distinction to the previously considered spectra in the wavenumber domain $F_i(\kappa_x)$. Figs. 5.7 – 5.9 depict the spectra of all three velocity components in the case of both isotropic and anisotropic inflow at different distances to the inlet plane for inflow fields with average longitudinal TI of 5%, 10% and 15%, respectively, in comparison to the spectra of the pure inflow field.

It is found that the spectra of all velocity components for low frequencies up to approximately 10 Hz are generally in good agreement with the input spectra. Only slight attenuation, which becomes more pronounced with increasing distance to the inlet plane, is apparent. For higher frequencies, however, the spectra are significantly damped. Notable differences can be seen between spectra of the velocity directly at the inflow location and at the remaining considered locations at which the highest damping occurs. These findings apply for the isotropic case as well as for the non-isotropic case.

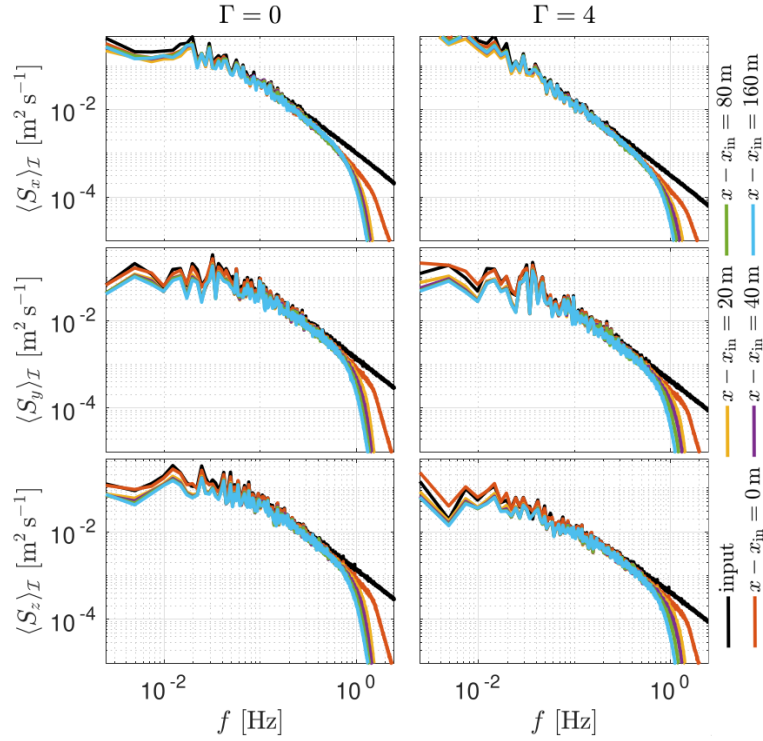


FIGURE 5.7: Spatially averaged power spectral densities in LES for isotropic ($\Gamma = 0$) and anisotropic ($\Gamma = 4$) inflow with input turbulence intensity of $\langle Tl_x^{\text{in}} \rangle_{\mathcal{I}} = 5\%$ for different distances $x - x_{\text{in}}$ to the inlet plane in streamwise direction.

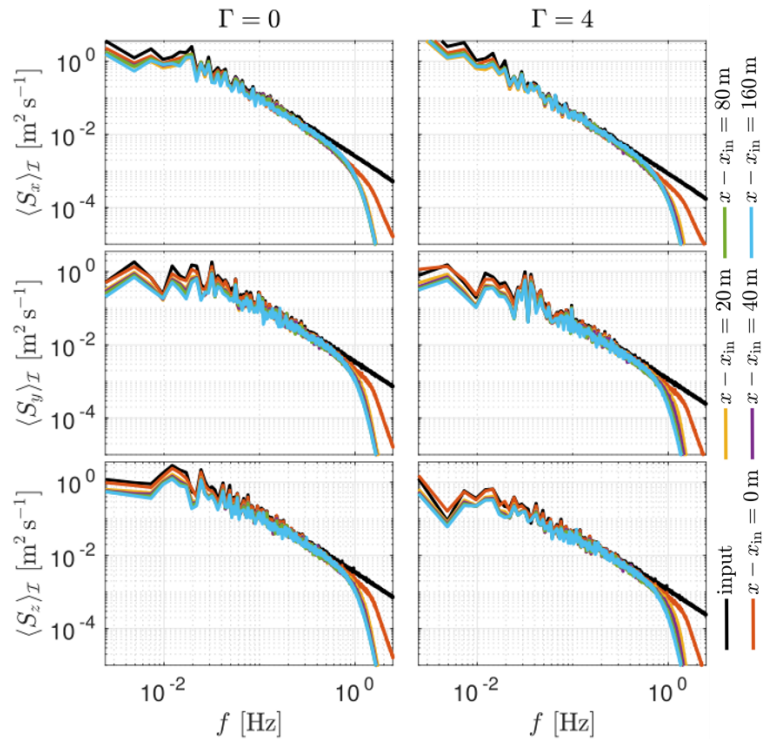


FIGURE 5.8: Spatially averaged power spectral densities in LES for isotropic ($\Gamma = 0$) and anisotropic ($\Gamma = 4$) inflow with input turbulence intensity of $\langle Tl_x^{\text{in}} \rangle_{\mathcal{I}} = 10\%$ for different distances $x - x_{\text{in}}$ to the inlet plane in streamwise direction.

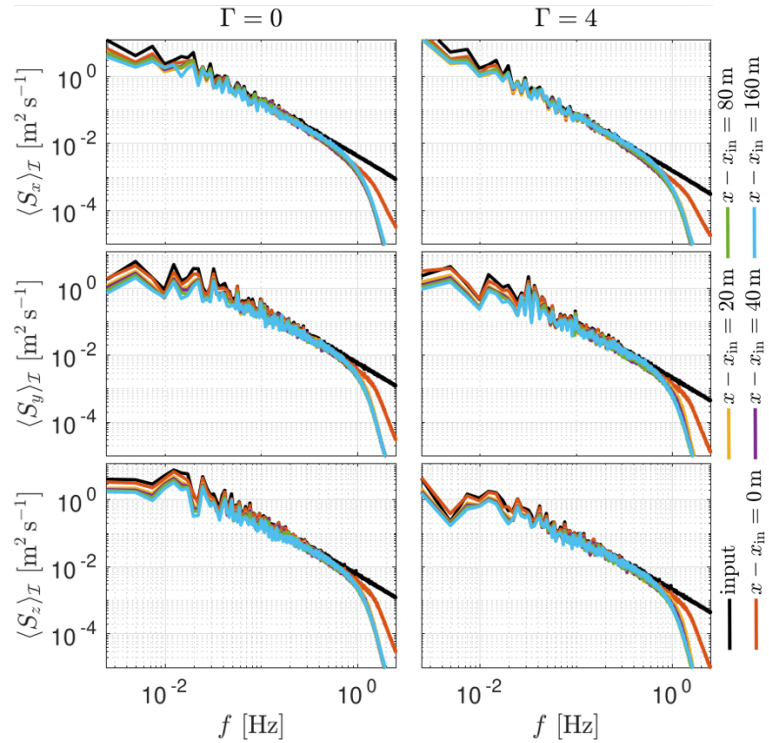


FIGURE 5.9: Spatially averaged power spectral densities in LES for isotropic ($\Gamma = 0$) and anisotropic ($\Gamma = 4$) inflow with input turbulence intensity of $\langle \text{TI}_x^{\text{in}} \rangle_{\mathcal{I}} = 15\%$ for different distances $x - x_{\text{in}}$ to the inlet plane in streamwise direction.

5.5 Turbulence Intensities

As mentioned, the turbulence intensity TI_i of the i -th velocity component is another important quantity for the statistical description of turbulence, especially in the fields of aerodynamics. It allows for the expression of the degree of turbulent fluctuations, related to the velocity of the mean flow that is causing their advection, in a single number. It is thus of great interest to understand how the turbulence intensities of the velocity components evolve inside the LES domain along the streamwise direction. For this purpose, the average $\langle \text{TI}_i \rangle_{\mathcal{I}}$ with respect to the inlet plane and the respective spatial standard deviation as a function of the longitudinal distance to the inlet plane at $x = x_{\text{in}}$ were calculated and compared to their corresponding values that arise from the original, unchanged input field. The results are presented in Figs. 5.10 – 5.12.

As described in Section 5.1, the input fields for the LES are each rescaled so that their average standard deviations $\langle \sigma_x \rangle_{\mathcal{I}}$ correspond to longitudinal turbulence intensities of 5 %, 10 % and 15 %, respectively, for the given mean velocity of $\langle U \rangle = 10 \text{ m s}^{-1}$. The purpose of this rescaling is to achieve the same average value for TI_x for the isotropic and the non-isotropic case and therefore provide greater comparability between both cases. It is, however, not easily possible to achieve the same spatial standard deviation $\sqrt{\langle \sigma_x^2 \rangle_{\mathcal{I}} - \langle \sigma_x \rangle_{\mathcal{I}}^2}$ of the velocity standard deviation σ_x for both. For the considered cases here, the spatial standard deviation of σ_x is generally higher for the non-isotropic case with $\Gamma = 4$ than for the isotropic case with $\Gamma = 0$. This should

be taken into account when comparing both inflow conditions. The significant differences between the standard deviations of all velocity components—and therefore also the turbulence intensities—for $\Gamma = 4$ are part and expression of the anisotropy as explained in Section 2.3.1.

Considering first the longitudinal turbulence intensity, it is found that TI_x is initially steadily increasing towards $x = x_{\text{in}}$. However, the target TI, i. e., the respective value of the input field, is generally not fully reached. Subsequently, the value of TI_x experiences a sudden drop and then builds up towards a local maximum, followed by a slow and steady decrease which was also observed for constant input fields $\mathbf{u} = u_x \hat{\mathbf{x}}$ that were considered for the purpose of verification of the volume force based inflow method (see Fig. 5.5). In contrast, the TI for the transverse components TI_y and TI_z do not experience a sharp drop and a subsequent "build-up" effect but steadily decrease for $x > x_{\text{in}}$ in all simulations.

By comparison, the deviation between actual turbulence intensities in LES and the desired turbulence intensities of the input field is greater the higher the target longitudinal TI is. This can primarily be explained by the inflow method (see Section 5.2). The differences between input velocity and the corresponding velocity in LES resulting from it are increasing with the magnitude of the input velocity, as can be seen in Fig. 5.4. The effect is also graphically illustrated in Fig. 5.13 which shows the ratios of the spatially averaged TIs to the respective initial value of the input field at an exemplary distance of $x - x_{\text{in}} = 100$ m to the inlet plane.

Another important result to be noted is that the longitudinal turbulence intensity TI_x for $\Gamma = 4$ is generally more markedly damped than for $\Gamma = 0$ (see Fig. 5.13). A direct link between the damping of the one-point spectra (Figs. 5.7 – 5.9) and the decrease of the turbulence intensities in LES can be made. The one-point spectra represent the contribution of the wavenumber or, equivalently,² the frequency on the variance (see, for instance, Eq. 4.4). The attenuation of the turbulence intensities can thus to a large extent be attributed to the high frequencies at which the spectra are significantly damped.

²According to Taylor's hypothesis, the relation between longitudinal wavenumber κ_x and frequency f is given by $\kappa_x = 2\pi f / \langle U \rangle$.

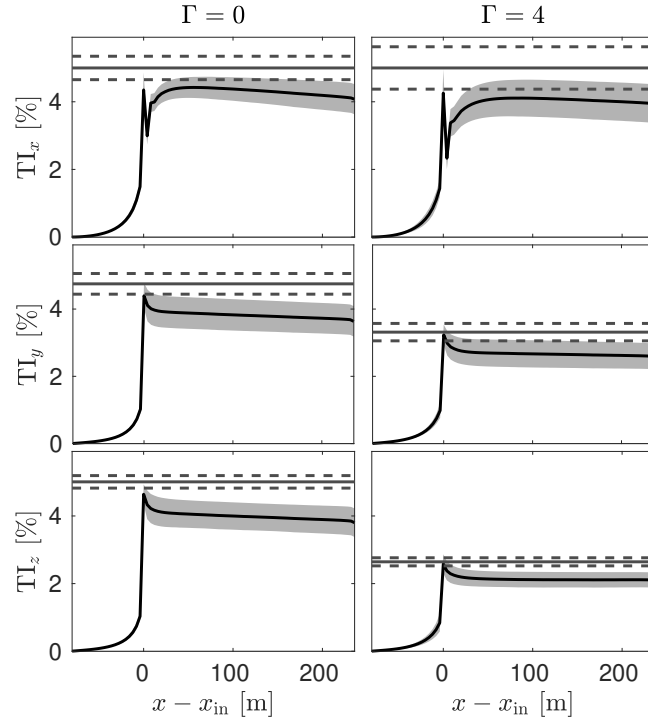


FIGURE 5.10: Turbulence intensities in LES for isotropic ($\Gamma = 0$) and anisotropic ($\Gamma = 4$) inflow with input turbulence intensity of $\langle TI_x^{\text{in}} \rangle_{\mathcal{I}} = 5\%$. Solid black line represents the spatial average, whereas the shaded area around the average represents one spatial standard deviation of uncertainty ($\langle TI_i \rangle_{\mathcal{I}} \pm \sqrt{\langle \sigma_x^2 \rangle_{\mathcal{I}} - \langle \sigma_x \rangle_{\mathcal{I}}^2}$). The solid horizontal line corresponds to the average TI of the input field whereas the dashed lines refer to the respective spatial standard deviation.

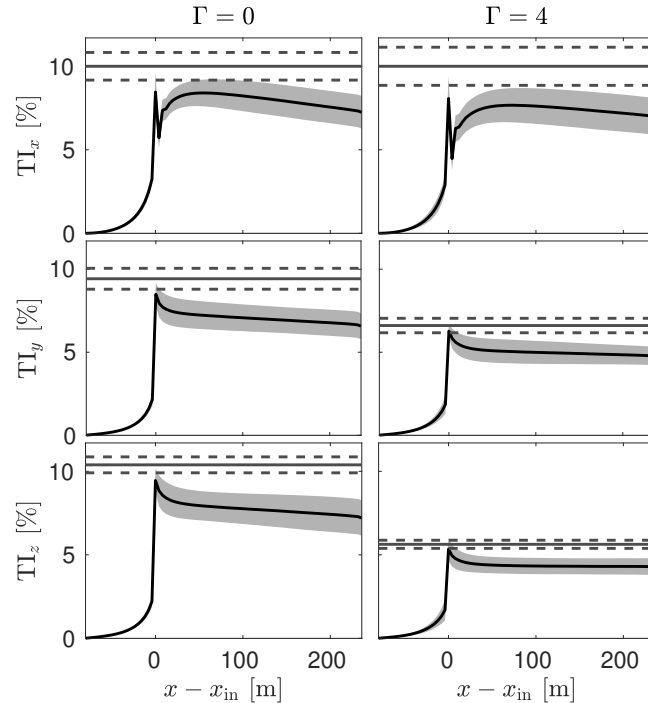


FIGURE 5.11: Turbulence intensities in LES for isotropic ($\Gamma = 0$) and anisotropic ($\Gamma = 4$) inflow with input turbulence intensity of $\langle TI_x^{\text{in}} \rangle_{\mathcal{I}} = 10\%$. Same representation as in Fig. 5.10.

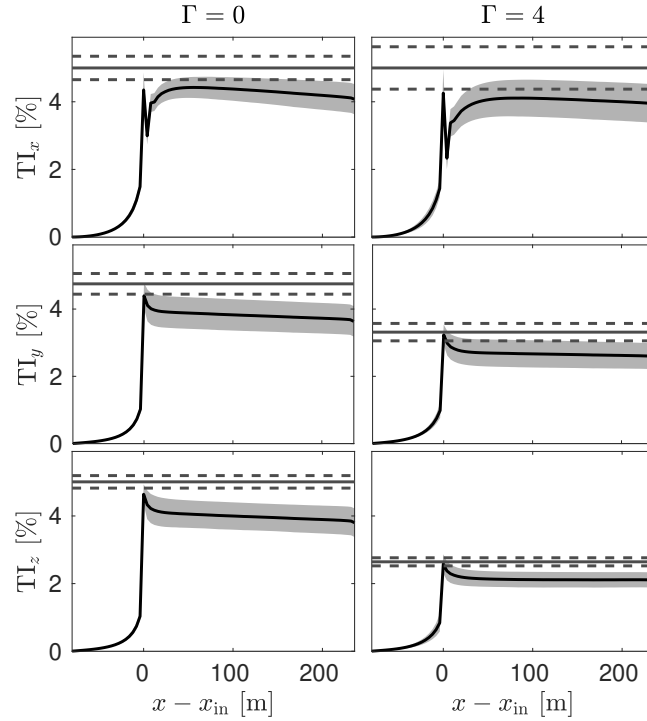


FIGURE 5.12: Turbulence intensities in LES for isotropic ($\Gamma = 0$) and anisotropic ($\Gamma = 4$) inflow with input turbulence intensity of $\langle \text{TI}_x^{\text{in}} \rangle_{\mathcal{I}} = 15\%$. Same representation as in Fig. 5.10.

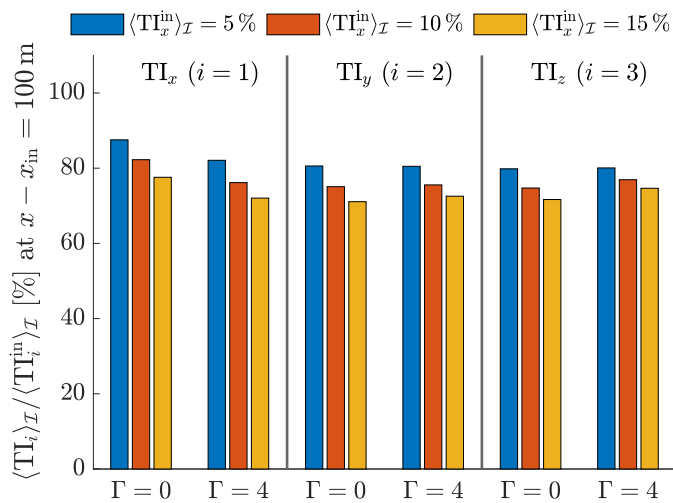


FIGURE 5.13: Ratios of spatially averaged turbulence intensities $\langle \text{TI}_i \rangle_{\mathcal{I}}$ in LES and respective input turbulence intensities $\langle \text{TI}_i^{\text{in}} \rangle_{\mathcal{I}}$ for all simulations at an exemplary distance of 100 m to the inlet plane.

5.6 Coherence

In a similar manner to the analysis of one-point spectra in the LES (Section 5.4), the coherence of all velocity components with different horizontal separations $\Delta y > 0$ is considered at different distances to the inlet plane at $x = x_{\text{in}}$. The results are depicted in Figs. 5.14 – 5.16. It may be noted that the horizontal axes corresponds to the previously considered axes in plots for the coherence in the wavenumber domain according to Taylor's hypothesis:

$$\frac{2\pi f}{\langle U \rangle} = \kappa_x. \quad (5.7)$$

In general, the coherence of the velocity components in LES most closely matches the coherence that arises from the unchanged input velocity field for large values of the horizontal spatial separation Δy . From the coherence with the smallest separation of $\Delta y = 2 \text{ m}$, it further appears that the difference between input coherence and coherence of the velocity in LES is generally larger for high frequencies than for small frequencies. These findings indicate that changes in the coherence of the velocity particularly occur on small temporal and spatial scales. This is consistent with the damping of the velocity spectra (Section 5.4) at high frequencies.

Moreover, the agreement between input and LES coherence seem to become worse for an increasing value of the turbulence intensity $\langle \text{TI}_x^{\text{in}} \rangle_{\mathcal{I}}$. Again, this is partly due to the reduced validity of the volume-force inflow method (see, for instance, Fig. 5.5) for large inflow velocity magnitudes. It can further be attributed to an increased dissipation rate that is associated with high turbulence intensities (Azevedo et al., 2017) and which leads to a damping of the turbulent structures. Numerical dissipation (see Section 5.3) is of course a further relevant factor for the difference between the coherence of the input velocity field and the coherence of the respective LES data in general.

Another finding, that is visible in the observed frequency range, is the strong increase of $\text{coh}_{xx}(f)$ and $\text{coh}_{yy}(f)$ for the non-isotropic case with $\langle \text{TI}_x^{\text{in}} \rangle_{\mathcal{I}} = 5\%$ at $\Delta y = 2 \text{ m}$ (Fig. 5.14, B) and of $\text{coh}_{yy}(f)$ for the non-isotropic case with $\langle \text{TI}_x^{\text{in}} \rangle_{\mathcal{I}} = 10\%$ at $\Delta y = 2 \text{ m}$ (Fig. 5.15, B). Since the coherence was only computed for certain distances to the inlet plane, similar behaviour may be occurring for the remaining velocity components and spatial separations Δy at other locations. It should furthermore be noted that the highest frequency in the leftmost plots in Figs. 5.14 – 5.16 ($\Delta y = 2 \text{ m}$) refer to the smallest spatial scales according to Taylor's hypothesis due to the scaling of the frequency axis with the spatial separations Δy . It is therefore possible that the stated increase of the coherence can be explained by the influence of the spatial resolution of the LES in this frequency range.

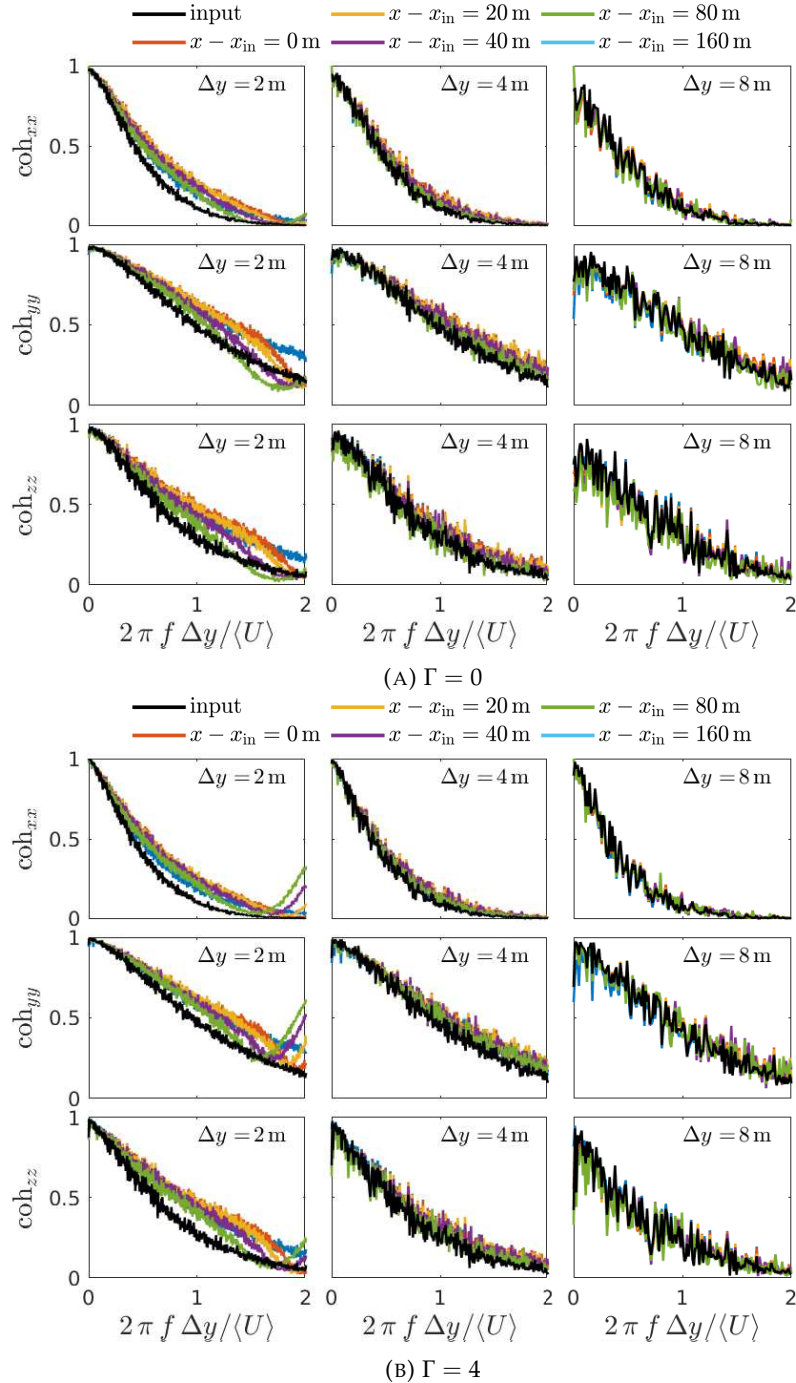


FIGURE 5.14: LES coherence in frequency domain for different horizontal separations Δy at different distances $x - x_{\text{in}}$ to the inlet plane in comparison to coherence of modeled input field with $\langle T\Gamma_x^{\text{in}} \rangle_{\mathcal{I}} = 5\%$ for isotropic ($\Gamma = 0$, A) and anisotropic inflow ($\Gamma = 4$, B).

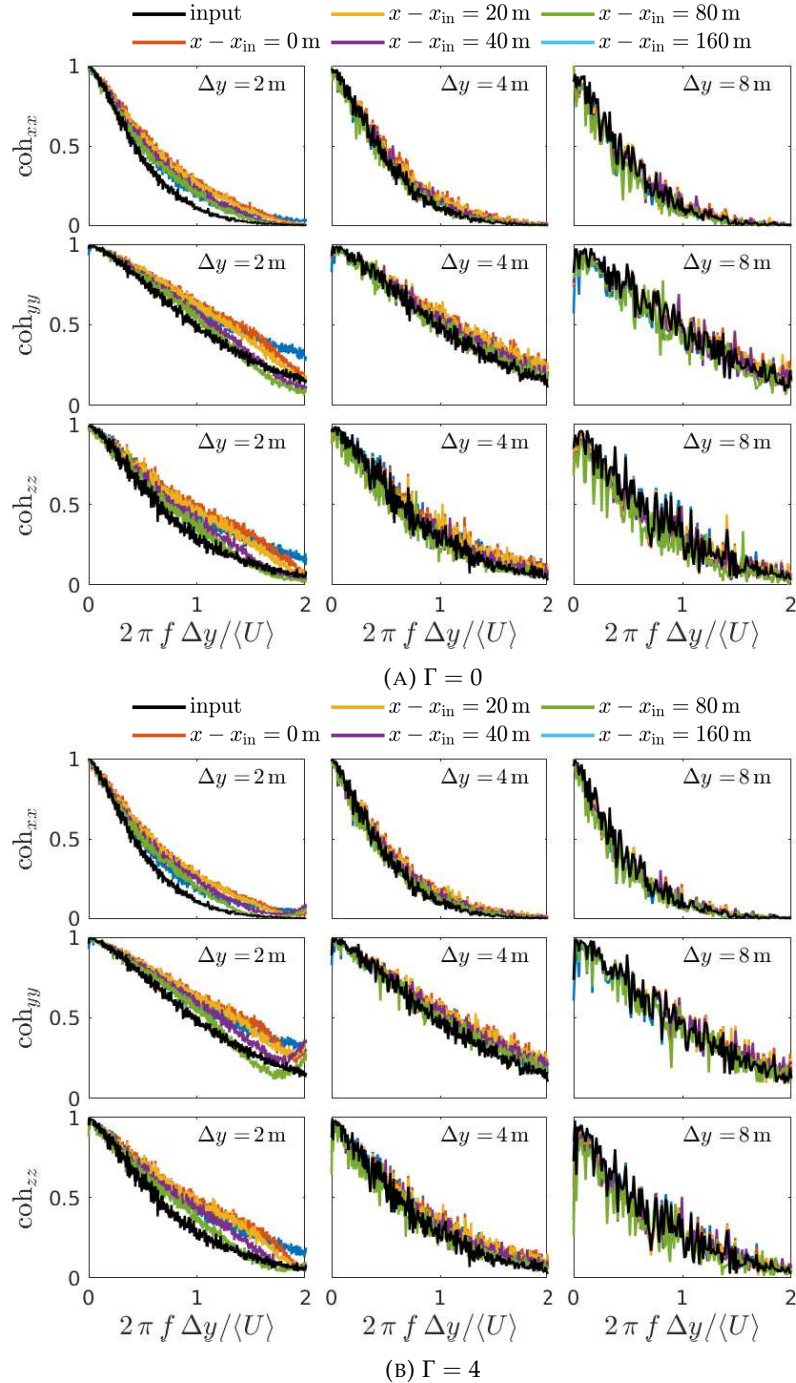


FIGURE 5.15: LES coherence in frequency domain for different horizontal separations Δy at different distances $x - x_{\text{in}}$ to the inlet plane in comparison to coherence of modeled input field with $\langle T_i^{\text{in}} \rangle_I = 10\%$ for isotropic ($\Gamma = 0$, A) and anisotropic inflow ($\Gamma = 4$, B).

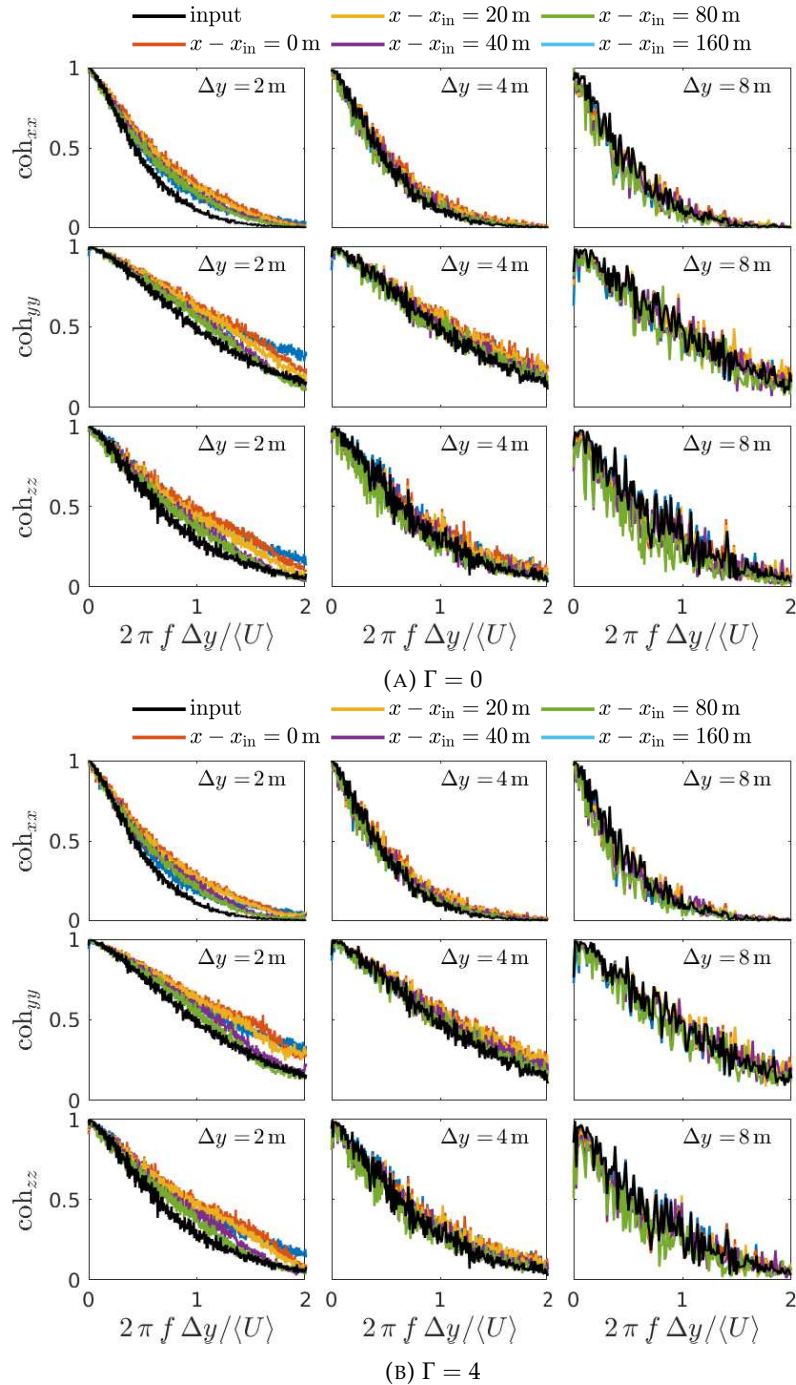


FIGURE 5.16: LES coherence in frequency domain for different horizontal separations Δy at different distances $x - x_{\text{in}}$ to the inlet plane in comparison to coherence of modeled input field with $\langle T_i^{\text{in}} \rangle_I = 15\%$ for isotropic ($\Gamma = 0$, A) and anisotropic inflow ($\Gamma = 4$, B).

5.7 Increment Statistics

As described in Section 4.4, the Mann turbulence model does not capture the characteristic of intermittency. Hence, velocity increments follow Gaussian distributions (see Fig. 4.10). In LES, however, the Navier-Stokes equations (although given for a scale-filtered velocity field and scale-filtered pressure) are solved. They describe turbulent flow in its entirety and thus intermittency is inherent to them (see, for instance, Biferale et al., 2006). It is therefore interesting to investigate the development of intermittency in LES with the given inflow fields. For this purpose, the velocity increment

$$u_\tau = u_x(\mathbf{x}, t + \tau) - u_x(\mathbf{x}, t) \quad (5.8)$$

is considered in the temporal domain, i. e., with respect to a temporal separation τ . The resulting probability distribution functions for u_τ for temporal separations from $\tau = 0.05$ s to $\tau = 1.6$ s at an exemplary distance of 80 m to the inlet plane in streamwise direction are shown separately for isotropic and non-isotropic inflow in Figs. 5.17 – 5.19. The figures correspond to average longitudinal input turbulence intensities of 5 %, 10 % and 15 %, respectively. While deviations of the velocity increment PDFs from Gaussian distributions are barely notable for an input longitudinal TI of $\langle \text{TI}_x^{\text{in}} \rangle_{\mathcal{I}} = 5$ %, they can clearly be observed for $\langle \text{TI}_x^{\text{in}} \rangle_{\mathcal{I}} = 10$ % and are most pronounced for $\langle \text{TI}_x^{\text{in}} \rangle_{\mathcal{I}} = 15$ %.

With direct numerical simulations of homogeneous isotropic turbulence as well as for turbulent Rayleigh-Bénard convection³, Schumacher et al. (2014) could, by means of velocity gradient statistics, show that intermittency becomes more pronounced with increasing Reynolds number. It seems therefore reasonable to assume that intermittency and thus non-Gaussian velocity increments become as well more pronounced for high turbulence intensities.

The deviation of $p(u_\tau)$ from Gaussian distributions, given in the form of heavy tails of the PDFs, are highest for small time scales τ which is in agreement with experimental results (e. g., Kailasnath et al., 1992).

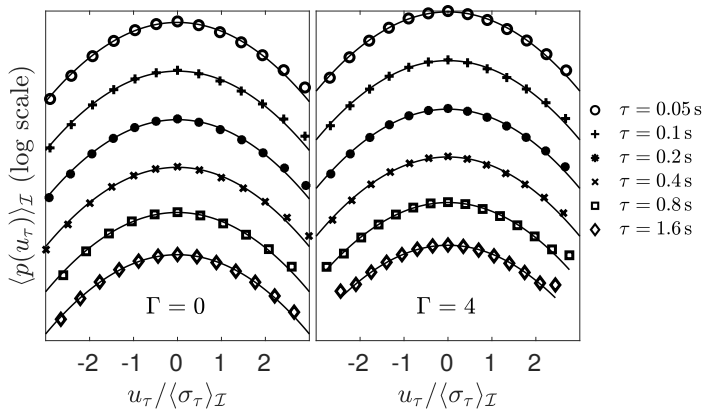


FIGURE 5.17: PDFs of u_τ in LES for isotropic ($\Gamma = 0$) and anisotropic ($\Gamma = 4$) inflow with $\langle \text{TI}_x^{\text{in}} \rangle_{\mathcal{I}} = 5$ % at $x - x_{\text{in}} = 80$ m. PDFs are shifted in vertical direction for the sake of clarity. Solid lines represent Gaussian distributions with the same respective standard deviation.

³Rayleigh-Bénard convection is a simple model for thermal convection in a horizontal fluid layer under the influence of gravity that is heated from below and cooled from above.

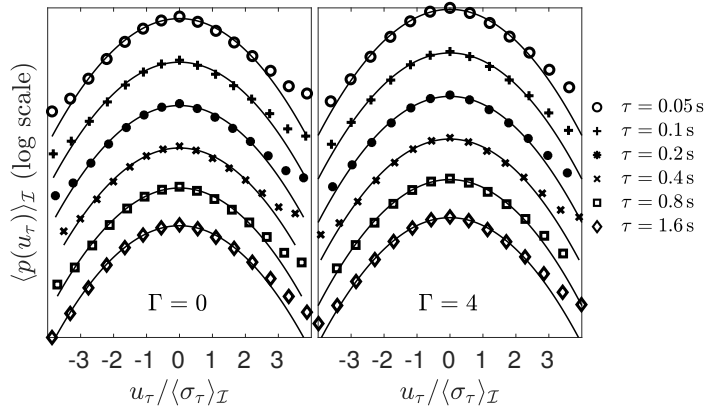


FIGURE 5.18: PDFs of u_τ in LES for isotropic ($\Gamma = 0$) and anisotropic ($\Gamma = 4$) inflow with $\langle \text{TI}_x^{\text{in}} \rangle_{\mathcal{I}} = 10\%$ at $x - x_{\text{in}} = 80\text{ m}$. PDFs are shifted in vertical direction for the sake of clarity. Solid lines represent Gaussian distributions with the same respective standard deviation.

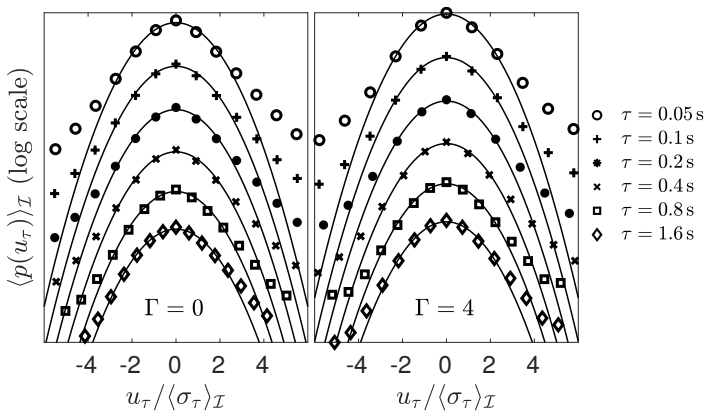


FIGURE 5.19: PDFs of u_τ in LES for isotropic ($\Gamma = 0$) and anisotropic ($\Gamma = 4$) inflow with $\langle \text{TI}_x^{\text{in}} \rangle_{\mathcal{I}} = 15\%$ at $x - x_{\text{in}} = 80\text{ m}$. PDFs are shifted in vertical direction for the sake of clarity. Solid lines represent Gaussian distributions with the same respective standard deviation.

In order to quantify the non-Gaussian behaviour of velocity increments at different distances to the inlet plane, the kurtosis (Eq. 2.25) of u_τ is considered. Figs. 5.20 A – C show $\text{Kurt}(u_\tau)$ as a function of the temporal separation τ at different values for $x - x_{\text{in}}$ for isotropic and non-isotropic inflow at $\langle \text{TI}_x^{\text{in}} \rangle_{\mathcal{I}} \in \{5\%, 10\%, 15\%\}$. It is evident that the kurtosis generally becomes larger with increasing distance. Overall, the kurtosis of the increment decreases with τ and reaches $\langle \text{Kurt}(u_\tau) \rangle_{\mathcal{I}} \approx 3$, i. e., Gaussian behaviour at $\tau \sim \mathcal{O}(10\text{ s})$. However, the kurtosis of u_τ directly at $x = x_{\text{in}}$ must be considered separately. Directly at the inlet plane, a very different behaviour from the kurtosis at other locations is observed. Even though it also approaches 3 at large values of τ , the course of $\langle \text{Kurt}(u_\tau) \rangle_{\mathcal{I}}$ takes a different form for small temporal scales. This should be insignificant for most applications though. Further, it is noted that the magnitude of the kurtosis for isotropic and non-isotropic inflow generally differ. It seems that for the non-isotropic case, the intermittency is generally more pronounced at large distances to the inflow location.

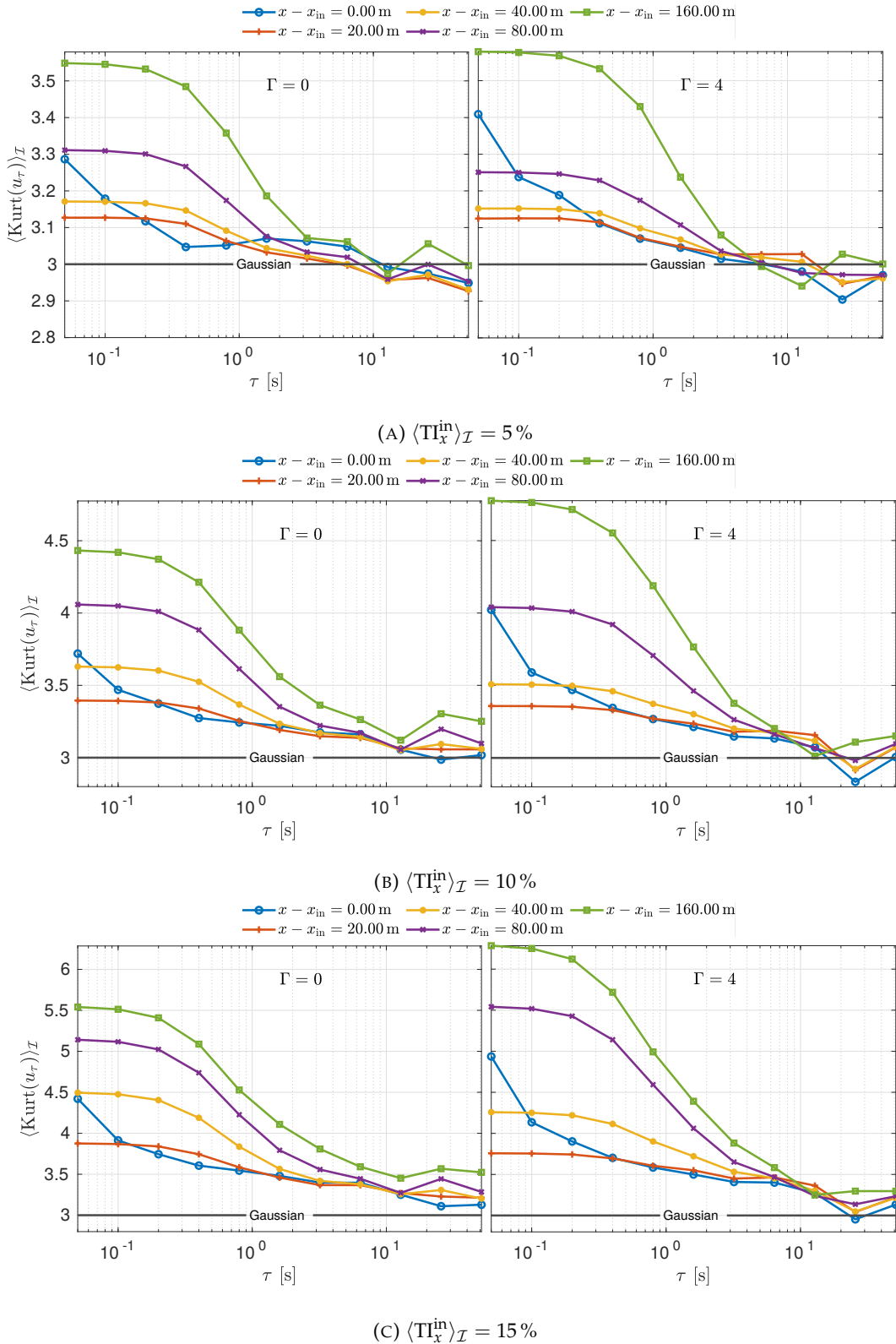


FIGURE 5.20: Spatially averaged kurtosis of velocity increments in LES for isotropic ($\Gamma = 0$) and anisotropic ($\Gamma = 4$) inflow with average longitudinal input turbulence intensity of 5% (A), 10% (B), 15% (C). The horizontal line represents the kurtosis for Gaussian distributions for comparison.

Chapter 6

Application of Stochastic Time Mapping to Mann Turbulence

This chapter deals with the application of the time-mapping process of the CTRW wind model by Kleinhans (2008), as described in Section 2.3.2, to Fourier simulated Mann turbulence (Section 2.3.1) after conversion of the longitudinal spatial coordinate into the time axis according to Taylor's hypothesis. For this purpose, the same exemplary set of physical parameters $\{\Gamma, L, c_K \varepsilon^{2/3}\}$ as for the analysis of Fourier simulated Mann turbulence in Chapter 4, based on the ESDU spectral model (ESDU, 1982), is considered. Since the focus in this chapter lies on the temporal statistics, a large number of points in x direction (which corresponds to the time axis) is considered. Due to limited computational capacities, the number of points in y and z direction is chosen correspondingly smaller. All parameters for the original velocity field are given in Tab. 6.1.

TABLE 6.1: Parameters of the Mann model derived from the ESDU spectral model (ESDU, 1982) and values for the number of points n_i in each direction and the spatial increments δx_i of the domain considered in the context of this chapter.

Γ	L	$c_K \varepsilon^{2/3}$	n_x	$n_y = n_z$	δx_i
4.5	66 m	$0.62 \text{ m}^{4/3} \text{ s}^{-2}$	8192	64	1 m

Through the time-mapping, the originally Gaussian velocity field is extended by leptokurtic velocity increments in longitudinal direction which takes adequate account of the effect of intermittency which is a further characteristic of turbulent flow and therefore also inherent in wind (Boettcher et al., 2003). At the same time, the application of the time-mapping process is accompanied by changes of the fields spectral properties as well as its divergence as explained in Sections 6.1 and 6.2. Finally, Section 6.3 addresses the influence of the time-mapping process on the velocity increment statistics.

In order to distinct the time axis of the original, unchanged Mann turbulence field and the time axis after the application of the CTRW time-mapping (see Eq. 2.104), the naming according to the nomenclature from the work of Kleinhans (2008) has been adopted for this chapter. This means that s denotes the time of the original field whereas t denotes the time of the field after the application of the time-mapping. Moreover, both time variables are expressed in terms of their spatial equivalents $s \langle U \rangle$ and $t \langle U \rangle$ according to Taylor's hypothesis. The representation of s and t is hence given in a generalized manner rather than for a specific value of $\langle U \rangle$. The representation is done analogously for the frequency f as the fraction $f / \langle U \rangle$.

Different values for the parameter $\alpha \in \{0.4, 0.5, \dots, 0.9\}$ that defines the shape of the Lévy distribution and thus the degree of intermittency are considered. Given the

parameters in Tab. 6.1. The total time of the wind field is given as $T = 9182 \text{ m}/\langle U \rangle$. The cutoff parameter c , that defines the truncation of the Lévy distribution, is chosen as $c = 8$. The increment Δs_t is chosen as $40 \text{ m}/\langle U \rangle$. The resulting mapping of the original time s to the rescaled time t is depicted in Fig. 6.1.

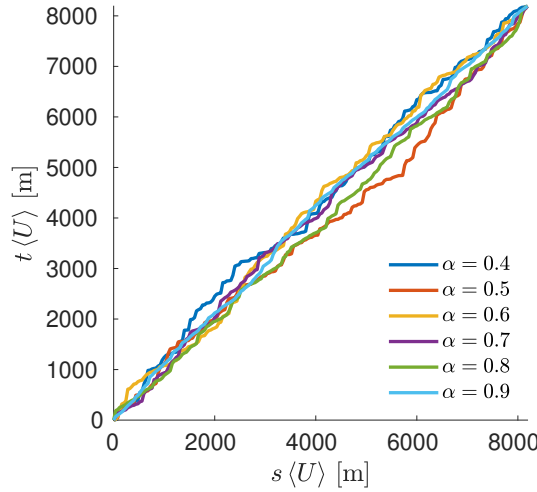


FIGURE 6.1: Representation of the time-mapping for $c = 8$, $\Delta s_t \langle U \rangle = 40 \text{ m}$ and different values for α .

As can be seen in Fig. 6.2, which shows the PDFs of $\tau_{\alpha,c} = dt/ds$ for all considered values of α , the time-mapping is consistent with the truncated Lévy distribution (Eq. 2.108) for the given cutoff c .

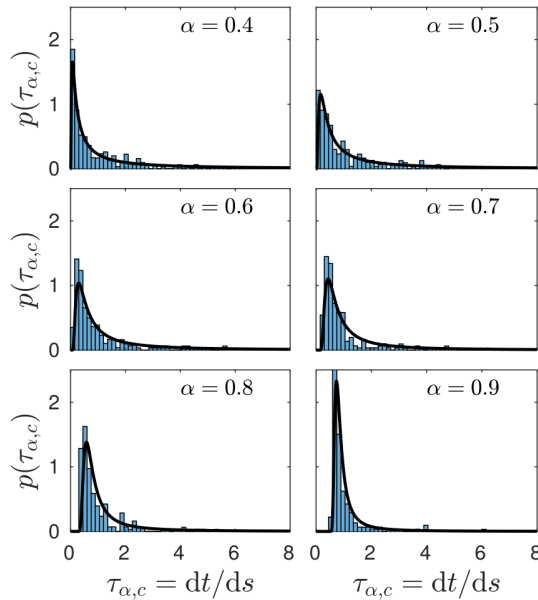


FIGURE 6.2: Histogram of $\tau_{\alpha,c} = dt/ds$ and analytical PDF according to Eq. 2.108 for $c = 8$, $\Delta s_t \langle U \rangle = 40 \text{ m}$ and different values for α .

6.1 Spectral Properties and Coherence

Fig. 6.5 depicts the one-point spectra of all velocity components that arise from the application of the time-mapping in comparison the spectra of the original velocity field, spatially averaged over the (y, z) plane perpendicular to the main stream direction. Changes due to the rescaled time-axis are most visible at high frequencies where the spectra are evidently attenuated (see magnified portions in Fig. 6.5). At low frequencies, however, the spectral changes are not as visible.

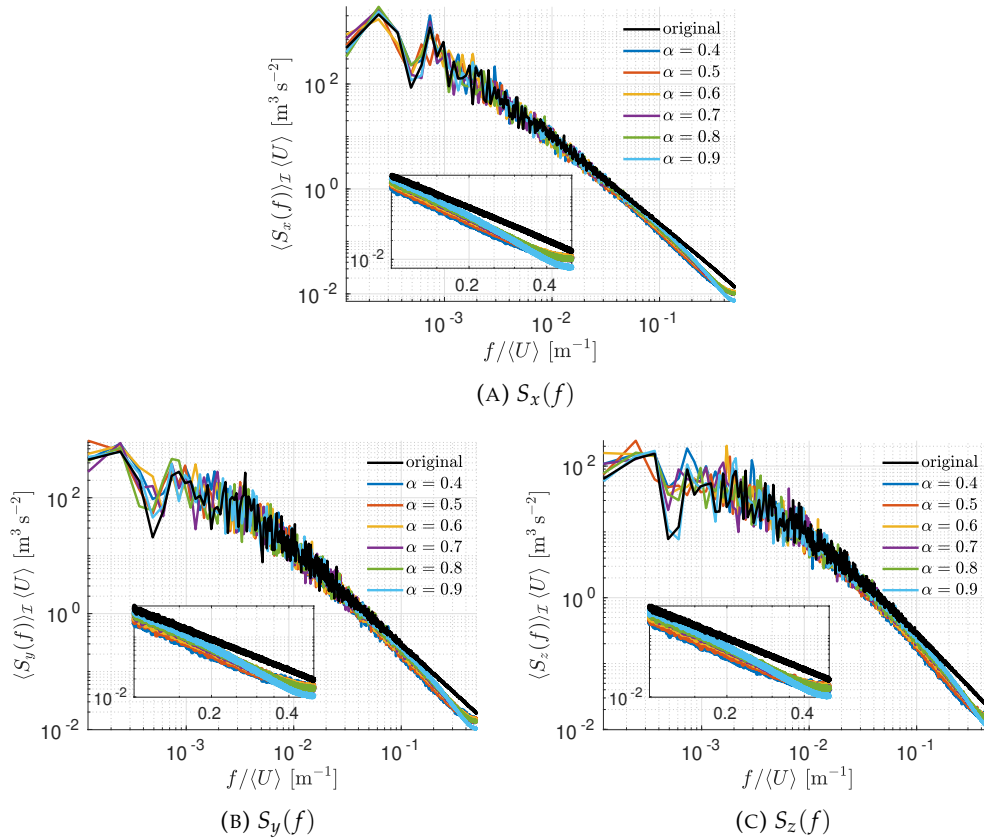


FIGURE 6.3: Spatially averaged power spectral densities of the velocity components before (original) and after application of the CTRW time-mapping with different values for α .

The effects on the velocity standard deviations, that can be attributed to the spectral changes, are depicted in Fig. 6.4. A clear correlation between the variation of σ_i and α can not be identified. Further, the changes of σ_i are relatively small and lie for the most part within the spatial standard deviation with regard to the (y, z) plane. This would allow for a rescaling of the time-mapped velocity field with respect to σ_i without strong alteration of its spatial structure.

In order to examine the changes of the coherence that are accompanied by the time-mapping process, horizontal spatial separations are considered. The resulting coherence is shown in Fig. 6.5. Differences between the coherence of the original velocity field and its time-mapped counterparts are primarily pronounced at high frequencies. Moreover, it seems that the coherence of the time-mapped fields is generally attenuated at lower frequencies and then increased at higher frequencies, which is most visible for $\Delta y = 2$ m in Fig. 6.5.

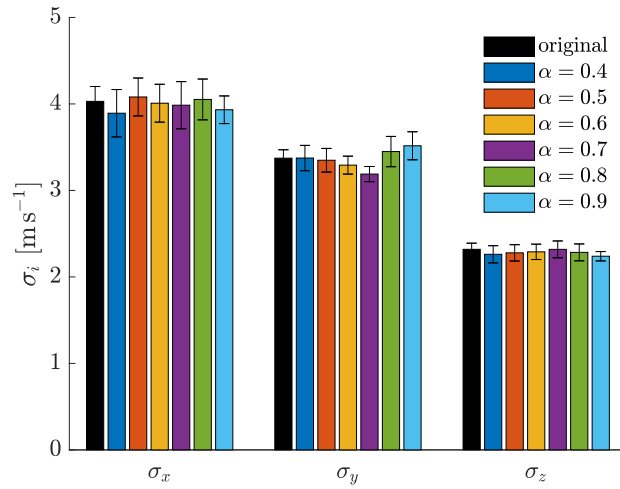


FIGURE 6.4: Average standard deviations of the velocity components due to the CTRW time-mapping. Error bars correspond to the spatial standard deviation of σ_i with respect to the (y, z) plane.

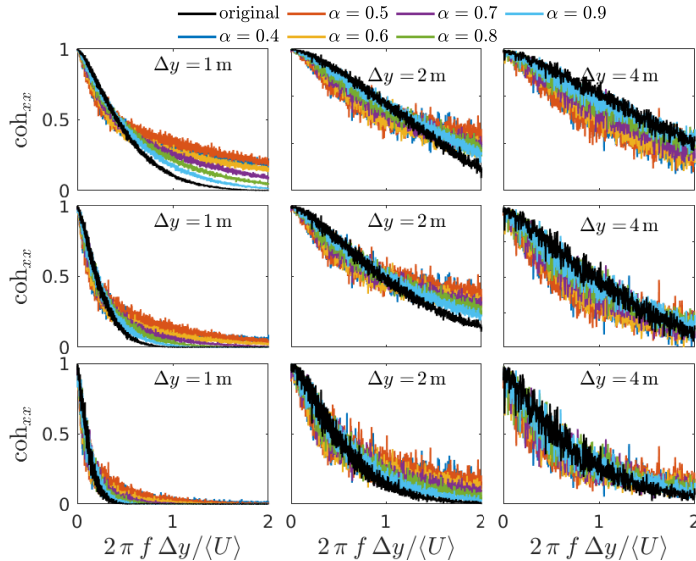


FIGURE 6.5: Coherence of time-mapped velocity field and original velocity field in comparison for different horizontal separations Δy .

6.2 Divergence

As mentioned previously in Section 4.3, the divergence of velocity fields is, in particular for their utilization as inflow conditions for numerical simulations of incompressible flows, of special significance. Considering the velocity fields again in the spatial domain by converting the time axis back to the x coordinate in accordance to Taylor's hypothesis allows determining the divergence. Fig. 6.6 shows the PDFs of the divergence $\nabla \cdot \mathbf{u}$ of all considered velocity fields with respect to the whole spatial domain \mathcal{B} . Moreover, the standard deviations of the respective distributions are shown.

The difference between the original field and its time-mapped counterparts in terms of their spatial distribution of $\nabla \cdot \mathbf{u}$ is larger than the differences of the considered

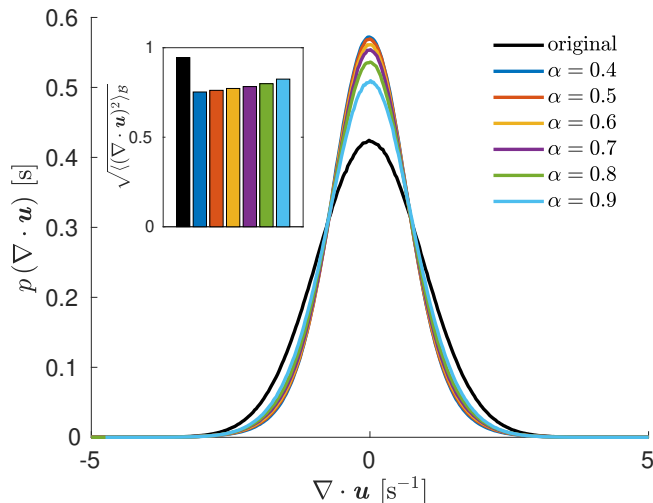


FIGURE 6.6: Probability density functions of the divergence within the domain \mathcal{B} for the velocity before (original) and after application of the time-mapping with different values for α . The bars correspond to the respective standard deviation $\sqrt{\langle (\nabla \cdot \mathbf{u})^2 \rangle_{\mathcal{B}}}$ with respect to the whole spatial domain.

time-mapped fields among each other. The most significant finding is that deviations of the divergence from zero are reduced if the CTRW time-mapping is applied. This shows that the application of the time-mapping method does not lead to a reduced usability as inflow for CFD simulations with regard to the satisfaction of the continuity equation.

6.3 Increment Statistics

As already shown in Section 4.3, the Mann turbulence model is characterized by Gaussian velocity increments. Fig. 6.8 depicts the spatially averaged PDFs of the velocity increments for every time-mapping realization in comparison to their Gaussian counterpart for different temporal separations τ . Leptokurtic behaviour and thus intermittency, the underlying objective of the time-mapping application, evidently arises. It can clearly be seen that deviations from the Gaussian increment distribution of the original field become more pronounced with decreasing α , which is due to the fact that the deviation from $t(s) = s$ increases for small values of α . At $\alpha = 1$ the Lévy distribution (Eq. 2.105) turns into the Dirac distribution $p_\alpha(V) = \delta(1 - V)$ and thus the original time s equals the rescaled time t . Furthermore, a transition towards Gaussian distributions takes place for large temporal separations τ , which reflects the characteristics of atmospheric flow and turbulence in general, as explained in Section 2.2.5.

In order to quantify the deviation of $p(u_\tau)$ from a Gaussian distribution, i. e., the degree of intermittency, more accurately, the kurtosis of u_τ is considered. Fig. 6.8 depicts the spatially averaged kurtosis of the velocity increments as function of τ . It illustrates yet again that non-Gaussian behaviour becomes more pronounced with a decreasing value of α and steadily decreases as the time scale increases. This demonstrates that the Mann turbulence model can be extended by the characteristic of intermittency in the streamwise direction.

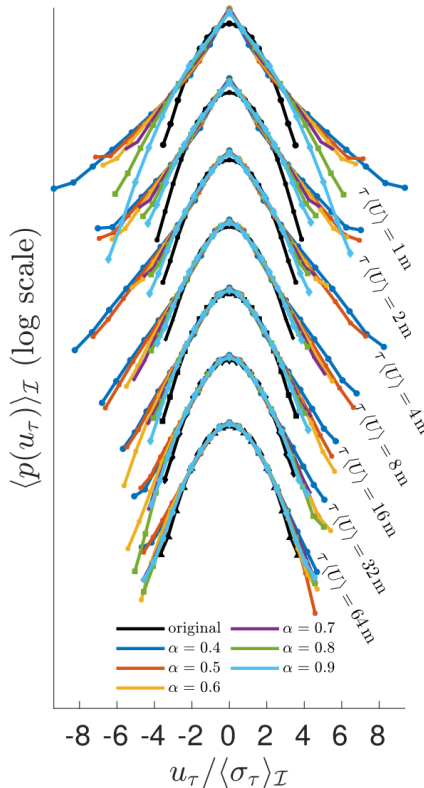


FIGURE 6.7: Spatially averaged probability density functions of velocity increments u_τ for different temporal separations τ for original velocity field and the velocity field after different realizations of the time-mapping process. The PDFs are shifted along the ordinate for the sake of clarity and normalized to their respective standard deviation.

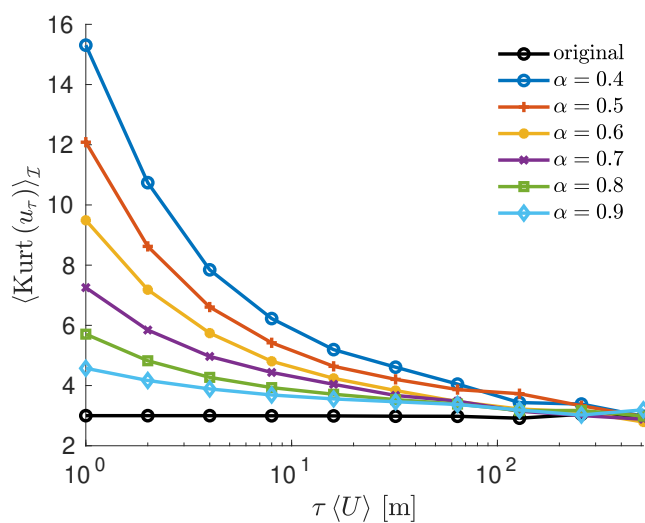


FIGURE 6.8: Spatially averaged kurtosis of velocity increments as function of the temporal separation τ for the original velocity field and the velocity after time-mapping application for different α .

Chapter 7

Conclusion and Outlook

By the analysis of one-point spectra and coherence for an exemplary set of parameters in Chapter 4 it could be shown that the characteristics that constitute the wind model by Mann (1994) are preserved in the respective Fourier simulation according to Mann (1998) for which the corresponding software tool (DTU Wind Energy, 2018) from HAWC2 (Larsen and Hansen, 2007) was used. However, it could be demonstrated that the variances of the velocity components are largely dependent on both the size and the resolution of the spatial domain. Thus related equations in the work of Mann (1994), which describe the modeled velocity field in an infinite and continuous domain ($\mathcal{B} = \mathbb{R}^3$), do not apply to the finite and discrete Fourier simulated data. Furthermore, the divergence of the Fourier simulated velocity field within the spatial domain averages to zero but varies with a standard deviation of approximately 0.109 s^{-1} for the considered set of parameters. The application of a method by Shirani et al. (1981) for the reduction of the divergence does not lead to a significant improvement. Velocity increments of the simulated velocities evidently follow Gaussian distributions. The Mann turbulence model hence does not include the characteristic of intermittency.

In Chapter 5 the utilization of Fourier simulated Mann turbulence as inflow for LES with a volume-force based approach is investigated. To this end, the inflow method was firstly tested with a piecewise constant inflow velocity of different magnitudes. The test demonstrates that target velocities are only reached for small magnitudes which therefore restricts the applicability of the method to small turbulence intensities. Moreover, deviation of the resulting velocity in LES from the target value is generally more pronounced for negative velocities. With Mann turbulence as inflow it is found that the spatial resolution of the LES grid has significant influence on the velocity spectra: the lower the spatial resolution, the more pronounced the damping of the one-point spectra at high frequencies. For this reason, the resolution of the grid was chosen significantly higher than the spatial resolution of the inflow field. In order to assess the effect of anisotropy and turbulence intensity, isotropic and non-isotropic inflow fields with different longitudinal turbulence intensities were considered.

Considering the one-point spectra of the velocity components in LES at different locations in the domain, a pronounced damping at high frequencies, which becomes more pronounced with increasing distance to the inlet plane, is apparent. Up to approximately 10 Hz, however, the spectra are generally in good agreement with the spectra of the original inflow velocity field.

The evolution of the longitudinal turbulence intensity TI_x , whose basic course traces back to the volume-force approach for the inflow, is found to be fundamentally different to the evolution of the TI of the transverse velocity components. In general,

the turbulence intensities do not fully reach their target value, whereby the differences between actual TI in LES and target TI become larger for increasing input turbulence intensity. The attenuation of the turbulence intensities largely corresponds to the damping of the velocity spectra at high frequencies. Another important result to be noted is that the longitudinal turbulence intensity is generally more markedly damped for the non-isotropic case than for the isotropic case.

Comparison of the coherence for different horizontal spatial separations at different locations in the LES domain with their respective counterpart of the original inflow field shows that changes in the coherence particularly occur on small temporal and spatial scales. Moreover, differences in the coherence between isotropic and non-isotropic inflow are apparent at small spatial scales.

A further investigation on the statistics of velocity increments shows that leptokurtic increment distributions, and thus intermittency, occur in LES, even though the inflow velocity field is Gaussian. The degree of intermittency generally becomes larger with increasing distance to the inlet plane and is larger for high turbulence intensities, too. Also, differences between isotropic and non-isotropic inflow are evident. Apparently, intermittency in the non-isotropic case is generally more pronounced at large distances to the inflow location.

Overall, the disparities between the statistical quantities of the modeled input velocity fields and the resulting fields in LES are multifactorially conditioned. The limitations of the volume-force approach employed for introducing the synthetic turbulence to LES plays a major role here. Troldborg et al. (2014) propose the convolution of the volume force (given by Eq. 3.18) with a one-dimensional Gaussian distribution in streamwise direction, which leads to a spatial smoothing of the force distribution so that singular behaviour is circumvented. This approach might as well be advisable for the presented inflow case in order to potentially reduce the large gradients of the velocity, and thus of the turbulence intensities, present at the inlet plane. The utilization of alternative methods for the imposition of synthetic turbulence as, for instance, suggested by Schmidt and Breuer (2017) might as well be worth further investigation. Another important factor for the changes of the initial characteristics of Mann turbulence in LES is the damping of spatial structures on small scales due to both physical and numerical effects of dissipation. In order to evaluate the proportion of their contribution, it might be appropriate to further investigate the influence of the grid resolution. The general tendency of stronger damping at high turbulence intensities is of physical nature. For instance, Azevedo et al. (2017) were able to demonstrate experimentally with 2D laser Doppler velocimetry in a straight compound-channel flow that dissipation rate and turbulence intensity have a linear relation. Further factors for the differences between LES flow field and inflow field are the limited validity of Taylor's hypothesis, which is utilized for the conversion of the longitudinal spatial coordinate of the inflow field into the time axis, at high turbulence intensities and the correction of the divergence in LES.

At this point, it should also be noted that the wind model by Mann comprises atmospheric turbulent velocity fluctuations \mathbf{u} according to the Reynolds decomposition under the influence of shear via the parameter Γ but does not directly describe the shear itself. In the scope of this work, the total velocity field $\mathbf{U} = \langle \mathbf{U} \rangle + \mathbf{u}$ was composed with a constant mean velocity $\langle \mathbf{U} \rangle$ ($\partial \langle \mathbf{U} \rangle / \partial x_i = 0$). The corresponding results provide information about the isolated effect of shear influence on velocity fluctuations \mathbf{u} without shear for the mean velocity $\langle \mathbf{U} \rangle$ that is carrying the fluctuating part in the spirit of Taylor's hypothesis. A simultaneous consideration of shear influence on velocity fluctuations with the Mann wind model and actual shearing of the mean velocity (i. e., $d \langle \mathbf{U} \rangle / dz > 0$) is rather challenging but worth further investigation.

First of all, the difficulty lies in the fact that there is no direct functional relation between Γ and the vertical gradient $d\langle U \rangle / dz$. Secondly, a shearing of the mean velocity would probably lead to a distortion of the spatial structure of the turbulence that becomes more pronounced over time.

The significance of intermittency in the context of wind turbine loads has been much debated. For instance, Mücke et al. (2011) carried out aero-elastic simulations with Gaussian and non-Gaussian flow conditions, including wind data based on the CTRW wind model by Kleinhans (2008), which showed increased torque fluctuations for the airfoil and the main shaft for cases with high intermittency. The authors suggest that this might lead to additional loads and therefore additional fatigue. However, aero-elastic simulations by Berg et al. (2016) indicate that only minor increases in the extreme loads of the tower base fore-aft moment (i. e., with respect to the streamwise direction) arise when non-Gaussian turbulence and high wind speeds are considered. These are negligible when taking into account the safety standards of modern wind turbines. The simulations did not indicate further impact on other load quantities. Moreover, the authors suggest that the turbine behaves similar to a low-pass filter, averaging out the highest frequencies and thus the smallest scales on which the non-Gaussian behaviour is present. Based on blade element momentum (BEM) simulations, Schwarz et al. (2019) suggested that significant differences in the fatigue loads for Gaussian and non-Gaussian wind fields arise in the case of large coherent structures. For the generation of the wind fields, the authors spatially assembled one-dimensional time series based on Kleinhans' CTRW wind model. Furthermore, different spatial correlations from delta correlation up to full correlation were considered.

The approach for the generation of intermittent wind fields by combination of the Mann turbulence model and the CTRW time-mapping of Kleinhans's model presented in this work (Chapter 6) may pose an alternative to previous wind models that aim to represent realistic spatial correlations and non-Gaussian behavior of velocity increments. In particular, the statistics of the velocity field are (apart from interpolation effects) unchanged in the plane transverse to the mean flow direction since the time-mapping only applies to the streamwise direction. It could be shown that the one-point spectra are primarily affected at high frequencies where the time-mapping leads to an attenuation. The standard deviations of the velocity components only change slightly. With regard to the coherence, differences between original velocity field and intermittent counterparts are very clear and present particularly at high frequencies. The main benefit of the presented approach is thus the provision of realistic spatial structures at larger scales. Further investigation of mechanical wind turbine loads based on this approach should therefore be targeted. Moreover, the application of CTRW time-mapping to Mann turbulence leads to a reduction of the divergence. Therefore, the utilization of the velocity fields in numerical simulations for incompressible flows is not further restricted in this regard. However, the limited comparability of Gaussian Mann turbulence and its intermittent counterparts due to the changes of spectra and coherence that result from the time-mapping process (see Section 6.1) calls for further development of the approach. It might for instance be possible to adapt the spectral tensor (Eqs. 2.93 – 2.98) that constitute Mann's wind model so that both original and time-mapped velocity field have similar spectral properties which would allow for a more precise analysis of the isolated effect of intermittency on wind turbine loads. More precisely, the model could either be adapted so the resulting velocity field after time-mapping shows the same spectral properties as the original Mann field without subsequent

time-mapping or vice-versa, the model is adapted so that the spectra of the field without time-mapping shows the same spectral properties as the original field after time-mapping. The first approach would of course be more desirable since the realistic spectral characteristics of the unchanged original Mann turbulence model would be preserved. The spectral tensor is initially based on the energy spectrum $E(\kappa)$ (see Eq. 2.75) for which the von Kármán spectrum (Eq. 2.69) is originally chosen. It would therefore be appropriate to adapt Mann's model by modifying the energy spectrum. For instance, Pope (2001) proposes the following parameterization that would allow for such modification:

$$E(\kappa) = c_K \varepsilon^{2/3} \kappa^{-5/3} f_L(\kappa L) f_{l_\mu}(\kappa l_\eta) \quad (7.1)$$

Here, the first function is given as

$$f_{l_\mu} = \left(\frac{\kappa L}{[(\kappa L)^2 + c_L]^{1/2}} \right)^{5/3+\xi}. \quad (7.2)$$

and describes $E(\kappa)$ for large scales (i. e., at small wavenumbers). For $c_L = 1$, $\xi = 4$ and $f_{l_\mu} = 1$, Eq. 7.1 equals the von Kármán spectrum (see Eq. 2.69). The second function is given as

$$f_{l_\mu}(\kappa l_\mu) = \exp \left\{ -c_{l_\mu,1} \left[\left([\kappa l_\mu]^2 + c_{l_\mu,2}^4 \right)^{1/4} - c_{l_\mu,2} \right] \right\} \quad (7.3)$$

and describes the viscous cutoff of the energy spectrum at spatial scales below the Kolmogorov length l_μ where the energy is fully dissipated. If l_μ is simply considered as an adjustable parameter, variation of $c_{l_\mu,1}$, $c_{l_\mu,2}$ and l_μ allows for the modification of the energy spectrum at large wavenumbers and thus in the range where the spectra of Mann turbulence are changed due to the CTRW time-mapping (see Fig. 7.1).

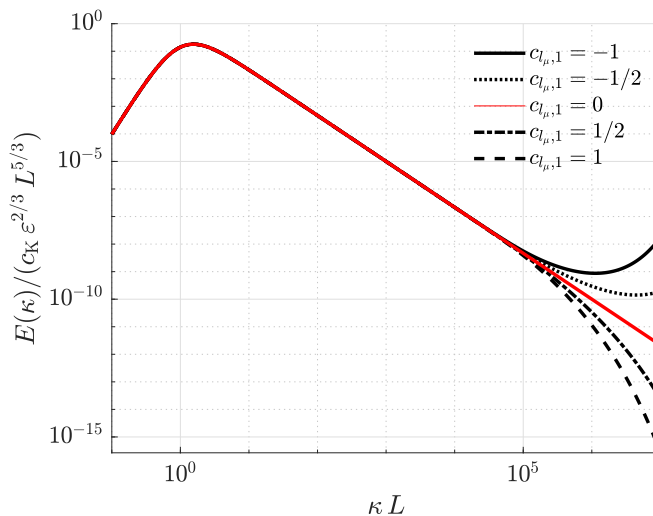


FIGURE 7.1: Energy spectrum according to Eq. 7.1 for $l_\mu/L = 10^{-5}$, $c_L = 1$ and $\xi = 4$ (von Kármán spectrum at small wavenumbers) and different values for $c_{l_\mu,1}$, $c_{l_\mu,2} = 1$. The red line ($c_{l_\mu,1} = 0$) corresponds to the von Kármán spectrum for the whole wavenumber range.

Appendix A

Probability Distributions

The probability distributions that are considered in scope of this work and their respective probability density function (PDF), cumulative distribution function (CDF), mean and standard deviation are given as follow:

- Gaussian distribution:

- PDF:

$$p_U(V) = \frac{1}{\sqrt{2\pi}\sigma} \exp\left[-\frac{1}{2}\left(\frac{x-\mu}{\sigma}\right)^2\right] \quad (\text{A.1})$$

- CDF:

$$f_U(V) = \frac{1}{2} \left[1 + \operatorname{erf}\left(\frac{x-\mu}{\sqrt{2}\sigma}\right) \right] \quad (\text{A.2})$$

- mean:

$$\langle U \rangle = \mu \quad (\text{A.3})$$

- standard deviation:

$$\sqrt{\operatorname{var}(U)} = \sigma \quad (\text{A.4})$$

- Lévy distribution:

- PDF:

$$p_U(V) = \frac{1}{\pi} \operatorname{Re} \left\{ \int_0^\infty \exp\left[-i\xi V - \xi^\alpha \exp\left(-i\frac{\pi\alpha}{2}\right)\right] d\xi \right\} \quad (\text{A.5})$$

- CDF: analytical expression only for certain parameter values

- mean: undefined

- standard deviation:

$$\sqrt{\operatorname{var}(U)} \longrightarrow \infty \quad (\text{A.6})$$

- Dirac distribution:

- PDF:

$$p_U(V) = p_U(V) = \delta(V - V_0) \quad (\text{A.7})$$

– CDF:

$$f_U(V) = \theta(V - V_0) \equiv \begin{cases} 0 & \text{for } V < V_0 \\ 1 & \text{for } V \geq V_0 \end{cases} \quad (\text{A.8})$$

– mean:

$$\langle U \rangle = V_0 \quad (\text{A.9})$$

– standard deviation:

$$\sqrt{\text{var}(U)} = 0 \quad (\text{A.10})$$

- Uniform distribution:

– PDF:

$$p_U(V) = \begin{cases} \frac{1}{b-a} & \text{for } a \leq V \leq b \\ 0 & \text{otherwise} \end{cases} \quad (\text{A.11})$$

– CDF:

$$f_U(V) = \begin{cases} 0 & \text{for } V < a \\ \frac{V-a}{b-a} & \text{for } V \in [a, b] \\ 1 & \text{for } V > b \end{cases} \quad (\text{A.12})$$

– mean:

$$\langle U \rangle = \frac{1}{2} (a + b) \quad (\text{A.13})$$

– standard deviation:

$$\sqrt{\text{var}(U)} = \frac{1}{12} (b - a)^2 \quad (\text{A.14})$$

- Exponential distribution:

– PDF:

$$p_U(V) = \lambda e^{-\lambda V} \quad (\text{A.15})$$

– CDF:

$$f_U(V) = 1 - e^{-\lambda V} \quad (\text{A.16})$$

– mean:

$$\langle U \rangle = \frac{1}{\lambda} \quad (\text{A.17})$$

– standard deviation:

$$\sqrt{\text{var}(U)} = \frac{1}{\lambda} \quad (\text{A.18})$$

Appendix B

Notes on the Turbulence Intensity Definition

The *turbulence intensity* is sometimes—in contrast to Eq. 2.28—defined as the standard deviation of the *wind speed* variations divided by the mean wind speed $\langle U \rangle$ (see, for example, Burton et al., 2001). The term *speed* however denotes, in a strict sense, the magnitude of the velocity vector (Gibbs and Wilson, 1913). The turbulence intensity according to this definition is therefore generally different from the definition given in Eq. 2.28, since the variance of the magnitude (i. e., the vector norm) of velocity fluctuations

$$\text{var}(|\mathbf{u}|) = \langle |\mathbf{u}|^2 \rangle - \langle |\mathbf{u}| \rangle^2 = \sum_{i=1}^3 \text{var}(u_i) - \left\langle \left(\sum_{i=1}^3 u_i^2 \right)^{1/2} \right\rangle^2 \quad (\text{B.1})$$

is not identical to the variance of each velocity fluctuation component.

The relation between $\text{var}(|\mathbf{u}|)$ and $\text{var}(u_i)$ is obviously not trivial and the comparison of data with the mentioned differing definitions of the turbulence is therefore challenging. However, for the case of isotropic turbulence, i. e., $\text{var}(u_i) = \text{var}(u_j) \forall i, j$, assumed statistical independence of the velocity fluctuation components u_i and normally distributed u_i (as is the case for the Mann turbulence model), the noncentral chi distribution provides a remedy. Its PDF is given as (Krishnan, 1967)

$$p(V; k, \lambda) = e^{-(V^2 + \lambda^2)/2} \frac{V^k \lambda}{(\lambda V)^{k/2}} J_{k/2-1}(\lambda V) \quad (\text{B.2})$$

where $J_{k/2-1}$ is a modified Bessel function of the first kind and it describes the distribution of random variables $V \equiv \sqrt{\sum_{i=1}^k V_i'^2 / \text{var}(V_i)}$ where V_i' ($i = 1, \dots, k$) are independent, normally distributed random variables. λ is related to the mean values of V_i' by $\lambda = \sqrt{\sum_{i=1}^k \langle V_i' \rangle^2 / \text{var}(u_i)}$.

The mean value is given by

$$\langle V \rangle = \int_{\mathbb{R}} V p(V; k, \lambda) dV = \sqrt{\frac{\pi}{2}} L_{1/2}^{(k/2-1)}(\lambda V) \quad (\text{B.3})$$

where $L_n^{(m)}$ is a Laguerre function. Interpreting V_i' as isotropic velocity fluctuation components u_i (same standard deviation σ_{iso} for all components) with zero mean

yields

$$\left\langle \left(\sum_{i=1}^3 u_i^2 \right)^{1/2} \right\rangle = \sqrt{\frac{\pi}{2}} L_{1/2}^{(k/2-1)}(0) \sigma_{\text{iso}} \approx 1.596 \sigma_{\text{iso}} \quad (\text{B.4})$$

and thus $\text{var}(|\mathbf{u}|) \approx 0.453 \sigma_{\text{iso}}^2$.

In addition, it should be noted that the definition of the turbulence intensity for free field wind data can also be dependent on the applied measurement method. The measurand of cup anemometers, for instance, is the magnitude of the horizontal velocity $\sqrt{U_x^2 + U_y^2}$ and statistical quantities as the TI therefore often relate to this quantity.

Appendix C

OpenFOAM® Setup for LES

The directory structure for an OpenFOAM case is given as follows:

```
<case>
  system
    controlDict
    fvSchemes
    fvSolution
    blockMeshDict
    topoSetDict
  constant
    transportProperties
    turbulenceProperties
    fvOptions
    boundaryData
      ...
    polyMesh
      ...
  0 (+ further time directories)
  ...
```

The most important files for the LES that have been carried out in the context of this work are presented in the following.

system

controlDict

```
/*----- C++ -----*/
| ====== | OpenFOAM: The Open Source CFD Toolbox
| \ \ / F ield | Version: 5
| \ \ / O peration | Web: www.OpenFOAM.org
| \ \ / A nd |
| \ \ / M anipulation |
\*-----*/
FoamFile
{
    version      2.0;
    format       ascii;
    class        dictionary;
    location     "system";
    object       controlDict;
}
// * * * * * // * * * * *
libs ("libfvOptionsTurbulence.so");
application pimpleFoam;

startFrom      startTime;
startTime       0;
stopAt         endTime;
endTime         435;
deltaT          0.05;
writeControl   runTime;
writeInterval  100;
purgeWrite     0;
writeFormat    ascii;
writePrecision 6;
writeCompression off;
timeFormat     general;
timePrecision  6;
runTimeModifiable true;
// **** //
```

fvSchemes

fvSolution

blockMeshDict

```

        type      cyclic;
        neighbourPatch front;
        faces    ((7 6 2 3));
    }
    front
    {
        type      cyclic;
        neighbourPatch back;
        faces    ((4 5 1 0));
    }

    left
    {
        type      patch;
        faces    ((0 3 7 4));
    }
    right
    {
        type      patch;
        faces    ((1 2 6 5));
    }
}

);

mergePatchPairs
(
);

// ****
topoSetDict

/*----- C++ -----*/
| =====
| \\ / Field      | OpenFOAM: The Open Source CFD Toolbox
| \\ / Operation   | Version: 5
| \\ / And         | Web:     www.OpenFOAM.org
| \\/ Manipulation |
\*-----*/
FoamFile
{
    version   2.0;
    format    ascii;
    class     dictionary;
    object    topoSetDict;
}

// ****

actions
(
{
    name    inlet;
    type    cellSet;
    action   new;
    source   boxToCell;
    sourceInfo
    {
        box (80. 40. 40.) (82. 120. 120. );
    }
}
);

// ****

```

constant

transportProperties

turbulenceProperties

```

/*-----* C++ -----*/
| \\\| F ield | OpenFOAM: The Open Source CFD Toolbox
| \\\| O peration | Version: 5
| \\\| A nd | Web: www.OpenFOAM.org
| \\\| M anipulation |
\*-----*/FoamFile
{
    version      2.0;
    format       ascii;
    class        dictionary;
    location     "constant";
    object       turbulenceProperties;
}
// * * * * * * * * * * * * * * * * * * * * * * * * * * * * * * * * * * * * * * * * * * * * //simulationType laminar;LES
{
    LESModel      WALE;
    turbulence    on;
    printCoeffs   on;
    delta         cubeRootVol;
    cubeRootVolCoeffs
    {
        deltaCoeff      1;
    }
    PrandtlCoeffs
    {
        delta         cubeRootVol;
        cubeRootVolCoeffs
        {
            deltaCoeff      1;
        }
    }
}
```

```

        }
    smoothCoeffs
    {
        delta          cubeRootVol;
        cubeRootVolCoeffs
        {
            deltaCoeff      1;
        }

        maxDeltaRatio   1.1;
    }

    Cdelta          0.158;
}

vanDriestCoeffs
{
    delta          cubeRootVol;
    cubeRootVolCoeffs
    {
        deltaCoeff      1;
    }

    smoothCoeffs
    {
        delta          cubeRootVol;
        cubeRootVolCoeffs
        {
            deltaCoeff      1;
        }

        maxDeltaRatio   1.1;
    }

    Aplus          26;
    Cdelta          0.158;
}

smoothCoeffs
{
    delta          cubeRootVol;
    cubeRootVolCoeffs
    {
        deltaCoeff      1;
    }

    maxDeltaRatio   1.1;
}

// ****

```

fvOptions

```

/*-----* C++ -----*/
| ====== |
| \ \ / F ield      | OpenFOAM: The Open Source CFD Toolbox
| \ \ / O peration   | Version: 5
| \ \ / A nd         | Web: www.OpenFOAM.org
| \ \ / M anipulation |
\*-----*/
FoamFile
{
    version    2.0;
    format     ascii;
    class      dictionary;
    location   "constant";
    object     fvOptions;
}
// * * * * *

```

```

inlet
{
    type          actuationTurbulenceSource;
    fields        (U);
    selectionMode cellSet;
    cellSet        inlet;
    diskDir        (1 0 0);      // Orientation of the disk
    diskArea       6400;
}

// ****

```

0 (time directory – initial and boundary conditions)

nut (ν_t)

```

/*-----* C++ -----*/
| ====== | |
| \ \ / F ield | OpenFOAM: The Open Source CFD Toolbox
| \ \ / O peration | Version: 5
| \ \ / A nd | Web: www.OpenFOAM.org
| \ \ / M anipulation | |
/*-----*/
FoamFile
{
    version     2.0;
    format      ascii;
    class       volScalarField;
    location    "1";
    object      nut;
}
// * * * * *
dimensions      [0 2 -1 0 0 0];
internalField   uniform 0;

boundaryField
{
    bottomWall
    {
        type      cyclic;
    }
    topWall
    {
        type      cyclic;
    }
    front
    {
        type      cyclic;
    }
    back
    {
        type      cyclic;
    }
    left
    {
        type      zeroGradient;
    }
    right
    {
        type      zeroGradient;
    }
}

```

```

// ****
U

/*
| ====== | *- C++ -* |
| \\\ / F ield | OpenFOAM: The Open Source CFD Toolbox |
| \\\ / O peration | Version: 5 |
| \\\ / A nd | Web: www.OpenFOAM.org |
| \\\/ M anipulation |
*/
FoamFile
{
    version      2.0;
    format       ascii;
    class        volVectorField;
    location     "1";
    object       U;
}
// ****
dimensions      [0 1 -1 0 0 0];
internalField   uniform (10 0 0);

boundaryField
{
    bottomWall
    {
        type         cyclic;
    }
    topWall
    {
        type         cyclic;
    }
    front
    {
        type         cyclic;
    }
    back
    {
        type         cyclic;
    }
    left
    {
        type         fixedValue;
        value        $internalField;
    }
    right
    {
        type         zeroGradient;
    }
}

// ****

```


Appendix D

Parameter for LES Inflow Mann Box

The physical parameters of the Mann model and the resulting turbulence intensities of the simulated fields, which are used as input for LES, are given in Tab. D.1. The label "I" refers to the target longitudinal TI of 5 %, whereas "II" and "III" refer to 10 % and 15 %, respectively. The tool being used for the Fourier simulation of the

	n_x	n_y	n_z	δx [m]	δy [m]	δz [m]	Γ	L [m]	$c_K \varepsilon^{2/3}$ [$m^{4/3} s^{-2}$]	TI_x [%]	TI_y [%]	TI_z [%]
I	2048	64	64	2.0	2.0	2.0	0	46.55	0.029304	5.0 ± 0.346	4.750 ± 0.307	5.009 ± 0.185
	2048	64	64	2.0	2.0	2.0	4	46.55	0.009134	5.0 ± 0.627	3.314 ± 0.259	2.644 ± 0.120
II	2048	64	64	2.0	2.0	2.0	0	93.1	0.073644	10.0 ± 0.827	9.424 ± 0.629	10.388 ± 0.478
	2048	64	64	2.0	2.0	2.0	4	93.1	0.024562	10.0 ± 1.142	6.608 ± 0.436	5.631 ± 0.245
III	2048	64	64	2.0	2.0	2.0	0	139.65	0.124113	15.0 ± 1.308	13.975 ± 0.791	15.666 ± 0.766
	2048	64	64	2.0	2.0	2.0	4	139.65	0.045	15.0 ± 1.154	9.773 ± 0.552	8.818 ± 0.383

TABLE D.1: Parameters for the simulated turbulent velocity fields and resulting turbulence intensities at $\langle U \rangle = 10 \text{ m s}^{-1}$. TIs refer to the "cropped" part of the spatial domain.

turbulent field (DTU Wind Energy, 2018) demands n_i as powers of two (i. e., $n_i = 2^n$ with $n \in \mathbb{N}$). Thus, the size of its (y, z) plane cannot be reached exactly with the chosen spatial increment of $\delta x_i = 2 \text{ m}$. It is therefore necessary to only consider the part of the Mann boxes that matches the inlet plane of the LES (see Fig. 5.1) which has an area of $80 \text{ m} \times 80 \text{ m}$. The Mann boxes are accordingly "cropped", starting from the origin of the coordinate system.

Bibliography

- Altenbach, Holm (2012). *Kontinuumsmechanik*. Springer.
- Anderson Jr, John David (2010). *Fundamentals of Aerodynamics*. Tata McGraw-Hill Education.
- Azevedo, Ricardo, Luís R Roja-Solórzano, and João Bento Leal (2017). "Turbulent structures, integral length scale and turbulent kinetic energy (TKE) dissipation rate in compound channel flow". In: *Flow Measurement and Instrumentation* 57, pp. 10–19.
- Batchelor, George Keith (2000). *An Introduction to Fluid Dynamics*. Cambridge University Press.
- Batchelor, George Keith and Albert Alan Townsend (1949). "The nature of turbulent motion at large wave-numbers". In: *Proceedings of the Royal Society of London. Series A. Mathematical and Physical Sciences* 199.1057, pp. 238–255.
- Berg, Jacob et al. (2016). "Gaussian vs non-Gaussian turbulence: impact on wind turbine loads". In: *Wind Energy* 19.11, pp. 1975–1989.
- Bies, David A, Colin Hansen, and Carl Howard (2017). *Engineering noise control*. CRC press.
- Biferale, L et al. (2006). "Lagrangian statistics in fully developed turbulence". In: *Journal of Turbulence* 7, N6.
- Blitzstein, Joseph K and Jessica Hwang (2019). *Introduction to probability*. Crc Press.
- Boettcher, F et al. (2003). "On the statistics of wind gusts". In: *Boundary-Layer Meteorology* 108.1, pp. 163–173.
- Bortoli, D et al. (2000). "Preliminary results from an experiment on the interaction of a flow with an orographic relief". In: CONFERENCE PROCEEDINGS-ITALIAN PHYSICAL SOCIETY. Vol. 69. Editrice Compositori; 1999, pp. 203–220.
- Breuer, Michael, Guillaume De Nayer, and Manuel Münsch (2011). "Fluid–structure interaction of a flexible structure in a turbulent flow using les". In: *Direct and Large-Eddy Simulation VIII*. Springer, pp. 449–454.
- Burton, Tony et al. (2001). *Wind energy handbook*. Vol. 2. Wiley Online Library.
- Castaing, B, Y Gagne, and EJ Hopfinger (1990). "Velocity probability density functions of high Reynolds number turbulence". In: *Physica D: Nonlinear Phenomena* 46.2, pp. 177–200.
- Cheynet, Etienne (Apr. 29, 2020). *Uniform shear model (Mann, 1994)*. Version 1.7. (Last accessed on 27.11.20). URL: <https://github.com/ECheynet/MannModel1994/releases/tag/v1.7>.
- Clarke, Steve (2003). *Electricity generation using small wind turbines at your home or farm*. Ontario, Ministry of Agriculture and Food.
- Cootner, Paul H (1967). *The random character of stock market prices*. MIT press.
- Deardorff, James W et al. (1970). "A numerical study of three-dimensional turbulent channel flow at large Reynolds numbers". In: *J. Fluid Mech* 41.2, pp. 453–480.
- Di Mare, L et al. (2006). "Synthetic turbulence inflow conditions for large-eddy simulation". In: *Physics of Fluids* 18.2, p. 025107.
- Dimotakis, P, RC Lye, and DZ Papantoniou (1981). "In 15th Intl Symp". In: *Fluid Dyn., Jachranka, Poland*.

- DTU Wind Energy (2018). *Mann 64bit turbulence generator*. (Last accessed on 27.11.20). URL: <https://www.hawc2.dk/download/pre-processing-tools>.
- Ehrich, Sebastian (2020). "Turbulent Inflow Models". In: *Handbook of Wind Energy Aerodynamics*, pp. 1–27.
- Erdélyi, Arthur (1953). "Higher transcendental functions". In: *hft1*, p. 59.
- ESDU (1982). *Characteristics of wind speed in the lower layers of the atmosphere newar the ground: Strong Winds (neutral atmosphere)*.
- Faber, Tom E (1995). *Fluid dynamics for physicists*. Cambridge university press.
- Ferziger, Joel H, Milovan Peric, et al. (1999). *Computational Methods for Fluid Dynamics* Springer Verlag.
- Fogedby, Hans C (1994). "Langevin equations for continuous time Lévy flights". In: *Physical Review E* 50.2, p. 1657.
- Friedrich, R (2003). "Statistics of Lagrangian velocities in turbulent flows". In: *Physical review letters* 90.8, p. 084501.
- Frisch, Uriel (1995). *Turbulence: The Legacy of A. N. Kolmogorov*. Cambridge university press.
- Galanti, B and A Tsinober (2004). "Is turbulence ergodic?" In: *Physics Letters A* 330.3–4, pp. 173–180.
- Gibbs, Josiah Willard and Edwin Bidwell Wilson (1913). *Vector Analysis: A Text-book for the Use of Students of Mathematics and Physics, Founded Upon the Lectures of J. Willard Gibbs*... Yale University Press.
- Gilbarg, David and Neil S Trudinger (2015). *Elliptic partial differential equations of second order*. Springer.
- Gilling, Lasse and Niels N Sørensen (2011). "Imposing resolved turbulence in CFD simulations". In: *Wind Energy* 14.5, pp. 661–676.
- Harris, RI (1970). "The nature of the wind". In: *Seminar in the Modern Design of Wind-Sensitive Structures, Construction Industry Research and Information Association*, pp. 29–55.
- Häuser, H. and J. Keiler (2018). *Betreiber-Datenbasis*. URL: <http://www.btrdb.de/>.
- Helmholtz, Hermann von (1868). *Über discontinuirliche Flüssigkeits-Bewegungen*. Akademie der Wissenschaften zu Berlin.
- Holtslag, AAM (2015). "Atmospheric boundary layers: modeling and parameterization". In: *Encyclopedia of Atmospheric Sciences 2nd Edition*. Elsevier, pp. 265–273.
- Holzmann, Tobias (2016). "Mathematics, numerics, derivations and OpenFOAM®". In: *Loeben, Germany: Holzmann CFD*.
- Issa, Raad I (1986). "Solution of the implicitly discretised fluid flow equations by operator-splitting". In: *Journal of computational physics* 62.1, pp. 40–65.
- Jacob, Daniel J (1999). *Introduction to atmospheric chemistry*. Princeton University Press.
- Jaffe, Arthur M (2006). "The millennium grand challenge in mathematics". In: *Notices of the AMS* 53.6.
- Kailasnath, P, KR Sreenivasan, and G Stolovitzky (1992). "Probability density of velocity increments in turbulent flows". In: *Physical review letters* 68.18, p. 2766.
- Kármán, Theodore von (1948). "Progress in the statistical theory of turbulence". In: *Proceedings of the National Academy of Sciences of the United States of America* 34.11, p. 530.
- Karniadakis, George, Ali Beskok, and Narayan Aluru (2006). *Microflows and nanoflows: fundamentals and simulation*. Vol. 29. Springer Science & Business Media.
- Katopodes, Nikolaos D (2018). *Free-surface Flow: Environmental Fluid Mechanics*. Butterworth-Heinemann.

- Kelly, Mark C (2018). "From standard wind measurements to spectral characterization: turbulence length scale and distribution". In: *Wind Energy Science* 3.2, pp. 533–543.
- Khintchine, Alexander (1934). "Korrelationstheorie der stationären stochastischen Prozesse". In: *Mathematische Annalen* 109.1, pp. 604–615.
- Klein, Markus, Amsini Sadiki, and Johannes Janicka (2003). "A digital filter based generation of inflow data for spatially developing direct numerical or large eddy simulations". In: *Journal of computational Physics* 186.2, pp. 652–665.
- Kleinhans, David (2008). "Stochastische Modellierung komplexer Systeme: von den theoretischen Grundlagen zur Simulation atmosphärischer Windfelder". PhD thesis.
- Knight, Frank B (1962). "On the random walk and Brownian motion". In: *Transactions of the American Mathematical Society* 103.2, pp. 218–228.
- Kolmogorov, Andrey Nikolaevich (1941a). "Dissipation of energy in locally isotropic turbulence". In: *Akademija Nauk SSSR Doklady*. Vol. 32, p. 16.
- (1941b). "On degeneration (decay) of isotropic turbulence in an incompressible viscous liquid". In: *Dokl. Akad. Nauk SSSR*. Vol. 31, pp. 538–540.
- (1941c). "The local structure of turbulence in incompressible viscous fluid for very large Reynolds numbers". In: *Cr Acad. Sci. URSS* 30, pp. 301–305.
- (1962). "A refinement of previous hypotheses concerning the local structure of turbulence in a viscous incompressible fluid at high Reynolds number". In: *Journal of Fluid Mechanics* 13.1, pp. 82–85.
- Kornev, Nikolai and Egon Hassel (2007). "Method of random spots for generation of synthetic inhomogeneous turbulent fields with prescribed autocorrelation functions". In: *Communications in numerical methods in engineering* 23.1, pp. 35–43.
- Kramer, Mark A (2013). "An introduction to field analysis techniques: The power spectrum and coherence". In: *The Science of Large Data Sets: Spikes, Fields, and Voxels; J. E., Ed*, pp. 18–25.
- Krishnan, Marakatha (1967). "The noncentral bivariate chi distribution". In: *SIAM Review* 9.4, pp. 708–714.
- Kristensen, L and NO Jensen (1979). "Lateral coherence in isotropic turbulence and in the natural wind". In: *Boundary-Layer Meteorology* 17.3, pp. 353–373.
- Larsen, Torben Juul and Anders Melchior Hansen (2007). "How 2 HAWC2, the user's manual". In: *December 2007*.
- Laubrich, T (2009). "Statistical analysis and stochastic modelling of boundary layer wind speed". In: *The European Physical Journal Special Topics* 174.1, pp. 197–206.
- Leonard, A (1975). "Energy cascade in large-eddy simulations of turbulent fluid flows". In: *Advances in geophysics*. Vol. 18. Elsevier, pp. 237–248.
- Lévy, Paul (1925). "Calcul des probabilités". In:
- Lewandowski, Roger and Benoît Pinier (2016). "The Kolmogorov Law of Turbulence What Can Rigorously Be Proved? Part II". In: *The Foundations of chaos revisited: from Poincaré to recent advancements*. Springer, pp. 71–89.
- Lukassen, Laura J and Michael Wilczek (2017). "Lagrangian intermittency based on an ensemble of Gaussian velocity time series". In: *Progress in Turbulence VII*. Springer, pp. 23–29.
- Mandelbrot, Benoit (1960). "The Pareto-Levy law and the distribution of income". In: *International Economic Review* 1.2, pp. 79–106.
- Mann, J and J Peinke (2016). "Wind and Turbulence". In: *Long-term Research Challenges in Wind Energy-A Research Agenda by the European Academy of Wind Energy*. Springer, pp. 9–16.

- Mann, Jakob (1994). "The spatial structure of neutral atmospheric surface-layer turbulence". In: *Journal of fluid mechanics* 273, pp. 141–168.
- (1998). "Wind field simulation". In: *Probabilistic engineering mechanics* 13.4, pp. 269–282.
- Mann, Jakob, Leif Kristensen, and Michael Courtney (1991). *The Great Belt coherence experiment. A study of atmospheric turbulence over water*.
- McDonough, James M (2007). "Introductory lectures on turbulence: physics, mathematics and modeling". In:
- Montroll, Elliott W and George H Weiss (1965). "Random walks on lattices. II". In: *Journal of Mathematical Physics* 6.2, pp. 167–181.
- Mücke, Tanja, David Kleinhans, and Joachim Peinke (2011). "Atmospheric turbulence and its influence on the alternating loads on wind turbines". In: *Wind Energy* 14.2, pp. 301–316.
- Nicoud, Franck and Frédéric Ducros (1999). "Subgrid-scale stress modelling based on the square of the velocity gradient tensor". In: *Flow, turbulence and Combustion* 62.3, pp. 183–200.
- Nieuwstadt, FTM and PG Duynkerke (1996). "Turbulence in the atmospheric boundary layer". In: *Atmospheric Research* 40.2-4, pp. 111–142.
- North, Gerald R, John A Pyle, and Fuqing Zhang (2014). *Encyclopedia of atmospheric sciences*. Vol. 1. Elsevier.
- Obukhov, AM (1962). "Some specific features of atmospheric turbulence". In: *Journal of Geophysical Research* 67.8, pp. 3011–3014.
- Patankar, Suhas Vasant and Dudley Brian Spalding (1972). *A calculation procedure for the transient and steady-state behaviour of shell-and-tube heat exchangers*. Imperial College of Science and Technology, Department of Mechanical Engineering.
- Pearson, Karl (1905). ""DAS FEHLERGESETZ UND SEINE VERALLGEMEINER-UNGEN DURCH FECHNER UND PEARSON." A REJOINDER". In: *Biometrika* 4.1-2, pp. 169–212.
- Phillips, WF (2010). "Limits of Continuum Aerodynamics". In: *Journal of aircraft* 47.1, pp. 225–228.
- Pipinato, Alessio (2015). *Innovative bridge design handbook: Construction, rehabilitation and maintenance*. Butterworth-Heinemann.
- Pope, Stephen B (2001). *Turbulent flows*.
- Renner, Christoph, Joachim Peinke, and Rudolf Friedrich (2001). "Experimental indications for Markov properties of small-scale turbulence". In: *Journal of Fluid Mechanics* 433, p. 383.
- Reynolds, Osborne (1883). "XXIX. An experimental investigation of the circumstances which determine whether the motion of water shall be direct or sinuous, and of the law of resistance in parallel channels". In: *Philosophical Transactions of the Royal society of London* 174, pp. 935–982.
- (1895). "Iv. on the dynamical theory of incompressible viscous fluids and the determination of the criterion". In: *Philosophical transactions of the royal society of london.(a.)* 186, pp. 123–164.
- Richardson, Lewis Fry (1922). *Weather prediction by numerical process*. Cambridge university press.
- Sagaut, Pierre (2006). *Large eddy simulation for incompressible flows: an introduction*. Springer Science & Business Media.
- Santiago, Jose-Luis, Alberto Martilli, and Fernando Martin (2017). "On dry deposition modelling of atmospheric pollutants on vegetation at the microscale: Application to the impact of street vegetation on air quality". In: *Boundary-Layer Meteorology* 162.3, pp. 451–474.

- Schlichting, Hermann and Klaus Gersten (2016). *Boundary-layer theory*. Springer.
- Schmidt, Stephan and Michael Breuer (2017). "Source term based synthetic turbulence inflow generator for eddy-resolving predictions of an airfoil flow including a laminar separation bubble". In: *Computers & Fluids* 146, pp. 1–22.
- Schmidt, Wolfram, Wolfgang Hillebrandt, and Jens C Niemeyer (2006). "Numerical dissipation and the bottleneck effect in simulations of compressible isotropic turbulence". In: *Computers & Fluids* 35.4, pp. 353–371.
- Schumacher, Jörg et al. (2014). "Small-scale universality in fluid turbulence". In: *Proceedings of the National Academy of Sciences* 111.30, pp. 10961–10965.
- Schwarz, Carl Michael, Sebastian Ehrich, and Joachim Peinke (2019). "Wind turbine load dynamics in the context of turbulence intermittency". In: *Wind Energy Science* 4.4, pp. 581–594.
- Shirani, E, Joel H Ferziger, and William C Reynolds (1981). "Mixing of a passive scalar in isotropic and sheared homogeneous turbulence". In:
- Smagorinsky, Joseph (1963). "General circulation experiments with the primitive equations: I. The basic experiment". In: *Monthly weather review* 91.3, pp. 99–164.
- Sørensen, Niels N et al. (2018). "Aerodynamic effects of compressibility for wind turbines at high tip speeds". In: *Journal of Physics: Conference Series*. Vol. 1037. 2. IOP Publishing, p. 022003.
- Stull, Roland B (2012). *An introduction to boundary layer meteorology*. Vol. 13. Springer Science & Business Media.
- Tampieri, Francesco et al. (2016). "On turbulence characteristics at Ny-Ålesund–Svalbard". In: *Rendiconti Lincei* 27.1, pp. 19–24.
- Taylor, Geoffrey Ingram (1938). "The spectrum of turbulence". In: *Proceedings of the Royal Society of London. Series A-Mathematical and Physical Sciences* 164.919, pp. 476–490.
- Thomas, TG and JJR Williams (1999). "Generating a wind environment for large eddy simulation of bluff body flows". In: *Journal of Wind Engineering and Industrial Aerodynamics* 82.1-3, pp. 189–208.
- Thomson, William (1871). "XLVI. Hydrokinetic solutions and observations". In: *The London, Edinburgh, and Dublin Philosophical Magazine and Journal of Science* 42.281, pp. 362–377.
- Townsend, A (1976). "A. 1956 The Structure of Turbulent Shear Flow". In: *Cambridge University Press. for 727*, pp. 155–172.
- Troldborg, Niels et al. (2014). "A simple atmospheric boundary layer model applied to large eddy simulations of wind turbine wakes". In: *Wind Energy* 17.4, pp. 657–669.
- Turns, Stephen (2006). *Thermal-fluid sciences: an integrated approach*. Cambridge University Press.
- Vallis, Geoffrey K and John O Roads (1986). "Turbulent Effects in Large Scale Flow over Orography". In: *Proceedings of International Symposium on the Qinghai-Xizang Plateau and Mountain Meteorology*. Springer, pp. 990–1014.
- Van Loan, Charles (1992). *Computational frameworks for the fast Fourier transform*. SIAM.
- Veers, Paul (1984). "Modeling stochastic wind loads on vertical axis wind turbines". In: *25th Structures, Structural Dynamics and Materials Conference*, p. 910.
- Weller, Henry and Hrvoje Jasak (2019). *OpenFOAM Version 7*. (Last accessed on 10.12.20). URL: openfoam.com.
- Wiener, Norbert (1930). "Generalized harmonic analysis". In: *Acta mathematica* 55, pp. 117–258.
- Wray, AA and JCR Hunt (1990). "Algorithms for classification of turbulent structures". In: *Topological fluid mechanics*, pp. 95–104.

- Xie, Zheng-Tong and Ian P Castro (2008). "Efficient generation of inflow conditions for large eddy simulation of street-scale flows". In: *Flow, turbulence and combustion* 81.3, pp. 449–470.
- Xie, Zhengtong et al. (2004). "Large-eddy simulation of turbulent flow over a rough surface". In: *Boundary-layer meteorology* 111.3, pp. 417–440.